Fall 12-18-2020

Rilpivirine-Associated Aggregation-Induced Emission Enables Cell-Based Nanoparticle Tracking

Insiya Mukadam
University of Nebraska Medical Center

RILPIVIRINE-ASSOCIATED AGGREGATION-INDUCED EMISSION ENABLES CELL-BASED NANOPARTICLE TRACKING

By

Insiya Mukadam

A DISSERTATION

Presented to the Faculty of

the University of Nebraska Medical Center

in Partial Fulfillment of the Requirements

for the Degree of Doctor of Philosophy

Pharmaceutical Sciences
Graduate Program

Under the Supervision of Professors Howard E. Gendelman
and Bhavesh D. Kevadiya

University of Nebraska Medical Center
Omaha, Nebraska

December 2020

Supervisory Committee:

Aaron Mohs, Ph.D. Corey Hopkins, Ph.D.

Larisa Poluektova, M.D., Ph.D.

RILPIVIRINE-ASSOCIATED AGGREGATION-INDUCED EMISSION ENABLES CELL-BASED NANOPARTICLE TRACKING

Insiya Mukadam, Ph.D.

University of Nebraska Medical Center, 2020

Supervisors: Howard E. Gendelman, M.D. and Bhavesh D. Kevadiya, Ph.D.

Antiretroviral therapy (ART) has improved the quality and duration of life for people living with human immunodeficiency virus (HIV) infection. However, limitations in drug efficacy, the emergence of viral mutations and the paucity of cell-tissue targeting remain. We posit that to maximize ART potency and therapeutic outcomes newer drug formulations that reach HIV cellular reservoirs need to be created. In a step towards achieving this goal we discovered the aggregation-induced emission (AIE) property of the non-nucleoside reverse transcriptase inhibitor Rilpivirine (RPV) and used it as a platform for drug cell and subcellular tracking. RPV nanocrystals were created with endogenous AIE properties enabling the visualization of intracellular particles in cell and tissue-based assays. The intact drug crystals were easily detected in CD4+ T cells and macrophages, the natural viral target cells, by flow cytometry and ultraperformance liquid chromatography tandem mass spectrometry. We conclude that AIE can be harnessed to monitor cell biodistribution of selective antiretroviral drug nanocrystals.

ACKNOWLEDGEMENTS

The journey that led to my enrollment in a Ph.D. program has been far more inspiring than my Ph.D. journey itself. First and foremost, I would like to thank my parents (Zoher and Jumana Mukadam) for bringing me into this world and for giving me this extraordinary life and my sister (Lulua Mukadam) for giving me the opportunity to experience sisterhood. I would also like to thank my grandparents and my extended family for all their love, support and blessings. I hope that I continue to make them proud of the person I am, now and in the future. A big thank you to my husband (Ali Alsaadi) for being my constant pillar of support and encouragement, especially during the trying times of my Ph.D. journey. My education thus far would have been impossible without the amazing teachers I have had throughout my educational career. I deeply and wholeheartedly thank all the teachers that have inspired and educated me to be the person I am today.

I am deeply grateful to my mentor and supervisor, Dr. Howard Gendelman, for believing in me and allowing me to learn and grow as a Ph.D. student in his laboratory. While he may be tough and unyielding at times, he is also equally caring and understanding towards his students. It is his ability to be a great mentor that has pushed me to be the skilled scientist I am today. A big thank you to my co-mentor, Dr. Bhavesh Kevadiya, for being a great teacher and for always making sure that there was never a dull moment, no matter how stressful the situation became. I would also like to thank my committee members: Dr. Aaron Mohs, for a great collaborative experience; Dr. Corey Hopkins for his time and insightful suggestions; Dr. Larisa Poluektova for her guidance and thoughtfulness. I would

also like to thank Jatin, Brendan and Wilson for being great co-workers with a special thank you to Yoni and Hassan for not only being terrific lab mates with their assistance and input with experiments but also being great friends by supporting and motivating me through all the ups and downs of being a Ph.D. student. Thank you, for making me laugh and keeping me going throughout my journey.

They say, ‘friends are the family you choose’, and that has been especially true with the friends I have made here in Omaha, Nebraska. Being an international student, there have been additional challenges to face such as culture shock and a yearning for home. I owe it to all the friends I have made here in Omaha for making everyday life more enjoyable, for being there for me when I needed support and for being my constant cheerleaders. Thank you, for making Omaha, a home away from home.

Insiya Mukadam

TABLE OF CONTENTS

LIST OF FIGURES

LIST OF TABLES

LIST OF ABBREVIATIONS

AIDS: acquired immune deficiency syndrome

AIE: aggregation-induced emission

AFM: atomic force microscopy

ART: antiretroviral therapy

ARV: antiretroviral drugs

BSA: bovine serum albumin

CD: cluster of differentiation

DMSO: dimethyl sulfoxide

DLS: dynamic light scattering

DSPE-PEG2000:1,2-distearoyl-sn-glycero-3-phosphoethanolamine-N-[amino(polyethylene glycol)-2000]

DTA: derivative thermal analysis

FACS: fluorescence-activated cell sorting

HIV-1: human immunodeficiency virus type 1

HPS: hexaphenylsilole

HSC: hematopoietic stem cells

IP: intraperitoneal

IV: intravenous

LA ARV: long-acting antiretroviral drugs

LA NRPV: long-acting nano-formulated rilpivirine

LASER ART: long-acting slow effective release antiretroviral therapy

MDM: human monocyte-derived macrophages

MFI: median fluorescent intensity

MOI: multiplicity of infection

MTT: 3-(4,5-dimethylthiazol-2-yl)-2,5-diphenyltetrazolium bromide

NNRTI: non-nucleoside reverse transcriptase inhibitor

NSG: Nod.*Cg-Prkdc*^{scid}*IL2rg*^{tm1Wjl} / SzJ mice

PBS: phosphate-buffered saline

PBL: peripheral blood lymphocytes

PBMC: peripheral blood mononuclear cells

PC: phosphatidylcholine

PDI: polydispersity index

PFA: paraformaldehyde

PK: pharmacokinetic

RB: round-bottom flask

RIM: restricted intramolecular motion

RIR: restricted intramolecular rotation

RIV: restricted intramolecular vibration

RPV: Rilpivirine

RPV-NC: Rilpivirine nanocrystals

RT: reverse transcriptase

SEM: scanning electron microscopy

TEM: transmission electron microscopy

TGA: thermogravimetric analysis

TNT: tunneling nanotubes

UPLC-MS/MS: ultraperformance liquid chromatography-tandem mass spectrometry

UPLC-TUV: ultraperformance liquid chromatography-tunable UV detector

UV : ultraviolet

XRD : x-ray diffraction

CHAPTER 1. INTRODUCTION

1.1 Global Impact of HIV/AIDS

The HIV/AIDS epidemic began in the early 1980s and since then, 75.7 million people have become infected with HIV with 32.7 million people have died from AIDS-related illnesses during this period[1]. With the advent of antiretroviral therapy, patient quality and duration of life have been improved significantly with a 39% decrease in new HIV infections and a 51% decrease in HIV-related deaths between the years of 2000 and 2019 with 15.3 million lives saved due to ART[2]. Early clinical trial reports show that antiretroviral therapy has changed the lives of patients infected with HIV[3, 4]. The past three decades have seen the global use of antiretroviral therapy (ART) for those with or at risk for human immunodeficiency virus type one (HIV-1) infection. ART has decreased disease morbidity and mortality, in infected patients, by maintaining viral suppression to undetectable levels[5, 6]. Further progress towards maintaining regimen adherence and slowing viral transmission can now be realized through long-acting (LA) formulations and LA slow effective release (LASER) ART prodrugs[7-13]. Recent advances have shown “proof of concept” that HIV could be eliminated in live animals using LASER ART and CRISPR/Cas9 viral excision[14]. However, a major obstacle remains in demonstrating HIV-1 elimination in infected people through medical regimens alone[15-19].

1.2 HIV-1 Pathobiology

Infection with HIV-1 begins with the entry of the virus into the host cell. The main cellular targets of HIV are CD4+ helper T cells, macrophages, monocytes, dendritic cells and microglial cells. Viral entry is facilitated by viral envelope proteins namely glycoprotein 120 (gp120) and glycoprotein 41 (gp41). Binding to the host cell is initiated by the interaction of gp120 with the cellular CD4 receptor[20]. This induces a conformational change in the envelope proteins which allows for the interaction of gp120 with either the CXCR4 or CCR5 co-receptor[21]. Interaction with the co-receptor induces additional conformation changes that uncover the gp41 that is hidden by gp120. The viral hydrophobic fusion peptide is inserted into the host cell membrane leading to direct contact between the virus and the target cell, following which a trimeric gp41 complex is formed, pulling the viral and cellular membranes together, allowing the fusion of the virion and release of viral contents into the cell[22]. Within the nucleocapsid of the virus are two plus-stranded RNAs that constitute the HIV genome. These single-stranded viral RNAs are reverse transcribed into double-stranded DNA molecules by the reverse transcriptase enzyme, a characteristic of retroviruses[23]. The reverse transcription complex (RTC) then transitions to the pre-integration complex (PIC) which is then actively transported to the cell nucleus. The viral DNA is then inserted into the host genome by the integrase enzyme, following which the proviral DNA is replicated along with the host DNA as part of the host cell chromosome[24, 25]. The integrated proviral DNA can then remain silent for many years in long-living memory T-cells. Proviral

transcription is then initiated by the viral promoter located in the U3 region of the 5' LTR. Viral transcription and RNA elongation is promoted by the initially generated Tat protein[26] and finally, the complex process of viral assembly is carried out by the gag polyproteins along with assistance from the HIV-1 protease to form the virions[27]. This progeny of virions is then released from the infected cells by a process of budding. The released virions then undergo maturation and hijack other target cells culminating as a major threat to the host's immune system. The infection leads to a marked and progressive depletion of CD4+ T cells due to their excessive destruction[28]. A major depletion of CD4+ T cells occurs in the gastrointestinal tract early on and continues throughout all stages of infection[29]. Early signs of infection manifest as flu-like symptoms, but disease progression brings plasma viremia to a set point after which patients can become asymptomatic for extended periods. Infection is also characterized by a significant increase in immune activation[28]. Without treatment, the host immune system is eventually weakened to a point at which immune cell depletion makes the body susceptible to opportunistic infections. Simultaneously, long-living T cells enter a latent stage of HIV infection wherein they do not show any gene expression for several years before being reactivated to produce infectious HIV particles. To ensure effective and sustained eradication of HIV, these viral reservoirs need to be identified and treated to prevent further spread of HIV infections. To address this, antiretroviral drugs (ARVs) and viral elimination agents must be precisely delivered to CD4+ T cell and monocyte-macrophages, the principal viral cell reservoirs.

1.3 Targeting viral reservoir sites

The development of highly active antiretroviral therapy (HAART) enables a greater degree of control of viral replication in HIV-infected individuals. Indeed, the widespread use of HAART has led to a significant decline in the incidence of AIDS[30]. However, while HIV treatment and therapy have dramatically changed the course of infection in HIV-infected individuals, a critical obstacle lies in finding and delivering therapeutics to latent viral reservoirs[16, 18, 19, 31]. It has been reported that viral rebound was observed upon interruption of HAART in infected individuals in whom extensive viral suppression was obtained[32]. The major latent HIV reservoir in infected individuals has been established to be the pool of resting CD4+ T cells[33]. Initially, it was believed that viral latency was largely limited to the concept of preintegration latency which may last for a period of days until the cells become activated leading to reverse transcription followed by integration of proviral DNA into cellular DNA[34, 35]. However, it has been shown that <0.1% of resting CD4+ T cells carry integrated provirus, i.e. postintegration latency. In this state, the reverse transcribed proviral DNA is integrated into cellular DNA and can remain transcriptionally silent for long periods of time[36, 37]. Other potential reservoirs of HIV exist in tissues such as the brain, gut-associated lymphoid tissue, bone marrow, and genital tract[38, 39]. In addition, the interaction of HIV with monocytes and dendritic cells makes them potential viral reservoirs as well[40, 41].

The imminent dangers posed by viral reservoirs demand the advancement of delivery strategies to greatly improve the entry and accumulation of drug

nanoformulations into viral reservoir sites. To enhance delivery to intracellular reservoirs, various strategies such as enhancement of molecule lipophilicity or hydrophobicity have been explored. Delivery to anatomical reservoirs sites presents a more complex approach due to the physiological differences between organs as well as between tissues. For these sites, prodrug strategies have been employed to alter the physicochemical properties of drug molecules. Furthermore, invasive administration has also been employed to surpass the blood-brain barrier, however, long-term therapy may not be a practical option for intracerebral delivery. Another approach that has been extensively explored for drug delivery is nanocarrier systems. Numerous systems from liposomes[42, 43] to solid lipid nanoparticles[44, 45] and polymeric nanoparticles[46] have been employed. While efficient drug delivery systems have been established, the need for a platform that enables effective tracking of nanoparticles into cellular sub-populations still persists. To identify and deliver antiretroviral therapies to viral reservoir sites, we have harnessed herein, the AIE property of RPV to develop a platform that enables drug nanoparticle tracking to immune cell sub-populations. Effective and successful targeting of viral reservoir sites can indeed enable HIV eradication through complete and thorough suppression of viral replication[47].

1.4 Rilpivirine (RPV)

Soon after the outbreak of the HIV epidemic, the development of antiretrovirals began. Substantial progress has been made since then as

antiretroviral research has come a long way from Zidovudine, the first HIV drug to be approved by the US FDA[48] to Fostemsavir, an attachment inhibitor that received US FDA approval July 2020[49]. With the understanding of HIV and its life cycle, new and various targets were identified for the development of novel antiretroviral compounds. In 1995, the first class of HIV drugs, protease inhibitors, was created followed closely by the non-nucleoside reverse transcriptase inhibitors in 1996[50, 51]. Over the next few years, new classes of HIV compounds emerged such as fusion inhibitors[52], entry inhibitors[53] and integrase inhibitors[54], the latest being attachment inhibitors[49, 55]. As HIV understanding advanced and antiretroviral drug development progressed, it became apparent that combination antiretroviral therapy was necessary for effective management of HIV, to avoid the development of resistance and to reduce morbidity and mortality rates[56, 57]. Thus, further advances in antiretroviral treatment involved the development of single multi-drug tablets such as Atripla™ (efavirenz, emtricitabine and tenofovir disoproxil fumarate)[58] and Biktarvy® (bictegravir, emtricitabine and tenofovir alafenamide)[59].

In 2011, a new non-nucleoside reverse transcriptase inhibitor (NNRTI), rilpivirine (RPV), was approved by the FDA. NNRTIs are non-competitive inhibitors and act by binding to a hydrophobic pocket near the catalytic site of reverse transcriptase (RT)[13]. With antiviral activity in the sub-nanomolar range (0.73 nM), RPV is a highly active molecule from the diarylpyrimidine family of NNRTIs[60]. RPV is active against a wide variety of NNRTI resistant HIV strains due to its flexibility of binding at the allosteric site of HIV-1 RT[61]. The broad-spectrum activity and presentation of fewer adverse effects differentiates RPV from other NNRTIs such

as Nevirapine (NVP) and Efavirenz (EFV) that have been reported to generate hepatotoxic and neuropsychiatric side effects respectively[62, 63].

In our efforts to develop platforms that could reach viral reservoir sites, we uncovered yet another property of RPV that distinguishes it from other NNRTIs. We found that RPV exhibits the phenomenon of aggregation-induced emission (AIE). In its aggregated form, RPV emits blue fluorescence when excited by UV light. RPV proved to be an excellent candidate for ARV tracking as it is used as part of LA antiretroviral regimens and its mechanism of action involves interference with the early-stage life cycle of HIV replication. To elucidate the RPV AIE property for use in drug tracking, drug nanocrystals (RPV-NC) were synthesized, enabling quantitative analysis of cell targeting by flow cytometry. We were successful in affirming particle biodistribution by ultra-performance liquid chromatography-tandem mass spectrometry (UPLC MS/MS) analysis of the drug in CD4+ T cell and monocyte-macrophage populations. We contend that harnessing the AIE properties of RPV for drug biodistribution could speed the further development of LA ARVs and in success for viral elimination strategies.

1.5 Aggregation Induced Emission (AIE)

AIE is a photophysical phenomenon that was first discovered in 2001[64]. AIE is a phenomenon wherein non-emissive molecules can fluoresce upon excitation when in the form of aggregates or a crystal lattice [64-67]. To date, a plethora of molecules have been characterized for their AIE properties and several more have

been newly synthesized or discovered. One such prototypical molecule is Tetraphenylethylene (TPE) that has been widely studied and characterized for its AIE properties [68-71]. Another organic molecule that has been characterized for its AIE properties is hexaphenylsilole (HPS). Similar to other AIEgens, HPS is non-emissive when its molecules exist in a solution form. However, upon aggregation in an aqueous medium, HPS is induced to emit a strong fluorescence[64, 72]. Various other molecules have been synthesized or derivatized to molecules that exhibit the AIE phenomenon, showing a strong fluorescence upon aggregation in various forms[73, 74]. The mechanism behind AIE has been under extensive investigation, yielding several possible working mechanisms that include restricted intramolecular rotation (RIR), restricted intramolecular vibrations (RIV) and restricted intramolecular motions (RIM) which involves both RIR and RIV [64, 67]. The use of these AIE molecules spans a wide range of applications from chemical sensors to biological imaging probes in diagnosis and therapy. GFP-loaded perfluorocarbon nanoemulsions (PFCs) that enabled the visualization of these nanoparticles in CIR^{+} cells using Fluorine magnetic resonance imaging were developed[75]. Another report describes the fabrication of programmed nanoparticles that can track dendritic cells *in vivo* via the use of PLGA NPs containing near-infrared fluorophores[76]. Technological advancements can now facilitate the tracking and visualization of single nanoparticles in living cells using up-conversion particles that can transform low energy near-IR photons into high-energy visible emissions[77, 78]. Advancement of AIE has attracted the implementation of AIEgens in various technological applications[79]. Plentiful AIE

molecules are now being used as biological probes, in biomolecular sensing and biological imaging, as chemical sensors and in optoelectronic systems[64, 80-82]. Cao et. al demonstrated the use of an AIE luminogen for real-time tracking of extra-cellular vesicles in liver regeneration[83]. Photosensitizers, theranostic nanocarriers for cancer and bioprobes for real-time cell monitoring are some examples of the various applications of AIE[84-87]. Another exciting application of AIE involves the use of AIE dots which comprise of organic biocompatible nanoparticles with a dense core of AIE fluorogens. These AIE dots serve great potential as theranostic nano lights in biomedical applications[88, 89].

While various methods involving magnetic and gold nanoparticles have also been explored for cellular tracking[90, 91], we demonstrate herein, for the first time, tracking of intact antiretroviral therapeutic nanoparticles in CD4+ T cell reservoirs using AIE. Because AIE is a phenomenon that is expressed only when the molecule is in an aggregated state[64, 67] such as in a nanoparticle, this platform enables the assessment of nanoparticle integrity as well as tracking in cellular subpopulations of interest such as the CD14+ macrophages and CD4+ T cells.

1.6 ARV Biodistribution (BD) and Pharmacokinetics (PK)

Since the discovery and subsequent development of antiretroviral therapy, substantial efforts have been made to study the biodistribution and pharmacokinetics of these compounds and their formulations. The determination of the BD and PK of a drug candidate are fundamental components of drug product

development. Over the years, results from multiple clinical trials have published the evaluation of the efficacy of different antiretroviral-based strategies for the treatment and prevention of HIV[92]. The study of BD and PK is the principal component of drug and/or nanoformulation evaluation.

BD and PK have also been used to optimize antiretroviral drug-drug interactions in the treatment of HIV[93, 94]. Govil et. al deduced the mucosal pharmacokinetics of the ARV Tenofovir to create inferences about PK metrics and draw multiparametric relationships[95]. Additional biodistribution studies carried out by Kevadiya et. al demonstrated that rod-shaped nanoparticles facilitate ARV drug biodistribution in HIV susceptible calls and tissues[96]. These nanoparticles mimic the size, shape and surface properties of long-acting prodrug nanoformulations and enable real-time assessment of nanoparticle biodistribution in anatomical reservoir sites of HIV such as the liver, spleen, lungs and lymph nodes. While traditional PK methods require end-point animal sacrifice to determine drug concentrations in specific organs, they have proposed herein, a method to determine nanoparticle accumulation in organs by real-time bioimaging tests[96]. Furthermore, there is a need for useful pharmacokinetic models to predict the efficacy of compounds developed for HIV therapy. To address this need, many pharmacokinetic/pharmacodynamic (PD) models have been created to assess the efficacy of HIV drugs[97-99]. However, while PK/PD modeling has provided new insight into the efficacy and biodistribution of new compounds, challenges still abound[100, 101].

To overcome the limitations of accurate PK predictions, effective drug delivery to viral reservoir sites and methods to determine drug concentrations and track drug delivery, we have developed herein, a nanoparticle platform that enables successful tracking of fluorescent nanoparticles in cellular subpopulations. The formulation of RPV-NC ensures that RPV is in a stable, aggregated form with the molecules arranged in a definitive crystal lattice so as to emit optimal fluorescence upon excitation by UV light. Furthermore, the ability to track and sort immune cell types based on surface biomarkers enables us to separate the cellular sub-populations to determine the effective drug concentration in each of the sorted cell types. Fluorescence-concentration correlations have shown the accuracy of these assays, proving that the fluorescence emitted by the nanocrystals coincides with the concentration of drug present. This work puts forth several possibilities in the field of bioimaging and AIE with the potential to substantially improve biodistribution and therapy using AIE to track drug delivery to viral reservoir sites, as we move forward in the direction towards HIV eradication.

1.7 Figures

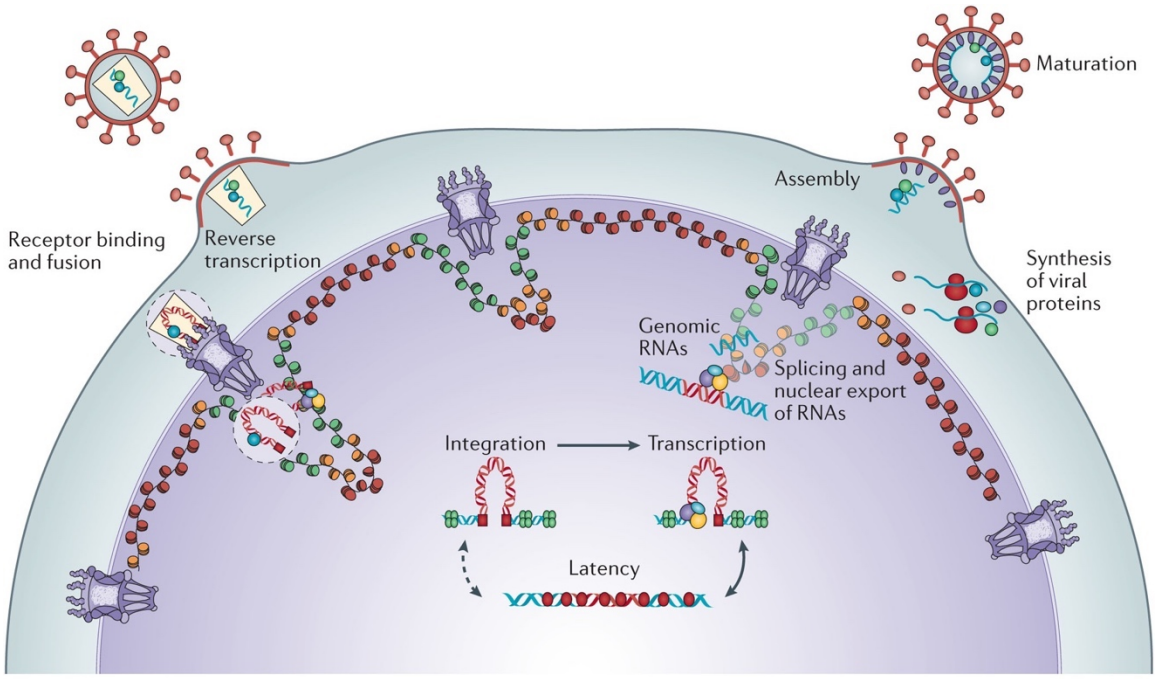

Figure 1.1 HIV life cycle and development of latency.[102]

Cellular invasion by HIV begins with the binding of the virus particle to the CD4+ T cell receptors leading to fusion and entry of viral proteins and RNA. Viral reverse transcriptase then produces viral DNA by reverse transcribing viral RNA. Transport to the nucleus is followed by integration into the host cell genome by HIV integrase. Viral DNA may enter a stage of pre-integration latency and remain silent until activation leads to integration and subsequent transcription. Alternatively, integrated viral DNA may enter a stage of post-integration latency creating silent viral reservoirs. Upon activation of these reservoirs, viral RNA is produced by transcription and undergoes splicing and assembly with viral proteins to form new virions. Figure adapted from Lusic, M., Siliciano, R. Nuclear landscape of HIV-1 infection and integration. Nat Rev Microbiol 15, 69–82 (2017).

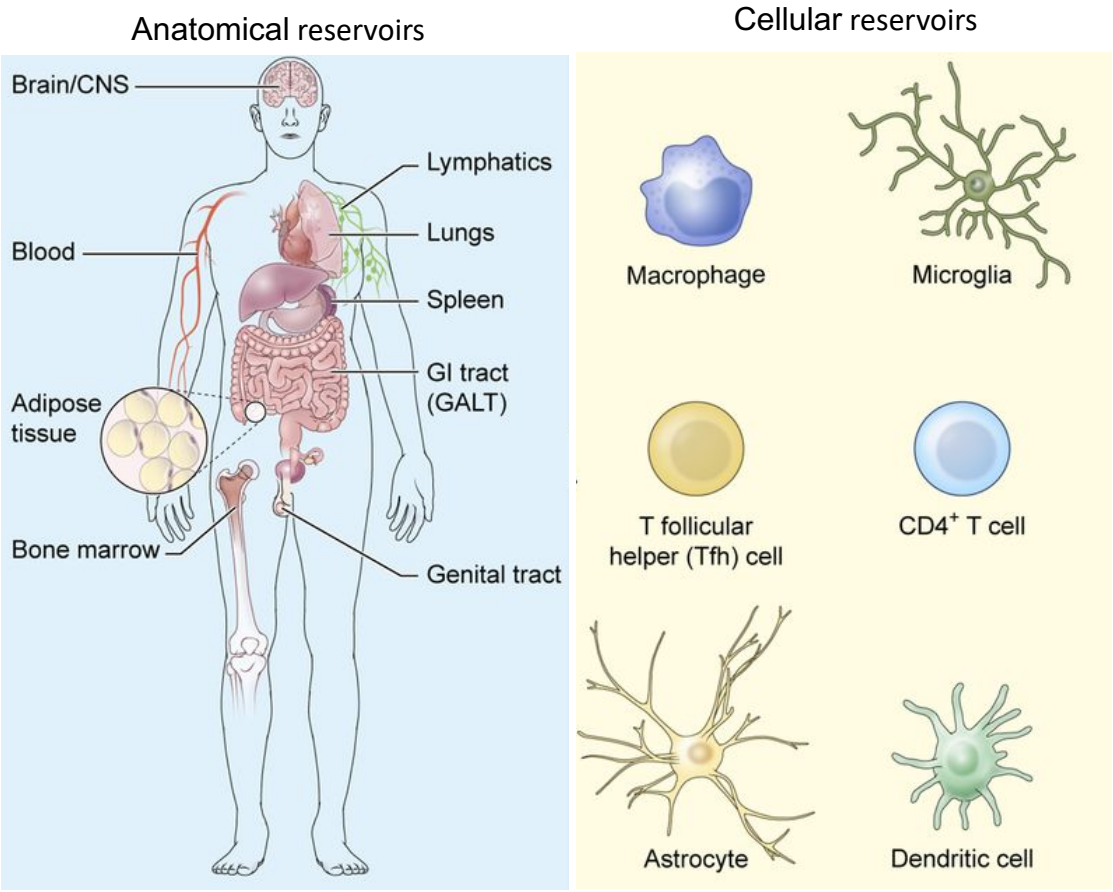

Figure 1.2 HIV viral reservoir sites.[37, 103]

The resting CD4+ T cell pool has been established as the major cellular reservoir of HIV. Macrophages, monocytes and dendritic cells are also other potential reservoir sites. Anatomical reservoir sites include the brain, gut-associated lymphoid tissue, bone marrow, and genital tract[38, 39].

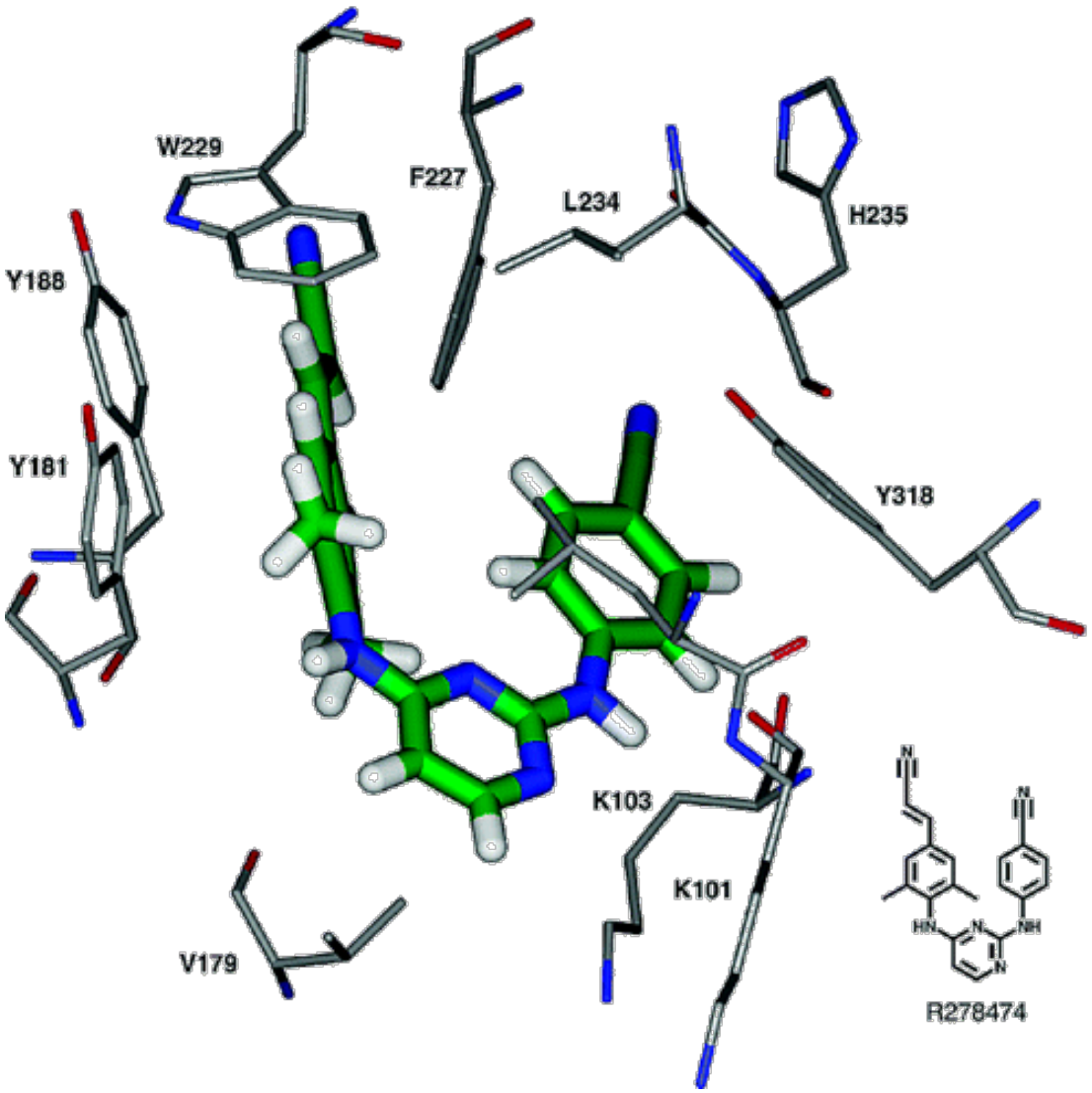

Figure 1.3 Rilpivirine (R278474) in the NNRTI-binding pocket (modeled structure).[60]

The structure of Rilpivirine within the nonnucleoside binding site of RT. The improved activity of RPV on wild-type and mutant HIV-1 strains may be due to a specific interaction involving the cyano group of the molecule and the indole ring of Trp229 on RT[60].

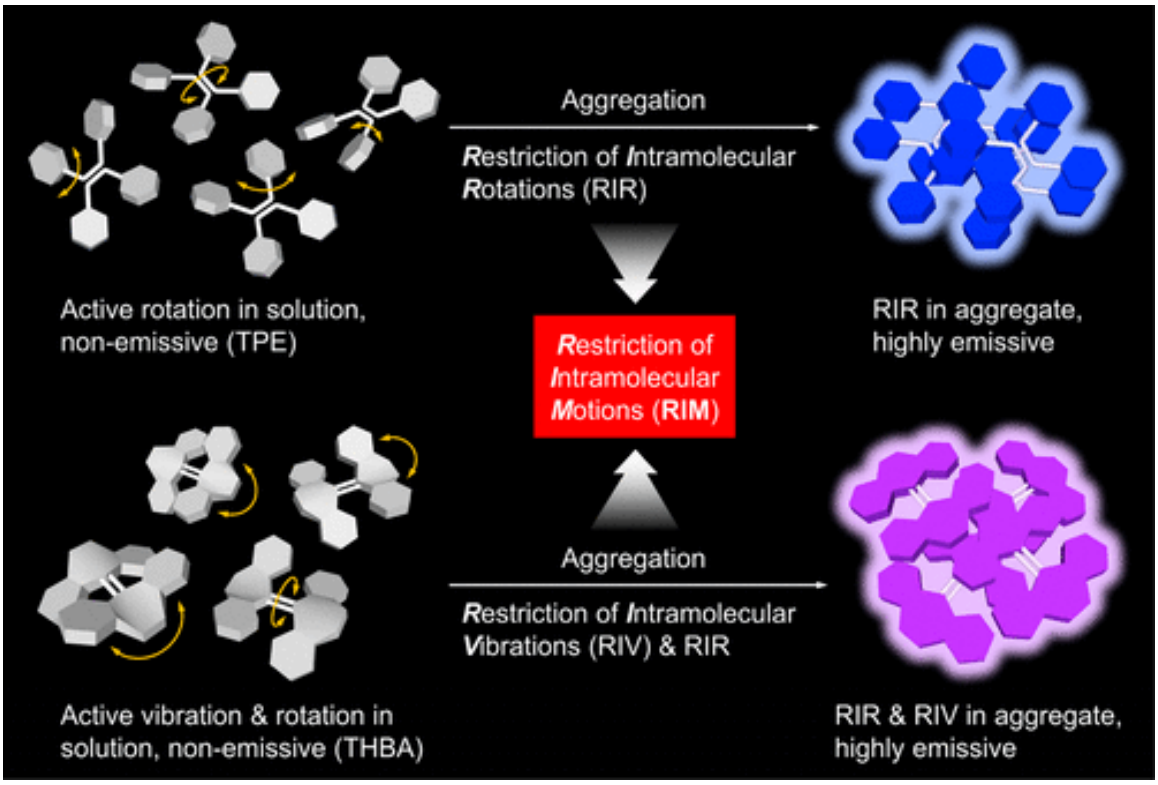

Figure 1.4 The phenomenon of Aggregation Induced Emission.

AIE is a phenomenon wherein non-emissive molecules are able to fluoresce upon excitation when in the form of aggregates or in a crystal lattice. [64-67]

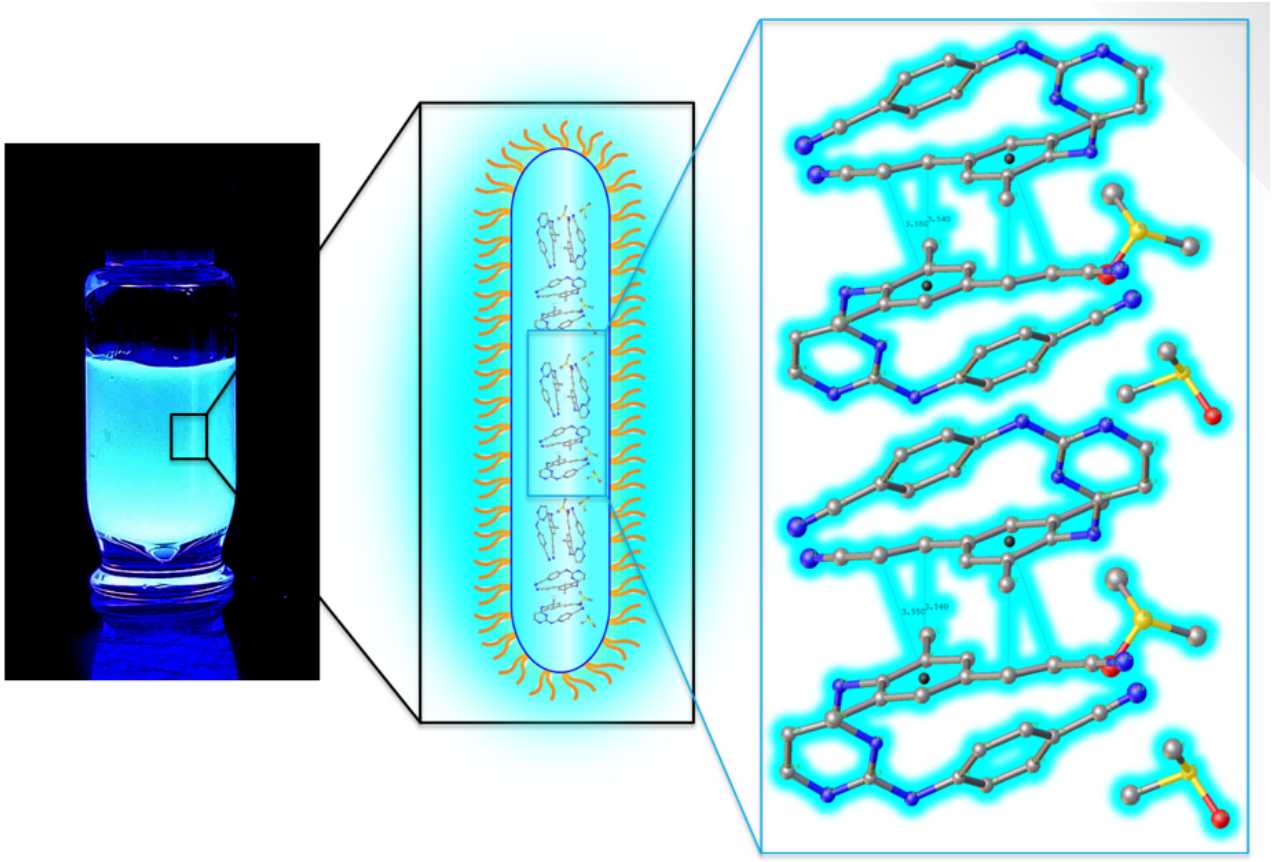

Figure 1.5 Visualizing the AIE property of Rilpivirine.

In an aggregated form, as in RPV-NC, RPV is highly emissive with a blue fluorescence upon excitation by UV light. This is due to the RIM that arises from the restricted rotation of π rings in RPV crystals that leads to fluorescent emission.

CHAPTER 2. SYNTHESIS AND CHARACTERIZATION OF RPV-NC

2.1 Introduction

The major target cells for HIV infection are the CD4+ T cell and the monocyte-macrophage [104-106]. Thus, detection of viral suppressive agents in these cells could prove valuable towards improving therapeutic and eradication designs. Indeed, the AIE properties of RPV enables drug tracking by fluorescence emission. This ability was affirmed by TEM, UPLC-MS/MS, flow cytometry and confocal microscopy (**Table 2.1**).

RPV exhibits AIE when in an aggregated form because of the restriction of intramolecular motion. A stable, uniformly ordered aggregate structure allows for optimal emission of fluorescence upon excitation. Hence, RPV-NC were formulated by a method of antisolvent precipitation[107-109] using a Smart nanotechnology bottom-up top-down approach[110]. The process of antisolvent precipitation allows for rapid crystallization of RPV into a uniform crystal structure. The micron-sized particles are then coated with a lipid film. A stable aggregate ensures maximum restriction of intramolecular motion and hence emission of fluorescence. Following stabilization, the particles are subjected to high-pressure homogenization[111] to obtain nanoparticles with a hydrodynamic diameter of about 250 – 300nm. The process of high-pressure homogenization allows for the

formation of compact, highly stable nanoparticles with a narrow polydispersity index.

The development of an AIE molecule involves various tests of photo properties and fluorescence emission[112]. Hence, RPV-NC were thoroughly characterized for physicochemical properties, fluorescence properties, as well as crystal structure. Physicochemical characterization involved TEM, XRD and TGA analyses along with stability studies by determination of PDI and hydrodynamic diameter. Characterization of fluorescence properties involved confocal microscopy images, absorption and emission spectra, photostability studies and measurements of fluorescence intensities in different conditions. The crystal structure was also elucidated in detail by x-ray crystallography. Thus, a stable platform that can be used for several potential bioimaging applications was produced.

2.2 Methods

2.2.1 Reagents

RPV was purchased from Hangzhou Bingo Chemical Co., Ltd. (Hangzhou, ZJ, China). 1, 20-Distearoyl-phosphatidylethanolaminemethyl-polyethyleneglycol conjugate 2000 (DSPE-PEG_{2000}) was obtained from Corden Pharma International (Plank Stadt, Germany). L-α-phosphatidylcholine (from egg yolk) Chloroform, Dimethyl sulfoxide, N-butanol and 3-(4,5-dimethyl-2-thiazolyl)-2,5-diphenyl-2H-tetrazolium bromide (MTT) from Sigma Aldrich (St. Louis, MO, USA).

2.2.2 Synthesis of RPV-NC

Formulation of RPV-NC followed a bottom-up top-down approach [110] wherein micron-sized crystals of RPV were prepared and then subjected to size reduction to obtain nanocrystals. Approximate 366 mg of RPV was dissolved in 400 ml of methanol and heated for 1 hour at 70°C for a complete dissolution of RPV. To obtain a saturated solution, solvent volume was reduced under vacuum in a rotavapor (Heidolph, Hei-VAP Precision, G3B Vertical, Schwabach, Germany). The saturated solution was then added to 300 ml of deionized water at 4°C in a sonication bath under rapid stirring at 2500 rpm (IKA RW 20 Digital overhead stirrer, IKA Works, Inc., Wilmington, NC, USA). The formulation was sonicated and stirred rapidly for 15 min. The white, uniform suspension obtained was purified by ultra-centrifugation at 6000 g for 30 min (Thermo Scientific™ Sorvall™ LYNX 4000 superspeed centrifuge, Waltham, MA, USA). The solid pellet

was lyophilized overnight. For the preparation of the lipid film, 200 mg of L-α-phosphatidylcholine and 100 mg of DSPE-PEG_{2000} were dissolved in a chloroform/hexane mixture (5:1 v/v) contained within a round-bottomed flask and evaporated to form a thin film using a rotavapor. The films were dried overnight to ensure complete removal of organic solvents. Lyophilized RPV crystals were dispersed in 15 ml of endotoxin-free water, added to the prepared lipid film and sonicated for 5 min to obtain a uniform surface coating. The mixture was then homogenized at 20,000 psi in an Avestin EmulsiFlex-C3 high-pressure homogenizer (Ottawa, ON, Canada) until the desired particle size was reached (~320 nm). Suspensions were stored at room temperature in amber vials for light protection.

2.2.3 Transmission electron microscopy (TEM), powder X-ray diffraction (XRD), thermal analysis and stability measurements

Nanoparticle morphology was analyzed by TEM. Nanoparticle suspensions were dried on a copper grid at room temperature and bright-field images were taken with two second exposure times using the Tecnai G2 Spirit TWIN electron microscope (FEI, Houston, TX, USA) operating at 80 kV. Images were acquired with an AMT digital imaging system [113]. Analyses were carried out with XRD using a PANalytical Empyrean diffractometer (PANalytical, Inc., Westborough, MA, USA). This was performed in the 2θ range of 2– 70° with Cu-Kα radiation (1.5418 Å) at 40 kV, 45 mA setting. The incident beam path used a mask of 20 mm and a divergence slit of 1/32°. A layer of the powder was placed on a zero-background

silicon plate. The sample holder was then spun at the rate of 22.5 deg/sec. During data collection, the solid state PIXcel3D detector (PANalytical, Inc., Westborough, MA, USA) scanned at a rate of 0.053 deg/sec. The PIXcel3D used a beam monochromator used to improve the signal to noise ratios. Thermogravimetric analysis was performed under a nitrogen flow of 20 ml/min at a temperature of 30–600°C and a heating rate of 10°C/min (TGA 209 F1 Libra, Netzsch-Gerätebau GmbH, Selb, Germany). The stability of the RPV-NC nanoparticle suspension was assessed for 3 weeks at 4°C recording hydrodynamic particle size distribution.

2.2.4 Spectral measurements and drug quantifications

For confocal microscopy, single crystals of RPV-NC were imaged using a 20x oil objective on an LSM 710 confocal microscope (Carl Zeiss Microimaging, Inc., Dublin, CA, USA). Zeiss LSM 710 Image browser AIM software version 4.2 was used to determine pixel numbers and the mean channel intensities. Absorption spectra of dilute RPV suspensions were recorded on Thermo Scientific Evolution 220 spectrophotometer in quartz cuvettes with the optical path length of 1 cm. Fluorescence spectroscopy measurements were performed at 350 nm excitation by SpectraMax® M3 Multi-Mode Microplate Reader (Molecular Devices, LLC, Sunnyvale, CA, USA), or on the Fluoromax 4 (Horiba Jobin Yvon, Kyoto, Japan) fluorometer (λ_{exc}=335 nm) in quartz cuvettes with the optical path length of 1 cm. Fluorescence quantum yields were determined using quinine sulfate in 0.5 M H_2SO_4 as a standard (φ=0.546 [114]). The photostability of RPV-NC was studied under a UV lamp (4 W, λ=365 nm, broadband filter) with constant stirring. Analysis

of RPV concentrations was carried out by UPLC using a Waters Acquity UPLC H-Class System with TUV detector and Empower 3 software (Waters, Milford, MA, USA). Sample separation was done on a Phenomenex Kinetex 5 µm C18 column (150 X 4.6 mm, Phenomenex Ltd., Torrance, CA, USA) using an isocratic mobile phase of 65% 50 mM KH_2PO_4, pH 3.2 / 35% acetonitrile at a flow rate of 1.0 ml/min and detection at 285 nm. Drug content was quantitated by comparison of the peak area to those of known standards (0.05–50 µg/ml in methanol) [115, 116]. All flow cytometry data were acquired on a BD LSR II flow cytometer and analyzed using FLOWJO analysis software v10.2 (Tree Star, Ashland, OR, USA) and BD FACSDiva™ Software v8 (BD Biosciences, San Jose, CA, USA). Untreated and single stained controls were used to assign gates for nanoparticle positive populations. Light microscopy images of the particles were taken using a Nikon TE300 microscope (Nikon Instrument, Inc., Melville, NY, USA) with a 20x objective. Polarized microscopy images were taken using an Olympus BX51 (Olympus Scientific Solutions Americas Corp., Waltham, MA, USA) polarizing microscope at 90° polarized light.

2.2.5 Single-crystal x-ray diffraction

Single crystals for x-ray diffraction were prepared from a saturated solution of RPV in a mixture of dimethylsulfoxide (DMSO; 75%) and n-butanol (25%). A suitable crystal was selected and mounted on a Kryoloop using paratone oil on an Xcalibur, Onyx, Ultra Diffractometer (Oxford Diffraction Limited, Oxfordshire, UK). The crystal was kept at 100 K during data collection. Using OLEX2[117], the structure

was solved with the SHELXS[118] structure solution program using Direct Methods and refined with the SHELXL[119] refinement package using Least Squares minimization.

2.2.6 Statistics

For all studies, data were analyzed using GraphPad Prism 7.0 software (La Jolla, CA) and presented as the mean ± the standard error of the mean (SEM). For comparisons of two groups, Student's *t-test* (two-tailed) was used. HIV-1 RT activity and HIV-1p24 staining were analyzed by one-way ANOVA with Bonferroni correction for multiple comparisons. Extreme outliers beyond the 99% confidence interval of the mean and 3-fold greater than the SEM were excluded. Significant differences were determined at $P < 0.05$.

2.3 Results

2.3.1 RPV-NC preparation

RPV-NC were formulated by Smart nanotechnology [110] (**Figure 2.1 A**). Micron-sized particles were prepared by anti-solvent precipitation.[107-109] A consistent molecular RPV crystal structure was achieved. Based on RPV solubility in methanol, a saturated drug solution was prepared by heating. The solution was then rapidly added to ice-cold water under bath sonication and high-speed shearing. The homogenous suspension of particles was purified by high-speed ultra-centrifugation and freeze-dried. Lyophilized particles were dispersed in water and coated with a lipid film containing DSPE-PEG_{2000} and phosphatidylcholine (α-PC) to impart stability and lipophilicity. The suspension was subjected to high-pressure homogenization for size reduction and nanocrystal formation.[111]

2.3.2 Physicochemical characterization

The physicochemical properties, fluorescence and structural features of these nanocrystals were studied by various analytical techniques. TEM images taken before homogenization showed micron-sized, 'flower-shaped' crystals accumulated in clusters **Figure 2.1 B** and **C** [120]. **Figure 2.1 D** demonstrates that the nanocrystals had a uniform shape and smooth surface with a particle size of approximately 200 nm after homogenization. To ensure that crystal structure was retained, powder x-ray diffraction (XRD) analysis was performed for native RPV and for RPV crystals before and after homogenization. As shown in **Figure 2.1 E**,

F and **G**, the characteristic diffraction peaks of native RPV (**Figure 2.1 E**) at 12.4°, 17.5°, 20.1°, 21.1° and 27.9° at 2° positions were maintained in the RPV crystals before (**Figure 2.1 F**) and after homogenization (**Figure 2.1 G**). This was also seen in RPV-NC after storage for 21 days at 25°C (**Figure 2.2**). The lack of a shift in the x-ray diffraction patterns demonstrates that the crystalline nature of native RPV in the free drug form was preserved in the microcrystals as well as in the homogenized nanoparticles. The thermal stability of the formulated and native drug was shown by thermogravimetric analysis (TGA) analysis. The isothermal heating distribution curve of TGA showed an endothermic peak at 444.22°C and 442.78°C due to the complete degradation of native RPV and RPV-NC, respectively. TGA is represented as a derivative thermal analysis (DTA) in **Figure 2.1 H** and shows the unchanged thermal properties of RPV-NC with respect to native RPV. The stability of RPV-NC in suspension at room temperature was monitored by dynamic light scattering (DLS). The zeta potential was found to be -24.9mV and as shown in **Figures 2.1 I** and **J**, the particle size, represented by hydrodynamic diameter, and polydispersity index (PDI) remained constant at 320 nm and 0.2, respectively, for a period of 21 days.

2.3.3 AIE properties

In its aggregated form, RPV emits blue fluorescence when excited by UV light. This unique property can be used to monitor particle integrity. The AIE properties of RPV were characterized by various methods [64, 70]. Confocal microscopy images of the RPV crystals overlapped with bright-field microscopic

images displayed uniformity of fluorescence emission (**Figure 2.3 A**). Since RPV is freely soluble in methanol, the AIE phenomenon of RPV-NC was studied in various ratios of water/methanol. The shift towards longer wavelengths and the broader width of the peak suggests that it should be attributed to the absorption of the RPV aggregates. The isosbestic point at approximately 325 nm supports the conclusion that these two absorption peaks are related **(Figure 2.3 B)**. Similar conclusions can be made from the analysis of the RPV emission spectra (λ_{exc}=335 nm) in the same solvent systems (**Figure 2.3 C**). There is no detectable fluorescence from RPV in its solution in methanol. Upon the increase of water content to 50%, blue fluorescence rises with a maximum at 385 nm. It reaches its maximum intensity at ~70% water content, and then somewhat decreases, potentially due to partial quenching induced by interactions with water [121]. Measurements of fluorescence quantum yield in solvent systems with varying amounts of methanol (%v/v) yielded a sigmoidal curve with a high goodness of fit (R^2 = 0.9981; **Figure 2.3 D**), a trend that was visually discernable (**Figure 2.3 E**). Analysis of RPV levels in supernatants of these samples showed an inverse relationship between drug concentration and fluorescence intensity (**Figure 2.3 F**). As the particles dissolve rapidly in 50% methanol, the fluorescence intensity drops significantly.

Further characterization of the AIE properties and its fluorescence stability important for prospective theranostic applications was carried out by measuring fluorescence intensities in different conditions. Emission of RPV-NC remained stable over a pH range of 2 to 14 but rapidly declined at pH 1 due to the complete

disintegration of RPV aggregates (**Figure 2.3 G**). The photostability studies revealed that the fluorescence intensity of RPV-NC only decreases by approximately 30% over the course of 6 hours of constant irradiation (**Figure 2.3 H**). The associated absorption and emission spectra (**Figure 2.4**) do not show any apparent photooxidation or other degradation processes that affect RPV-NC performance. These observations demonstrate that RPV-NC exhibit AIE.

2.3.4 Elucidation of crystal structure

Several agents that exhibit the AIE property via RIM have previously been reported [64, 65, 67]. To understand the mechanism of AIE exhibited by RPV, single-crystal x-ray diffraction studies were performed (**Figure 2.5 C**). Single crystals of RPV were grown from a mixture of two solvents to obtain clear micron-sized crystals (**Figure 2.5 A**). By polarized microscopy, the optically anisotropic character of the crystals was observed (**Figure 2.5 B**). X-ray crystallographic data revealed that two RPV molecules crystallized in a single cell unit (**Figure 2.5 D**). Displacement parameters, structure refinement and crystal data from x-ray studies are described (**Table 2.2 – 2.8**). Examination of the packing diagram revealed several close CH-π interactions for adjacent RPV molecules within the crystalline lattice. These contacts ranged from 2.96 - 3.5 Å. Similar intramolecular distances were observed for hexaphenylsilole (HPS) whose crystal structure showed intramolecular distances between C-H bonds and π rings of 2.587 - 3.642 Å [64, 72]. Taken together, these data suggest that restricted rotation of π rings in RPV

crystals enable fluorescent emission by a RIM mechanism similar to that observed in other compounds [65].

2.4 Discussion

The AIE properties of RPV were hence discovered and studied in depth. To confer a purpose to the AIE property of RPV, RPV-NC were synthesized by a Smart nanotechnology bottom-up top-down approach involving anti-solvent precipitation to obtain stable, uniform nanocrystals. These nanocrystals were observed to be stable for a period of weeks. Nanocrystal morphology and surface topology was studied by TEM and SEM, respectively. Other characteristics such as thermal stability and the crystalline nature of the molecule within the nanocrystals were also studied.

Determination of AIE properties involved qualitative assessments of large micron-sized crystals of RPV by confocal microscopy to be able to visualize the fluorescence emission of the crystals upon excitation by UV light. Spectral measurements were also carried out to determine the maximum wavelength of emission as well as the absorption and emission spectra. Thus, a new property of the antiretroviral compound, RPV, was established.

Crystal structure elucidation by x-ray crystallography uncovered several intramolecular interactions in the nanocrystals. The distances observed between the C-H bonds and π rings of RPV molecules show that significant intermolecular interactions exist between adjacent molecules. These non-covalent interactions hold the RPV molecules together, stabilizing the crystal packing and restricting the rotational motion of the phenyl rings. While similar intramolecular distances have been observed in other AIEgenic molecules, the intermolecular interactions in RPV have a similar effect on the intramolecular rotations. Hence, the restricted rotation

of π rings in RPV crystals enables fluorescent emission by a RIM mechanism similar to that observed in other compounds [65].

2.5 Figures

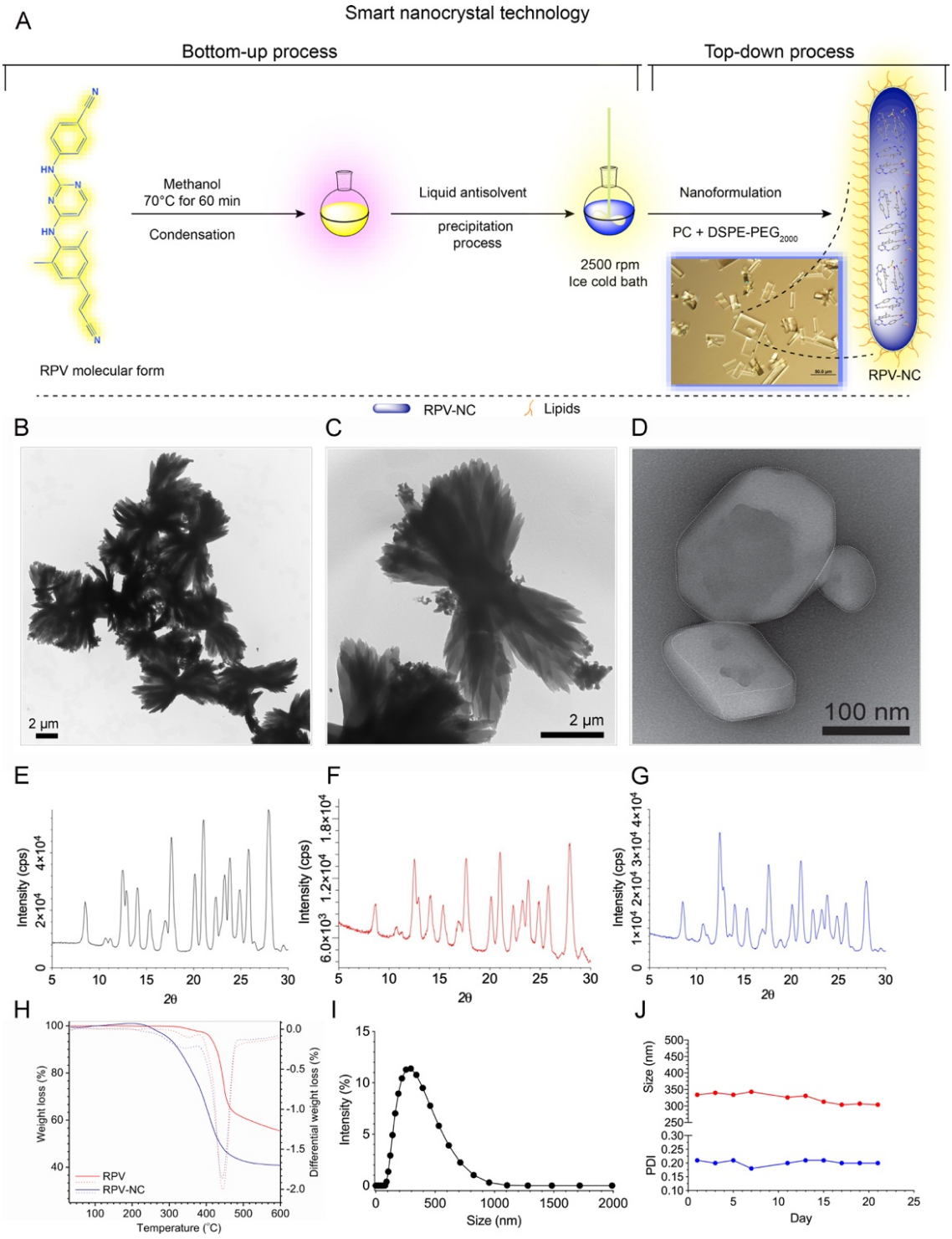
A
Smart nanocrystal technology
Bottom-up process
Top-down process
Methanol
70°C for 60 min
Condensation
Liquid antisolvent
precipitation
process
2500 rpm
Ice cold bath
Nanoformulation
PC + DSPE-PEG2000
RPV molecular form
RPV-NC
RPV-NC
Lipids
B
C
D
2 μm
2 μm
100 nm
E
F
G
Intensity (cps)
2θ
H
I
J
Weight loss (%)
Differential weight loss (%)
Temperature (°C)
RPV
RPV-NC
Intensity (%)
Size (nm)
PDI
Day

Figure 2.1 RPV-NC synthesis and physical characterizations.

(A) Schematic representation of the Smart nanotechnology used to formulate RPV-NC by bottom-up and top-down approaches. **(B)** Low and **(C)** high magnification TEM images showing the morphology of RPV crystals made by anti-solvent precipitation. **(D)** TEM image of RPV-NC shows uniform surface morphology after homogenization. **(E, F, G)** XRD patterns of native RPV, RPV-NC before and after homogenization, respectively. **(H)** TGA analysis of native RPV and RPV-NC. **(I)** The hydrodynamic size distribution of RPV-NC is shown by DLS (average size ~ 320 nm). **(J)** The stability of RPV-NC was determined by size and PDI measurements over a three-week time period.

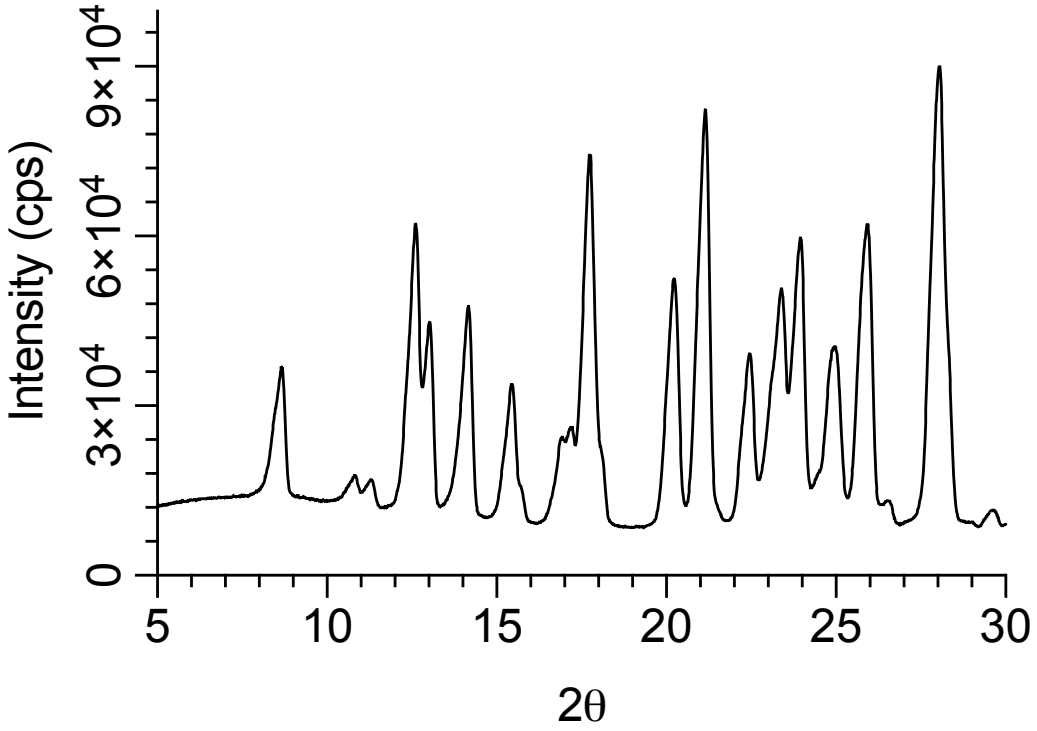

Figure 2.2 XRD pattern of RPV-NC.

The characteristic diffraction peaks of native RPV at 12.4°, 17.5°, 20.1°, 21.1° and 27.9° at 2° positions were maintained in RPV-NC after storage for 21 days at 25°C.

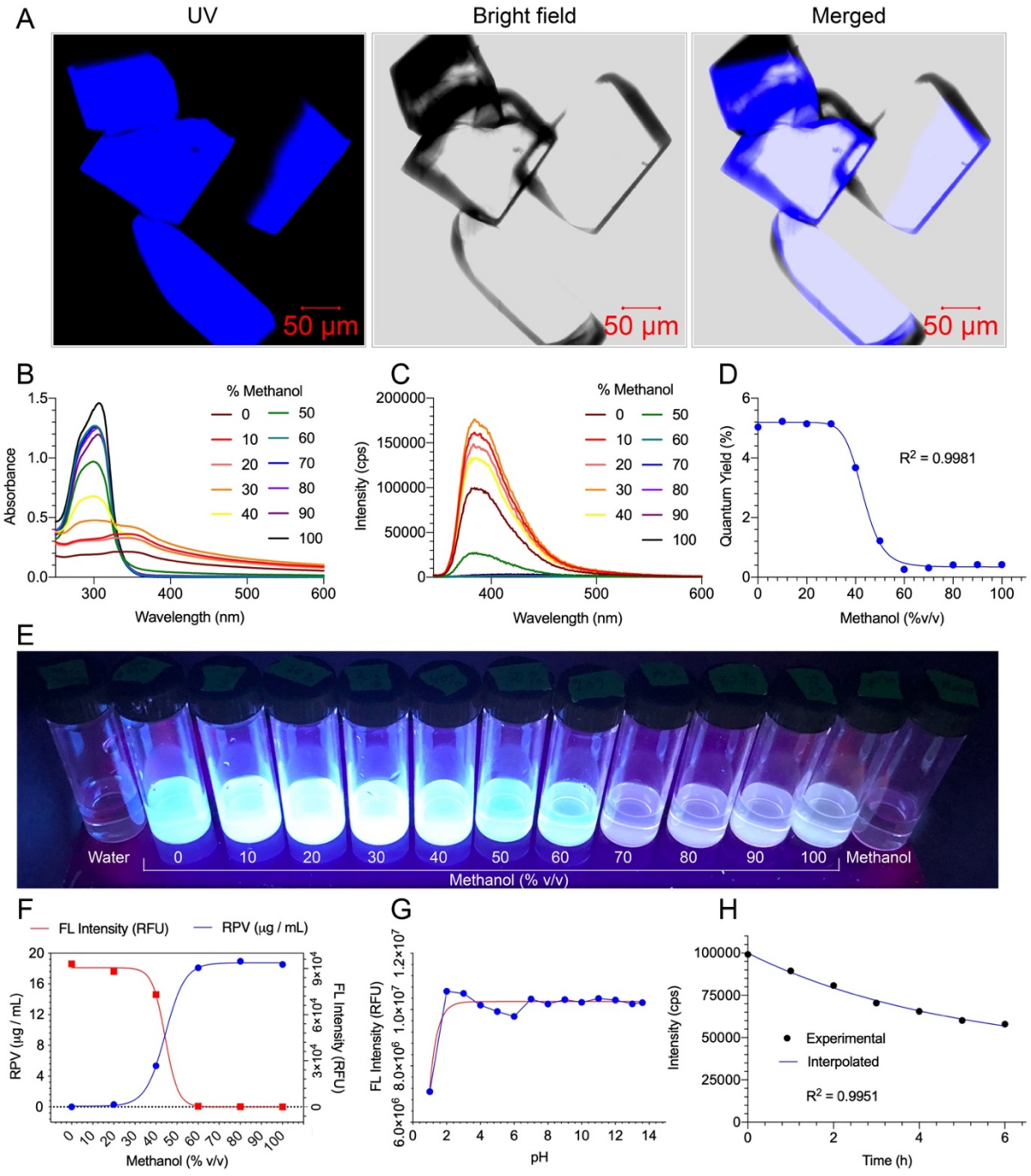
A
UV
Bright field
Merged
50 µm
50 µm
50 µm
B
Absorbance
Wavelength (nm)
% Methanol
0
10
20
30
40
50
60
70
80
90
100
C
Intensity (cps)
Wavelength (nm)
% Methanol
D
Quantum Yield (%)
R2 = 0.9981
Methanol (%v/v)
E
Water
Methanol
Methanol (% v/v)
F
FL Intensity (RFU)
RPV (µg / mL)
RPV (µg / mL)
FL Intensity (RFU)
Methanol (% v/v)
G
FL Intensity (RFU)
pH
H
Intensity (cps)
Experimental
Interpolated
R2 = 0.9951
Time (h)

Figure 2.3 Fluorescence characteristics of RPV-NC.

(A) Confocal and bright-field images of RPV-NC merged to show fluorescence distribution. **(B)** Absorption spectra of RPV-NC in water/methanol ratios. **(C)** Corresponding fluorescence spectra of RPV-NC in water/methanol ratios. **(D)** Fluorescence quantum yield in water/methanol ratios. **(E)** RPV-NC in water/methanol ratios upon UV excitation. **(F)** Fluorescence (FL) intensity and concentration of RPV in various methanol/water ratios. **(G)** Fluorescence intensity of RPV-NC at different pH. **(H)** Photostability of RPV-NC.

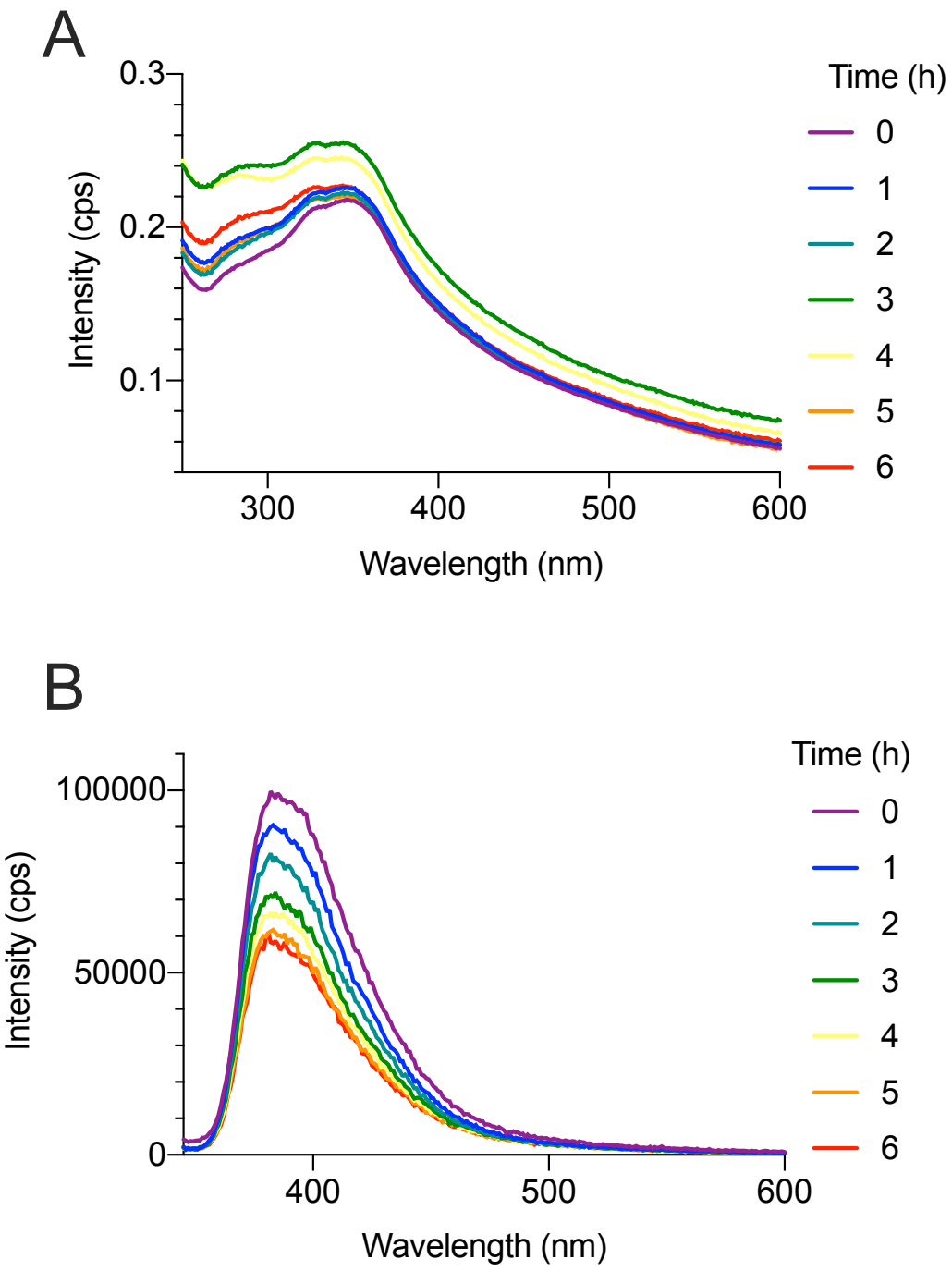

Figure 2.4 Photostability associated spectra.

(A) Absorption spectra of RPV-NC in 100% water over 6h. (B) Corresponding fluorescence emission spectra of RPV-NC.

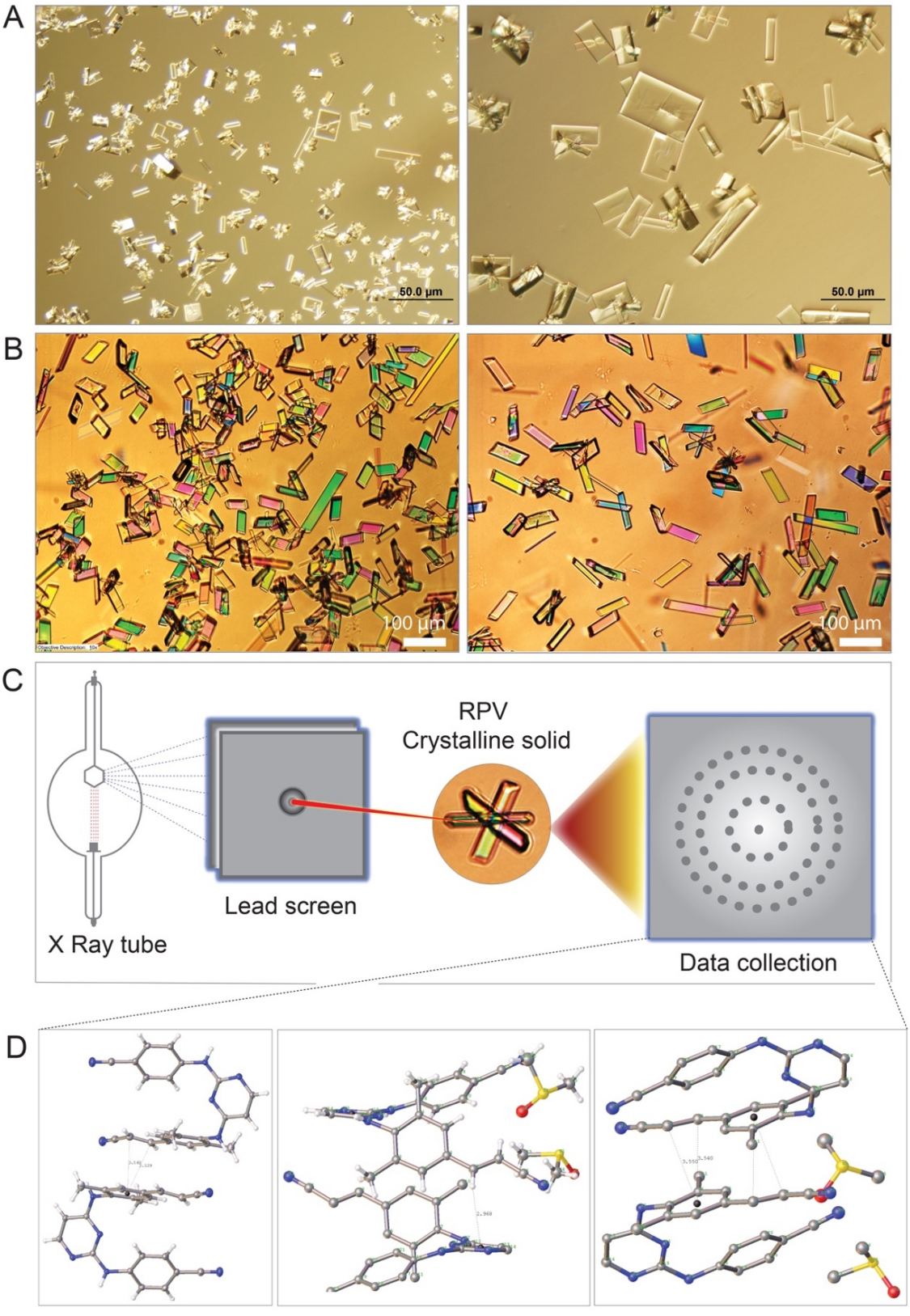
A
50.0 µm
50.0 µm
B
100 µm
100 µm
C
RPV
Crystalline solid
Lead screen
X Ray tube
Data collection
D

Figure 2.5 Single crystal x-ray RPV-NC crystallography.

(A) Light microscopy images of single crystals of RPV. **(B)** Polarized microscopy images of single crystals of RPV. **(C)** Schematic representation of single crystal x-ray crystallography setup. **(D)** Molecular conformation of RPV in RPV-NC showing the intermolecular CH-π interactions.

2.6. Tables

Table 2.1 Methods of analysis of RPV AIE in cells and in rodent animal models.

The table names the tests used to affirm RPV AIE. TEM, UPLC-MS/MS, flow cytometry and confocal microscopy tests were used for drug tracking using fluorescence emission tests.

	Models	Dose	Methods of Analysis			
			TEM	UPLC-MS/MS	Flow cytometry	Confocal microscopy
In vitro	Macrophages	100μM	+	+	+	+
	T cells		+	+	+	+
In vivo	Sprague-Dawley rats	45mg/kg	-	+	-	+
	PBL mice		-	+	-	+
	Humanized mice		-	+	+	-

Table 2.2 Crystal data and structure refinement for Rilpivirine.

IDENTIFICATION CODE	Rilpivirine
EMPIRICAL FORMULA	$C_{22}H_{18}N_6$, 2(C_2H_6OS)
FORMULA WEIGHT	366.4 + (2*78.13) = 522.68
TEMPERATURE/K	100
CRYSTAL SYSTEM	triclinic
SPACE GROUP	P-1
A/Å	8.41354(18)
B/Å	11.8546(2)
C/Å	13.7483(2)
A/°	79.7407(16)
B/°	89.0890(16)
Γ/°	80.1013(17)
VOLUME/Å^3	1329.08(5)
Z	2
P_{CALC}G/CM^3	1.306
M/MM^{-1}	2.098
F(000)	552.0
CRYSTAL SIZE/MM^3	0.25 × 0.25 × 0.1
RADIATION	CuKα (λ = 1.54184)
2Θ RANGE FOR DATA COLLECTION/°	6.534 to 151.482
INDEX RANGES	-10 ≤ h ≤ 10, -14 ≤ k ≤ 14, -17 ≤ l ≤ 17
REFLECTIONS COLLECTED	46467
INDEPENDENT REFLECTIONS	5442 [R_{int} = 0.0559, R_{sigma} = 0.0235]
DATA/RESTRAINTS/PARAMETERS	5442/0/331
GOODNESS-OF-FIT ON F^2	1.061
FINAL R INDEXES [I>=2Σ (I)]	R_1 = 0.0507, wR_2 = 0.1334
FINAL R INDEXES [ALL DATA]	R_1 = 0.0551, wR_2 = 0.1415
LARGEST DIFF. PEAK/HOLE / E Å^{-3}	1.82/-0.60

Table 2.3 Fractional Atomic Coordinates (×104) and Equivalent Isotropic Displacement Parameters (Å2×103) for Rilpivirine. Ueq is defined as 1/3 of the trace of the orthogonalized UIJ tensor.

Atom	*x*	*y*	*z*	U(eq)
S1	1559.0(6)	-3482.0(4)	9649.8(3)	20.58(14)
S2	5373.9(7)	-2653.0(5)	11209.0(4)	31.54(16)
N4	-1219.6(19)	-1927.4(13)	15538.4(11)	14.9(3)
N5	-3062(2)	-749.5(14)	14375.7(12)	17.1(3)
N3	-3701(2)	-849.7(14)	16012.6(12)	18.3(3)
N2	644(2)	-3029.4(14)	16709.7(11)	16.8(3)
O2	3754(2)	-2875.0(16)	11607.9(13)	37.2(4)
C15	-2621(2)	-1202.6(15)	15350.4(13)	15.1(4)
C16	-2022(2)	-629.9(16)	13571.5(13)	15.7(4)
C7	1469(2)	-3674.6(16)	16012.2(13)	15.8(4)
C19	-70(2)	-229.3(17)	11923.3(14)	18.6(4)
C21	-643(2)	-1439.8(16)	13448.1(14)	17.3(4)
C20	326(2)	-1232.8(17)	12632.8(14)	19.1(4)
C12	-777(2)	-2285.6(16)	16490.5(13)	14.9(4)
C17	-2427(2)	369.4(17)	12840.7(14)	18.4(4)
C18	-1468(3)	569.7(17)	12026.4(14)	19.8(4)
N1	5720(2)	-6798.3(17)	12013.7(14)	30.0(4)
C5	2998(2)	-3805.1(18)	14537.8(14)	19.2(4)
C22	984(3)	24.4(18)	11109.6(15)	23.1(4)
N6	1832(3)	263.6(18)	10469.9(14)	32.0(4)
C4	2973(2)	-5001.0(18)	14664.1(14)	20.1(4)
C13	-1771(2)	-1921.7(17)	17252.9(14)	18.5(4)
C14	-3209(2)	-1230.1(17)	16965.1(14)	19.1(4)
C6	2287(2)	-3131.2(17)	15214.9(14)	17.3(4)
C9	2229(3)	-5522.1(17)	15490.3(15)	21.4(4)
C8	1459(2)	-4873.8(17)	16167.2(14)	19.7(4)
C3	3746(3)	-5738.7(18)	13978.6(15)	21.9(4)
C11	2501(3)	-1882.9(18)	15119.2(15)	22.8(4)
C2	4332(3)	-5362.8(18)	13099.7(16)	23.8(4)
C1	5100(3)	-6169.5(19)	12504.5(15)	24.6(4)
C10	640(3)	-5458.8(19)	17048.1(16)	27.5(5)
C25	5041(3)	-1881(2)	9975.6(18)	34.0(5)
C26	5815(4)	-1472(3)	11738(2)	45.4(7)
O1	591.6(19)	-3814.0(14)	8864.9(10)	27.6(3)
C24	2677(3)	-4809(2)	10302.6(19)	33.3(5)
C23	179(3)	-3171(2)	10604.5(17)	31.8(5)

Table 2.4 Anisotropic Displacement Parameters (Å2×103) for Rilpivirine. The Anisotropic displacement factor exponent takes the form: -2π2[h2a*2U11+2hka*b*U12+…].

Atom	U_{11}	U_{22}	U_{33}	U_{23}	U_{13}	U_{12}
S1	23.6(3)	22.0(2)	16.0(2)	-0.61(17)	1.87(18)	-6.28(19)
S2	33.0(3)	25.7(3)	36.4(3)	-7.2(2)	-4.6(2)	-3.9(2)
N4	15.1(8)	14.7(7)	14.0(7)	-2.1(6)	1.2(6)	0.0(6)
N5	12.7(8)	20.8(8)	14.7(7)	-0.5(6)	0.6(6)	2.4(6)
N3	15.9(8)	20.6(8)	16.5(8)	-2.4(6)	2.2(6)	1.4(6)
N2	17.2(8)	19.6(8)	11.9(7)	-3.7(6)	-0.3(6)	2.6(6)
O2	42.5(11)	36.3(9)	33.8(9)	3.3(7)	-3.0(7)	-19.3(8)
C15	16.6(9)	13.7(8)	14.9(8)	-1.7(6)	0.3(7)	-3.5(7)
C16	15.6(9)	17.1(9)	14.7(8)	-3.7(7)	0.5(7)	-3.1(7)
C7	12.6(9)	19.2(9)	14.0(8)	-4.6(7)	-0.5(7)	3.2(7)
C19	19.5(10)	21.7(9)	15.5(9)	-3.7(7)	1.9(7)	-5.8(8)
C21	19.4(10)	15.9(8)	16.0(9)	-2.8(7)	0.3(7)	-1.2(7)
C20	19.8(10)	19.7(9)	17.3(9)	-5.1(7)	1.7(7)	-0.6(8)
C12	14.1(9)	14.9(8)	15.9(8)	-2.8(7)	0.5(7)	-2.5(7)
C17	18.4(10)	17.1(9)	18.3(9)	-2.1(7)	-0.1(7)	-0.5(7)
C18	22.6(10)	18.0(9)	17.4(9)	1.1(7)	-1.9(7)	-4.1(8)
N1	31.5(11)	32.1(10)	25.2(9)	-8.8(8)	7.5(8)	1.6(8)
C5	14.9(10)	25.2(10)	16.5(9)	-3.0(7)	2.0(7)	-1.8(8)
C22	23.2(11)	23.9(10)	21.8(10)	-2.8(8)	1.3(8)	-4.0(8)
N6	31.3(11)	36.5(11)	26.4(10)	-0.1(8)	9.2(8)	-7.5(9)
C4	16.7(10)	24.2(10)	19.0(9)	-6.7(8)	-0.5(7)	0.8(8)
C13	19.4(10)	22.3(9)	13.1(8)	-3.7(7)	1.7(7)	-1.4(8)
C14	17.3(10)	23.1(9)	15.8(9)	-4.9(7)	3.6(7)	0.4(8)
C6	13.5(9)	20.2(9)	17.1(9)	-2.5(7)	-1.5(7)	-0.3(7)
C9	22.6(11)	18.2(9)	23.4(10)	-6.0(8)	0.4(8)	-1.0(8)
C8	19.4(10)	20.5(9)	18.1(9)	-3.2(7)	-0.7(7)	-1.1(8)
C3	21.7(11)	20.4(9)	23.2(10)	-5.5(8)	1.9(8)	-1.5(8)
C11	23.7(11)	21.9(10)	23.6(10)	-4.3(8)	2.7(8)	-5.7(8)
C2	25.5(11)	20.7(10)	23.3(10)	-3.9(8)	1.1(8)	1.3(8)
C1	23.6(11)	28(1)	19.9(9)	-3.0(8)	0.4(8)	0.4(9)
C10	35.1(13)	22.3(10)	25.6(11)	-3.5(8)	7.0(9)	-7.4(9)
C25	32.0(13)	41.4(13)	31.6(12)	-7.7(10)	3.5(10)	-14.1(11)
C26	52.2(18)	54.2(17)	40.4(14)	-20.4(13)	-0.3(12)	-26.1(14)
O1	28.5(9)	38.1(9)	16.0(7)	-1.1(6)	-3.5(6)	-8.4(7)
C24	32.4(13)	27.5(11)	37.8(13)	-4.9(10)	-11.5(10)	1.2(10)

C23	33.2(13)	37.0(12)	25.5(11)	-7.4(9)	6.2(9)	-5.4(10)

Table 2.5 Bond Lengths for Rilpivirine.

Atom	Atom	Length/Å		Atom	Atom	Length/Å
S1	O1	1.5070(15)		C19	C20	1.392(3)
S1	C24	1.784(2)		C19	C18	1.400(3)
S1	C23	1.784(2)		C19	C22	1.438(3)
S2	O2	1.5083(19)		C21	C20	1.387(3)
S2	C25	1.779(3)		C12	C13	1.412(3)
S2	C26	1.782(3)		C17	C18	1.380(3)
N4	C15	1.333(3)		N1	C1	1.148(3)
N4	C12	1.340(2)		C5	C4	1.401(3)
N5	C15	1.383(2)		C5	C6	1.395(3)
N5	C16	1.402(2)		C22	N6	1.150(3)
N3	C15	1.345(3)		C4	C9	1.387(3)
N3	C14	1.353(3)		C4	C3	1.468(3)
N2	C7	1.430(2)		C13	C14	1.361(3)
N2	C12	1.361(2)		C6	C11	1.504(3)
C16	C21	1.402(3)		C9	C8	1.393(3)
C16	C17	1.406(3)		C8	C10	1.503(3)
C7	C6	1.403(3)		C3	C2	1.329(3)
C7	C8	1.401(3)		C2	C1	1.432(3)

Table 2.6 Bond Angles for Rilpivirine.

Atom	Atom	Atom	Angle/˚		Atom	Atom	Atom	Angle/˚
O1	S1	C24	106.13(10)		C21	C20	C19	120.47(19)
O1	S1	C23	106.18(11)		N4	C12	N2	118.44(16)
C24	S1	C23	97.70(12)		N4	C12	C13	121.09(17)
O2	S2	C25	107.06(11)		N2	C12	C13	120.46(17)
O2	S2	C26	105.76(13)		C18	C17	C16	120.86(18)
C25	S2	C26	96.91(13)		C17	C18	C19	119.80(18)
C15	N4	C12	116.86(16)		C6	C5	C4	121.72(18)
C15	N5	C16	126.50(17)		N6	C22	C19	177.6(2)
C15	N3	C14	113.97(17)		C5	C4	C3	123.00(18)
C12	N2	C7	122.57(15)		C9	C4	C5	118.69(18)
N4	C15	N5	118.45(17)		C9	C4	C3	118.27(18)
N4	C15	N3	127.17(17)		C14	C13	C12	116.28(17)
N3	C15	N5	114.39(17)		N3	C14	C13	124.42(18)
N5	C16	C21	124.50(17)		C7	C6	C11	121.70(17)
N5	C16	C17	116.61(17)		C5	C6	C7	117.98(17)
C21	C16	C17	118.88(17)		C5	C6	C11	120.19(18)
C6	C7	N2	121.21(17)		C4	C9	C8	121.39(19)
C8	C7	N2	117.50(17)		C7	C8	C10	120.97(18)
C8	C7	C6	121.27(17)		C9	C8	C7	118.79(18)
C20	C19	C18	119.81(18)		C9	C8	C10	120.24(18)
C20	C19	C22	120.63(19)		C2	C3	C4	125.72(19)
C18	C19	C22	119.49(18)		C3	C2	C1	120.7(2)
C20	C21	C16	120.15(18)		N1	C1	C2	178.7(2)

Table 2.7 Torsion Angles for Rilpivirine

A	B	C	D	Angle/˚		A	B	C	D	Angle/˚
N4	C12	C13	C14	2.3(3)		C12	N2	C7	C8	-107.8(2)
N5	C16	C21	C20	-178.94(18)		C12	C13	C14	N3	-2.4(3)
N5	C16	C17	C18	179.31(17)		C17	C16	C21	C20	2.1(3)
N2	C7	C6	C5	-176.98(17)		C18	C19	C20	C21	-0.8(3)
N2	C7	C6	C11	7.2(3)		C5	C4	C9	C8	2.6(3)
N2	C7	C8	C9	178.94(18)		C5	C4	C3	C2	-10.8(3)
N2	C7	C8	C10	-1.3(3)		C22	C19	C20	C21	176.09(18)
N2	C12	C13	C14	-176.44(18)		C22	C19	C18	C17	-175.67(18)
C15	N4	C12	N2	179.76(16)		C4	C5	C6	C7	-3.0(3)
C15	N4	C12	C13	1.0(3)		C4	C5	C6	C11	172.94(19)
C15	N5	C16	C21	37.9(3)		C4	C9	C8	C7	-1.2(3)
C15	N5	C16	C17	-143.15(19)		C4	C9	C8	C10	179.1(2)
C15	N3	C14	C13	-0.9(3)		C4	C3	C2	C1	178.4(2)
C16	N5	C15	N4	-23.4(3)		C14	N3	C15	N4	4.9(3)
C16	N5	C15	N3	156.94(18)		C14	N3	C15	N5	-175.51(16)
C16	C21	C20	C19	-0.9(3)		C6	C7	C8	C9	-2.4(3)
C16	C17	C18	C19	0.0(3)		C6	C7	C8	C10	177.31(19)
C7	N2	C12	N4	-16.7(3)		C6	C5	C4	C9	-0.5(3)
C7	N2	C12	C13	162.12(18)		C6	C5	C4	C3	-178.40(19)
C21	C16	C17	C18	-1.6(3)		C9	C4	C3	C2	171.2(2)
C20	C19	C18	C17	1.3(3)		C8	C7	C6	C5	4.4(3)
C12	N4	C15	N5	175.45(16)		C8	C7	C6	C11	-171.40(19)
C12	N4	C15	N3	-4.9(3)		C3	C4	C9	C8	-179.36(19)
C12	N2	C7	C6	73.5(2)						

Table 2.8 Hydrogen Atom Coordinates (Å×104) and Isotropic Displacement Parameters (Å2×103) for Rilpivirine.

Atom	*x*	*y*	*z*	U(eq)
H5	-4099	-512	14248	20
H2	1072	-3117	17304	20
H21	-372	-2132	13924	21
H20	1268	-1780	12558	23
H17	-3375	914	12908	22
H18	-1754	1248	11537	24
H5A	3513	-3444	13976	23
H13	-1453	-2147	17929	22
H14	-3916	-999	17467	23
H9	2246	-6338	15597	26
H3	3835	-6556	14181	26
H11A	1445	-1388	15140	34
H11B	3016	-1644	14489	34
H11C	3182	-1802	15666	34
H2A	4240	-4550	12864	29
H10A	1137	-5347	17656	41
H10B	758	-6293	17035	41
H10C	-508	-5118	17028	41
H25A	4150	-1226	9961	51
H25B	4767	-2404	9551	51
H25C	6022	-1587	9735	51
H26A	5984	-1722	12453	68
H26B	4910	-821	11610	68
H26C	6794	-1223	11442	68
H24A	1936	-5345	10549	50
H24B	3259	-4649	10861	50
H24C	3452	-5162	9857	50
H23A	-589	-2459	10362	48
H23B	776	-3063	11178	48
H23C	-407	-3821	10798	48

CHAPTER 3. CELL BASED STUDIES OF RPV-NC

3.1 Introduction

To track AIE nanocrystals of RPV *in vivo*, it is essential to first assess the presence of RPV-NC *in vitro*. Macrophages have been known to be a key target of HIV as well as serve as reservoirs and vehicles for HIV dissemination[122-124]. They also play an important role in the regulation of disease function during the disease state[125, 126]. Furthermore, macrophages are known for their phagocytic ability to engulf a wide variety of materials such as foreign particles, infected T cells, virus particles and nanoparticles[127]. Interactions of nanoparticles with the macrophage have resulted in the induction of a broad range of activation proteins that can enhance phagocytosis, secretory function and cell migration, thus enhancing drug loading while facilitating drug transportation and formation of drug tissue depots[128]. Hence, an *in vitro* assessment of RPV-NC uptake in monocyte-derived macrophages (MDM) is required and was analyzed herein, using HPLC for quantitative drug assessments as well as flow cytometry to assess the integrity of RPV-NC. In addition to macrophages, CD4+ T cells also play an important role in the pathogenies of HIV infection. Apart from being the major target of HIV invasion, CD4+ T cells are also the predominant viral reservoirs[105, 106]. Hence, assessment of nanoparticle uptake in these cells is of prime importance. Similar to macrophages, RPV-NC uptake in CD4+ T cells was also assessed by HPLC and flow cytometry. Monocyte-macrophage and CD4+ T cell activities may differ in

pure versus combined cell cultures [129], thus, RPV-NC uptake in isolate or co-cultures was also studied.

Additionally, HIV utilizes macrophage bridging conduits (BC) or tunneling nanotubes (TNTs), more commonly referred to as cytoplasmic bridges, that are formed in infected macrophages to accelerate the intercellular spread of infection while being shielded from the immune system[130, 131]. Hence, the presence of RPV-NC in these BC or TNTs was observed by confocal microscopy. These studies demonstrated the presence and uptake of RPV-NC in macrophages and CD4+ T cells with fluorescence dependent on RPV concentration, indicating and confirming the integrity of RPV-NC.

3.2 Methods

3.2.1 Reagents

Heat-inactivated pooled human serum was purchased from Innovative Biologics, Herndon, VA, USA. Dulbecco's Modified Eagle Medium (DMEM) was purchased from Corning Life Sciences (Tewksbury, MA, USA). Bovine serum albumin (BSA) and Triton X-100 were purchased from Fisher Scientific (Hampton, NH). Monoclonal mouse HIV-1p24 (Clone Kal-1) and Dako EnVision+ detection system HRP labeled polymer anti-mouse antibodies were purchased from Agilent Technologies (Santa Clara, CA, USA). The primary antibodies used in thestudy were obtained from Santa Cruz Biotechnology, Inc. (Dallas, TX, USA): Rab5 (D-11) (sc-46692), Rab7 (H-50) (sc-10767), and Rab14 (sc-98610) (H-55). The Alexa Flour™ secondary antibodies were purchased from Thermo Fischer Scientific (Waltham, MA, USA): 594 goat anti-rabbit (A11037), 594 goat anti-mouse (A11005), 488 chicken anti-mouse (A21200), and 488 goat anti-rabbit (A11008).

Human peripheral blood monocytes were obtained by leukapheresis from HIV-1, 2 and hepatitis B seronegative donors and purified by countercurrent centrifugal elutriation. Monocyte-derived macrophages (MDM) were cultured in DMEM supplemented with 10% heat-inactivated pooled human serum, 10 µg/ml ciprofloxacin, 50 µg/ml gentamicin, and 1,000 U/ml equivalents of macrophage colony-stimulating factor for 7 days to promote monocyte-macrophage differentiation (MDM) [132, 133]. The following reagent was obtained through the NIH

AIDS Reagent Program, Division of AIDS, NIAID, NIH: CEM-SS cells (CD4+ T cells) from Dr. Peter L. Nara [134, 135].

3.2.2 Cellular uptake in MDM and T cells

Cell vitality studies for MDM were carried out using 3-(4,5-dimethylthiazol-2-yl)-2,5 diphenyltetrazolium bromide (MTT) [136]. RPV-NC concentrations from 12 to 200 µM were prepared and added to the cells in triplicate. After treatment for 8 hours, the analysis was carried out as described previously [116]. For T cell vitality studies, CD4+ T cells were treated with 3 to 200 µM of RPV-NC diluted in RPMI medium containing 10% FBS and 1% penicillin-streptomycin for 24 hours in a 96-well round-bottom plate. The supernatant was removed by centrifugation at 650 g for 5 min and cells were washed twice with PBS. Cells were then stained using LIVE/DEAD™ Fixable Green Dead Cell Stain Kit (Thermo Fischer Scientific, Waltham, MA, USA) according to manufacturer's protocol and fixed in 2% paraformaldehyde (PFA).

MDM and CD4+ T cell uptake of the particles was assessed by flow cytometry and UPLC-TUV. Adherent MDM were treated in biological triplicates with 100 µM RPV-NC for 8 hours and cells were collected at various time points after washing and scraping into 1 ml PBS. For uptake in lymphocytes, CD4+ T cells were allowed to attach for one hour in poly-L-lysine coated plates at 37°C [137]. Cells were then treated with appropriate concentrations of RPV-NC and collected at the aforementioned time points by washing and scraping into 1 ml PBS. Cell counting was done using an Invitrogen Countess Automated Cell Counter

(Invitrogen Corp., Carlsbad, CA, USA). Cells were pelleted by centrifugation at 650 g for 8 min at 4°C and lysed in methanol by sonication for 1 min followed by centrifugation to remove cell debris. Drug concentration in methanol extracts was analyzed UPLC-TUV as previously reported [96, 111]. For analysis by flow cytometry, MDM and CD4+ T cells were treated similarly, stained with LIVE/DEAD™ Fixable Green Dead Cell Stain Kit and fixed in 2% PFA. For co-culture experiments, additional staining was performed using mouse anti-human CD4 and CD14 antibodies according to the manufacturer's protocol.

3.2.3 Antiretroviral activities

Antiretroviral activities of RPV-NC and native RPV were evaluated by measures of HIV reverse transcriptase (RT) activity and HIV-p24 staining, as previously described,[138] with some modifications. In brief, MDM were treated with 100 μM RPV and RPV-NC for 8 hours. Treatment media was then replaced with fresh media. On days 1, 5, 10 and 15 post-treatment, MDM were challenged with HIV-1 ADA for 16 hours at a multiplicity of infection (MOI) of 0.1 infectious virions per cell. MDM were allowed to stay in culture for 10 days after infection with half media exchanges every 2 days and a full media exchange on day 8. Culture supernatants were then collected and analyzed for progeny virion production by RT activity [139]. At the same time, cells were washed with PBS and fixed in 4% PFA for 15 min for HIV-p24 staining [8]. Images were analyzed using a Nikon TE300 microscope with a 20x magnification objective.

3.2.4 Transmission electron microscopy and atomic force microscopy

For TEM tests, MDM and CD4+ T cells were incubated in 12-well plates at 10^6 cells/well for 8 hours with RPV-NC (100 μM). Cells were washed 2x with PBS and centrifuged at 650 g for 8 min at 4°C after treatment and cell pellets were suspended in a solution of 2% glutaraldehyde and 2% PFA in 0.1 M Sorenson's phosphate buffer (pH 6.2) for a minimum of 24 hours at 4°C. TEM analysis was then carried out as previously described [96, 115]. For TEM analysis, fixed samples were washed three times with PBS to clear excess fixative. During processing, samples were post-fixed in a 1% aqueous solution of osmium tetroxide for 30 min. Subsequently, samples were dehydrated in a graded ethanol series (50, 70, 90, 95, and 100%) and propylene oxide was used as a transition solvent between the ethanol and araldite resin. Samples were allowed to sit overnight in a 50:50 propylene oxide: resin solution until all the propylene oxide had evaporated. Samples were then incubated in fresh resin for 2 hours at room temperature before the final embedding. Polymerization took place at 65°C for 24 hours. The staining procedure was as follows: 10 min in 2% uranyl acetate, washed three times in distilled water, 10 min in Reynolds Lead Citrate, washed three times in distilled water. Thin sections (100 nm) made with Leica UC6 Ultracut ultramicrotome were placed on 200 mesh copper grids and examined on the Tecnai G2 Spirit TWIN (FEI, Hillsboro, OR, USA) operating at 80 kV. Images were acquired digitally with an AMT digital imaging system.

For AFM analysis, MDM were treated with RPV-NC at 100 μM for 8 hours, washed and fixed in 4% PFA. Coverslips with fixed cells were removed from wells

and mounted on a slide for AFM analysis. Images were acquired in the air using an MFP-3D™ system (Asylum Research, Santa Barbara, CA, USA) operating in tapping mode. AFM probes MSNL-F with a nominal spring constant ~0.6 N/m were used for imaging. Image processing was performed using Femtoscan software (Advanced Technologies Center, Moscow, Russia).

3.2.5 Immunocytochemistry and confocal microscopy

Subcellular immunocytochemistry localization of RPV-NC treated MDM and T cells and immunocytochemistry staining were performed as previously described with some modifications [131, 140, 141]. Briefly, after MDM were treated with RPV-NC (100 µM), cells were washed with PBS and fixed with ice-cold 4% PFA and rinsed three times with PBS. MDM were then treated with 0.5% v/v Triton-X-100 for 15 min to permeabilize the cells and again washed with PBS. A mixture of 5% w/v bovine serum albumin (BSA) in PBS and 0.1% v/v Triton-X-100 was used as a blocking solution for 1 hour, and 50 mM NH_4Cl was used as a quenching solution for 15 min and washed once with 0.1% Triton-X-100 in PBS. MDM were next treated with primary antibodies against Rab5 for early endosomes, Rab7 for late endosomes, or Rab14 for recycling endosomes. Primary antibodies were diluted 1:25 (v/v: antibody: blocking solution) and incubated overnight with shaking at 4°C as previously described [115]. MDM were then treated with secondary antibody in blocking solution (1:50) for 2 hours at room temperature. F-actin was stained using Alexa Fluor™ 488 Phalloidin (Thermo-Fischer Scientific, Waltham, MA, USA) according to the manufacturer's protocol. Nuclei were stained using NucRed™

Live 647 ReadyProbes™ Reagent (Thermo-Fischer Scientific, Waltham, MA, USA). Cells were imaged using a 63x oil objective on an LSM 710 confocal microscope (Carl Zeiss Microimaging, Inc., Dublin, CA, USA). Zeiss LSM 710 Image browser AIM software version 4.2 was used to determine the number of pixels and the mean intensity of each channel.

3.2.6 UPLC-MS/MS analysis of RPV

For analysis of RPV in plasma, 10 µL of internal standard (IS) solution (250 ng/ml indinavir and 500 ng/ml lopinavir; final concentration 25 ng/ml indinavir, 50 ng/ml lopinavir) was added to 25 µl of plasma along with 1 ml of ice-cold Optima-grade acetonitrile. Samples were then vortexed and centrifuged at 17,000 g for 10 min at 4°C. Supernatants were evaporated using a Thermo Scientific Savant Speed Vacuum (Waltham, MA, USA) and reconstituted in 100 µL 50% (v/v) optima-grade methanol in optima-grade water. Standard curves were prepared in blank rat plasma in the range of 0.2–2000 ng/ml RPV with 10 µL of IS added. For tissue analyses, 100 mg of tissue was homogenized in 4 volumes of 90% (v/v) Optima-grade methanol/water using a Qiagen Tissue Lyzer II (Valencia, CA, USA). To 100 µL of tissue homogenate, 80 µL of 100% Optima-grade methanol, 10 µL of 50% Optima-grade methanol (v/v) in MS-grade water, and 10 µL IS was added. Standard curve samples were prepared using equivalent tissue matrix dilutions, to which 80 µL of Optima-grade methanol, 10 µL of 50% Optima-grade methanol (v/v) in MS-grade water spiked with standard drug concentrations and 10 µL of IS were added. Chromatographic separation of 10 µL of plasma or tissue samples was

achieved with an ACQUITY UPLC BEH Shield RP18 column (1.7 µm, 2.1 mm x 100 mm) using a 7 min gradient of mobile phase A (7.5 mM ammonium bicarbonate in Optima-grade water adjusted to pH 7 using acetic acid) and mobile phase B (100% Optima-grade methanol) at a flow rate of 0.25 ml/min. The initial mobile phase composition of 70% B was held for 4.75 min and was increased to 95% B in 0.25 min then held constant for 0.75 min. Mobile phase B was reset to 70% in 0.25 min and the column was equilibrated for 1.0 min before the next injection. RPV was detected at a cone voltage of 92 V and collision energy of 56 V. Multiple reaction monitoring (MRM) transitions used for RPV, indinavir and lopinavir were 367.032 m/z > 127.859 m/z, 614.14 m/z > 97.023 m/z, and 629.177 m/z > 155.031 m/z, respectively. Spectra were analyzed and quantified by MassLynx software version 4.1 using the ratio of analyte peak area to IS peak area.

3.2.7 Statistics

For all studies, data were analyzed using GraphPad Prism 7.0 software (La Jolla, CA) and presented as the mean ± the standard error of the mean (SEM). Experiments were performed using a minimum of three biologically distinct replicates. Sample sizes were not based on power analyses. For comparisons of two groups, Student's *t-test* (two-tailed) was used. HIV-1 RT activity and HIV-1p24 staining were analyzed by one-way ANOVA with Bonferroni correction for multiple comparisons. For studies with multiple time points, two-way factorial ANOVA and Bonferroni's post-hoc tests for multiple comparisons were performed. Extreme

outliers beyond the 99% confidence interval of the mean and 3-fold greater than the SEM were excluded. Significant differences were determined at $P < 0.05$.

3.3 Results

3.3.1 Cell-based RPV-NC activities

To assess the cellular kinetics of RPV-NC, cytotoxicity, particle uptake and antiretroviral activities are required in HIV-1 infectible macrophages and CD4+ T cells [142-145]. MDM treated with RPV-NC demonstrated no apparent cytotoxicity at concentrations up to 200 μM over 8 hours using MTT vitality assays (**Figure 3.1 A**). To assess cell uptake, MDM were treated with 100 μM RPV-NC and at 2, 4, 6 and 8 hours, media was removed, and cells lysed for drug analysis. Cellular RPV concentrations increased over time with maximum uptake seen at 6 hours (60 μg/10^6 cells) (**Figure 3.1 B**). AFM micrographs of replicate treated MDM showed no cell surface distortions upon uptake of RPV-NC (**Figure 3.1 C**). The intracellular uptake of RPV-NC was confirmed by TEM demonstrating RPV-NC in the macrophage cytoplasm and in the membrane-bound intracellular structures (**Figure 3.1 D**). Because AIE relies on particle aggregation, we studied nanoparticle integrity in MDM by flow cytometry. Up to 98.8% of MDM demonstrated nanoparticle uptake at 8 hours (**Figure 3.1 E**), further highlighting their ability to phagocytose nanoparticles in large amounts [146, 147]. Uptake of RPV-NC by CD4+ T cells was similarly evaluated. No cytotoxicity was observed at concentrations of up to 200 μM when treated for 8 hours (**Figure 3.2 A**). Cell uptake was determined at 2, 4, 6 and 8 hours after 100 μM RPV-NC treatments. Maximum uptake of 8 μg/10^6 cells was seen at 8 hours (**Figure 3.2 B**). To assess RPV-NC integrity over time within CD4+ T cells, the cells were examined by flow

cytometry. Both the percent and median fluorescent intensity (MFI) increased with time, corresponding to the efficiency of endocytosis and RPV-NC accumulation within CD4+ T cells, respectively. The RPV-NC positive population increased from 11% at 2 hours to 30% at 24 hours along with a 10-fold increase in MFI (**Figure 3.2 C and D**). Pearson correlation between the median fluorescent intensity (MFI) and drug concentration showed an r-value of 0.8800 when cells were treated with 100 μM RPV-NC over a time course of 24 hours (**Figure 3.2 E**). Correlative studies were also performed by varying the treatment concentration with a fixed harvest after 24 hours. Results revealed that both MFI and intracellular RPV were positively correlated with treatment concentration and showed a Pearson r-value of 0.7925 (**Figure 3.2 F**). TEM images from cells treated for 24 hours with 100 μM RPV-NC depict the discernible presence of nanoparticles in T cell cytoplasm and membrane-bound intracellular structures (**Figure 3.2 G**). Thus, RPV-NC uptake kinetics in a model for CD4+ T cells can be monitored using AIE.

Monocyte-macrophage and CD4+ T cell activities may differ in pure versus combined cell cultures [129], thus, we studied RPV-NC uptake in isolate or co-culture conditions over 24 hours. CD14+ MDM demonstrated greater uptake of RPV-NC in co-culture with CD4+ T cells (**Figure 3.4 A and B**, **Figure 3.5**). In contrast, CD4+ lymphocytes exhibited less efficient endocytosis of RPV-NC in the presence of macrophages. These differences emphasize the phagocytic potential of macrophages, which readily outcompete T cells to engulf RPV-NC, whereas lymphocyte immune activation of macrophages may enhance their uptake potential [132]. RPV-NC cytoplasmic accumulation in macrophages was further

detected using flow cytometry of nanocrystal AIE as exhibited by the rightward shift in histogram peaks with varying treatment concentration (**Figure 3.4 C**). Pearson correlation analysis revealed a high positive correlation (r = 0.9810) between MFI and treatment concentration in macrophages (**Figure 3.4 D**). In contrast, CD8+ T cells and CD19+ B lymphocytes exhibited no such dose-dependent accumulation of RPV-NC (**Figure 3.7**).

3.3.2 Cellular and sub-cellular colocalizations

To track their fate once inside cells, RPV-NC sub-cellular localization in monocyte-macrophages and CD4+ T cells was studied by confocal microscopy. MDM were treated for 8 hours with 100 μM RPV-NC then immune-stained for endosomal markers that included Rab5 (early endosomes), Rab7 (late endosomes) and Rab14 (recycling endosomes). Co-localization of RPV-NC was readily seen in stained endosomal compartments (**Figure 3.8 A**) with the Rab14 endosomes indicating that RPV-NC can be recycled for release by macrophages [133, 140, 148]. Another potential means of RPV-NC dissemination during HIV-1 infection is through cytoplasmic bridges, also called tunneling nanotubes (TNTs) or bridging conduits (BC), that facilitate cell-to-cell communication and intracellular material exchange [130, 140, 149-151]. Accordingly, TNTs of RPV-NC treated, HIV-1 ADA-infected MDM were visualized by f-actin staining. **Figure 3.8 B** shows the formation of multinucleated giant cells (i) and cytoplasmic bridges (ii) with RPV-NC observed in both the infected cells and the cytoplasmic bridges (iii and iv). Because uptake in CD4+ T cells occurs primarily by endocytosis [152], the extent of uptake is

lower than in macrophages. To visualize RPV-NC taken up by T cells, CD4+ T cells treated with RPV-NC were analyzed by confocal microscopy. RPV-NC was readily seen in the T cell cytoplasm (**Figure 3.8 C**).

Once RPV-NC entry and intercellular dissemination had been studied, antiretroviral activities of RPV-NC were also determined in MDM. MDM were treated with 100 μM RPV-NC for 8 hours followed by replacement with fresh media. On days 1, 5, 7 and 10 following treatment, cells were infected with HIV-1 ADA at a MOI of 0.1. 10 days after infection, cell supernatants were analyzed for reverse transcriptase (RT) activity. Cells were stained for HIV-1 p24 in parallel. Viral suppression was observed up to day 10 (**Figure 3.9**). These results indicate that the antiretroviral efficacy of RPV-NC parallels that of native RPV.

3.4 Discussion

Uptake of RPV-NC by macrophages and CD4+ T cells was evaluated by various methods including HPLC, flow cytometry, TEM and AFM. Results confirm the presence of intact nanocrystals of RPV. Additionally, a positive correlation was observed between the MFI and drug concentrations over time. Correlative studies were also performed by varying the treatment concentration over a fixed period of time. Results revealed that both MFI and intracellular RPV were positively correlated with treatment concentration.

Studies of RPV-NC uptake in co-cultured MDMs and CD4+ T cells showed increased amounts of RPV-NC in the macrophages due to their phagocytic activity as well as due to activation in the presence of lymphocytes[132]. These results highlight the preferential sequestration of antiretroviral nanocrystals by HIV-infectable macrophages and to a lesser degree CD4+ T cells, rather than by lymphocyte subtypes that are resistant to HIV-infection. To this end, AIE characteristics of RPV-NC facilitate the quantitative assessment of drug uptake in primary cells under conditions more similar to those encountered *in vivo*.

3.5 Figures

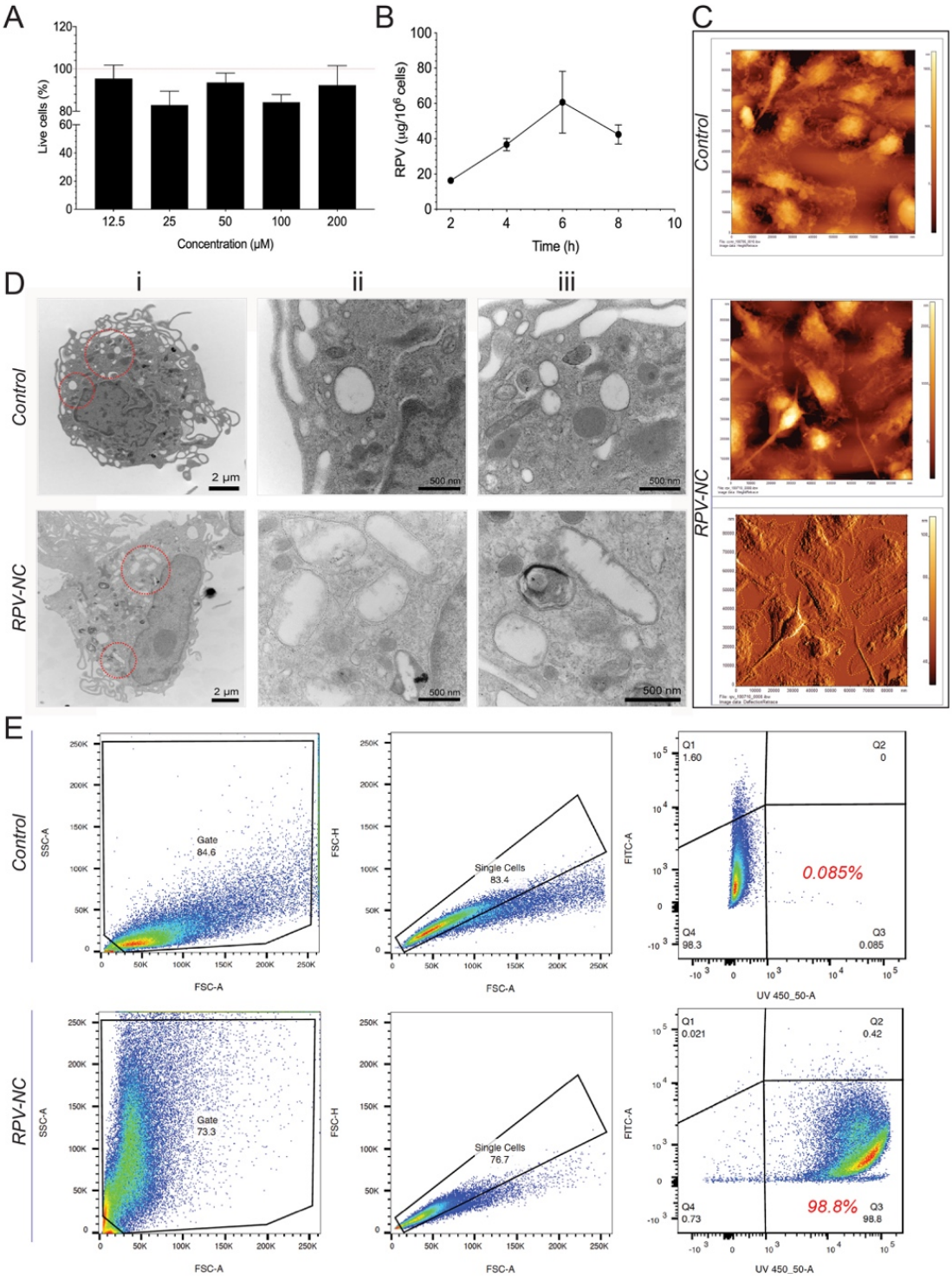
A
Live cells (%)
Concentration (μM)
B
RPV (μg/10^6 cells)
Time (h)
C
Control
RPV-NC
D
i
ii
iii
Control
RPV-NC
2 μm
500 nm
E
Control
RPV-NC
SSC-A
FSC-A
FSC-H
Gate
84.6
Gate
73.3
Single Cells
83.4
Single Cells
76.7
FITC-A
UV 450_50-A
Q1
1.60
Q2
0
Q4
98.3
Q3
0.085
0.085%
Q1
0.021
Q2
0.42
Q4
0.73
Q3
98.8
98.8%

Figure 3.1 RPV-NC macrophage targeting.

(A) MDM cell vitality was determined by the MTT assay. Data are expressed as a percent of control absorbance. **(B)** Uptake of RPV-NC in MDM upon treatment with 100 μM RPV-NC as determined by UPLC-MS. **(C)** AFM images of control and RPV-NC treated MDM. **(D)** TEM images of control and RPV-NC treated MDM showing internal morphology. The detailed evaluation of membrane-bound intracellular structures at areas of interest bordered in dotted red lines are presented in the magnified panels **(ii)** and **(iii)** and illustrate RPV-NC within membrane-bound intracellular structures. **(E)** Quantitative assessment of RPV-NC uptake by MDM via flow cytometry. MDM treated with RPV-NC (100 μM) for 8 hours were stained with a live-dead fluorophore and fixed. The percent of live MDM was determined by selecting the fluorophore dim (live) cells sub-gated from single-cells of the main forward-scatter and side-scatter density plot. The percent of RPV-NC and live double-positive cells (bottom panel) were gated based on untreated, live-stained negative controls (top panel).

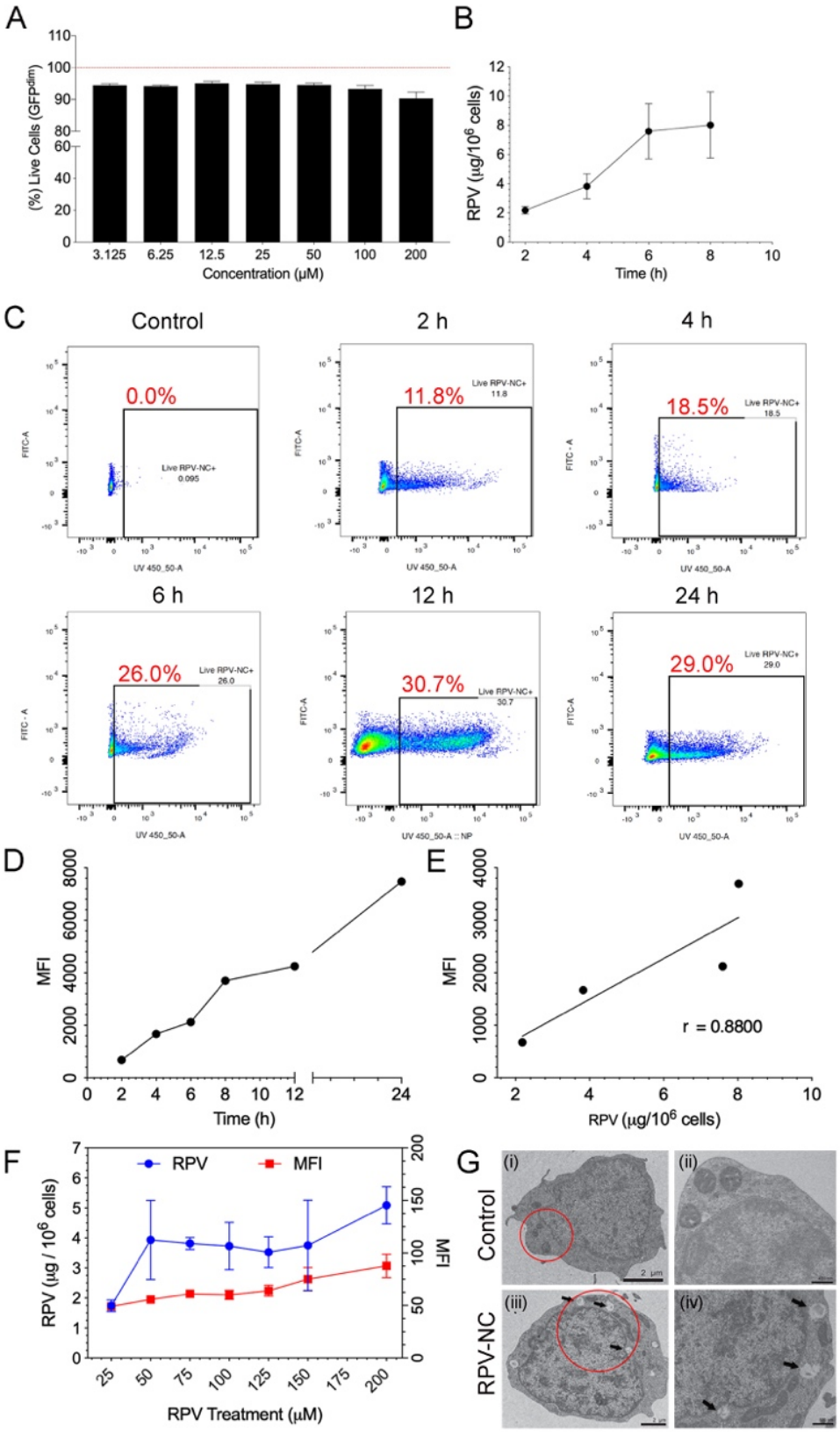
A
(%) Live Cells (GFPdim)
Concentration (μM)
3.125
6.25
12.5
25
50
100
200
B
RPV (μg/10^6 cells)
Time (h)
C
Control
2 h
4 h
6 h
12 h
24 h
0.0%
11.8%
18.5%
26.0%
30.7%
29.0%
Live RPV-NC+
FITC-A
UV 450_50-A
D
MFI
Time (h)
E
MFI
r = 0.8800
RPV (μg/10^6 cells)
F
RPV
MFI
RPV (μg / 10^6 cells)
RPV Treatment (μM)
G
Control
RPV-NC
(i)
(ii)
(iii)
(iv)

Figure 3.2 RPV-NC detection in CD4+ T cells.

(A) CD4+ T cell vitality assessed by flow cytometry. The percent live population is based on gating for GFP_{dim} cells. **(B)** Uptake of RPV-NC in CD4+ T cells upon treatment with 100 μM RPV-NC for 8 hours as determined by UPLC. **(C)** Flow cytometric quantitation of RPV-NC uptake in T cells. CD4+ T cells were treated with RPV-NC (100 μM) for 2, 4, 6, 12, or 24 hours, then stained with live-dead indicating fluorophore and fixed. Gating for double-positive live, RPV-NC containing cells was performed versus untreated control based on the gating strategy noted above (**Figure 3.1E**, full gating shown in **Figure 3.3**). **(D)** MFI for RPV-NC positive populations at each time point. **(E)** Pearson correlation between MFI and drug concentration; r = 0.8800. **(F)** MFI and RPV levels in CD4+ T cells treated with increasing concentrations of RPV-NC. **(G)** TEM images of control and RPV-NC treated CD4+ T cells showing internal morphology. The detailed evaluation of membrane-bound intracellular structures at areas of interest bordered in dotted red lines are presented in the magnified panels **(ii)** and **(iv)** and illustrate nanoparticles (indicated by arrows) within membrane-bound intracellular structures.

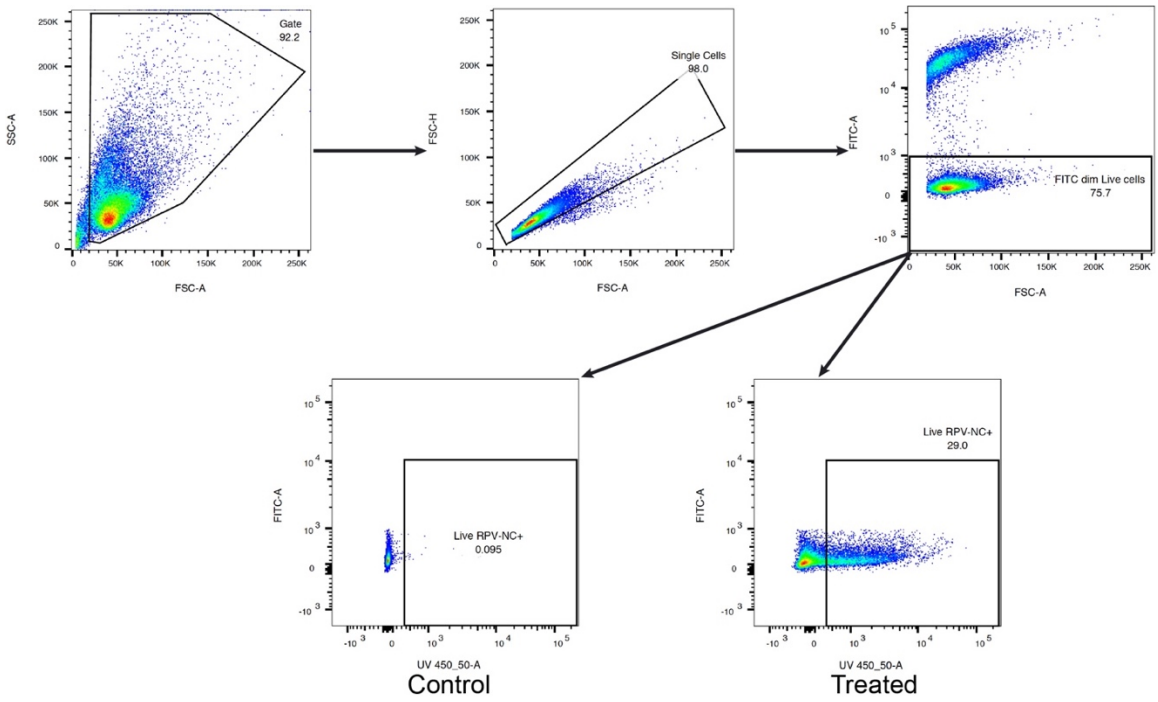

Figure 3.3 Gating strategy for RPV-NC uptake in T cells.

Single cells were sub-gated into $FITC_{bright}$ and $FITC_{dim}$. $FITC_{dim}$ cells were then gated for RPV-NC positive populations based on untreated control cells.

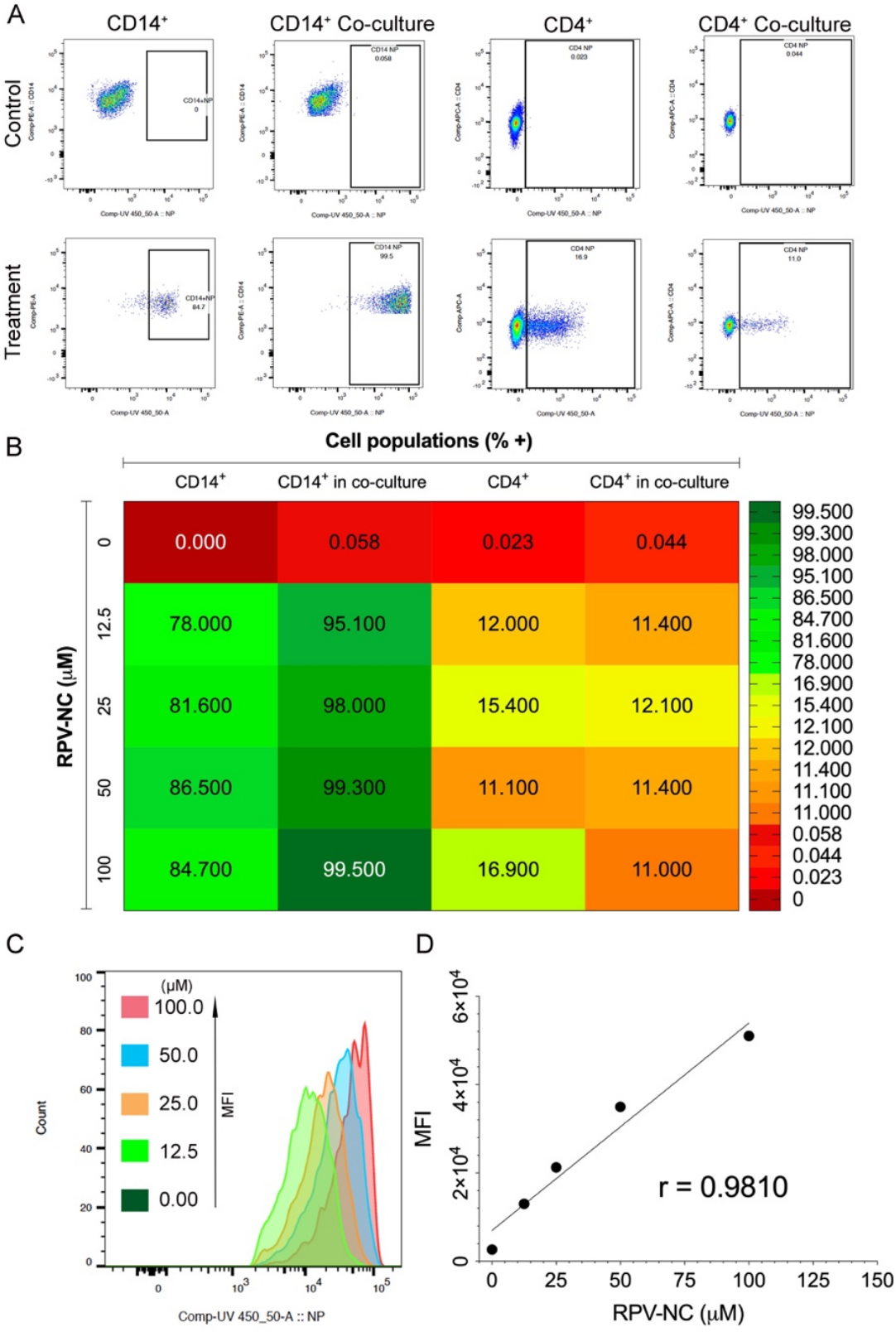
A
CD14+
CD14+ Co-culture
CD4+
CD4+ Co-culture
Control
Treatment
B
Cell populations (% +)
CD14+
CD14+ in co-culture
CD4+
CD4+ in co-culture
RPV-NC (μM)
0
12.5
25
50
100
0.000
0.058
0.023
0.044
78.000
95.100
12.000
11.400
81.600
98.000
15.400
12.100
86.500
99.300
11.100
11.400
84.700
99.500
16.900
11.000
99.500
99.300
98.000
95.100
86.500
84.700
81.600
78.000
16.900
15.400
12.100
12.000
11.400
11.100
11.000
0.058
0.044
0.023
0
C
(μM)
100.0
50.0
25.0
12.5
0.00
MFI
Count
Comp-UV 450_50-A :: NP
D
MFI
RPV-NC (μM)
r = 0.9810

Figure 3.4 RPV-NC in macrophage-T cell co-cultures.

(A) Primary MDM and PBL from human blood elutriation were treated in isolation or co-culture with RPV-NC (100 μM) for 24 hours. Treated and untreated (negative control) cells were stained with antibody cocktail against CD45 (pan-leukocyte), CD3 (T cell), CD4, CD8, and CD14 (monocyte-macrophage) epitopes. Sub-gating from parent populations is depicted in **Figure 3.5** and the percent of RPV-NC containing (bottom plots) CD14+ monocyte-macrophage and CD4+ T cell populations was determined against negative control (top plots). **(B)** The percent of each population containing RPV-NC is represented in heat map format for both CD14+ monocyte-macrophages and CD4+ T cells treated with a range of concentrations of RPV-NC (12.5-100 μM), either in isolation or co-culture. **(C)** Histogram showing the increasing MFI of RPV-NC positive monocyte-macrophage populations treated in isolation at various concentrations (12.5-100 μM). **(D)** Pearson correlation analysis comparing MFI and RPV-NC treatment concentration from **(C)** yielded an r value of 0.9810.

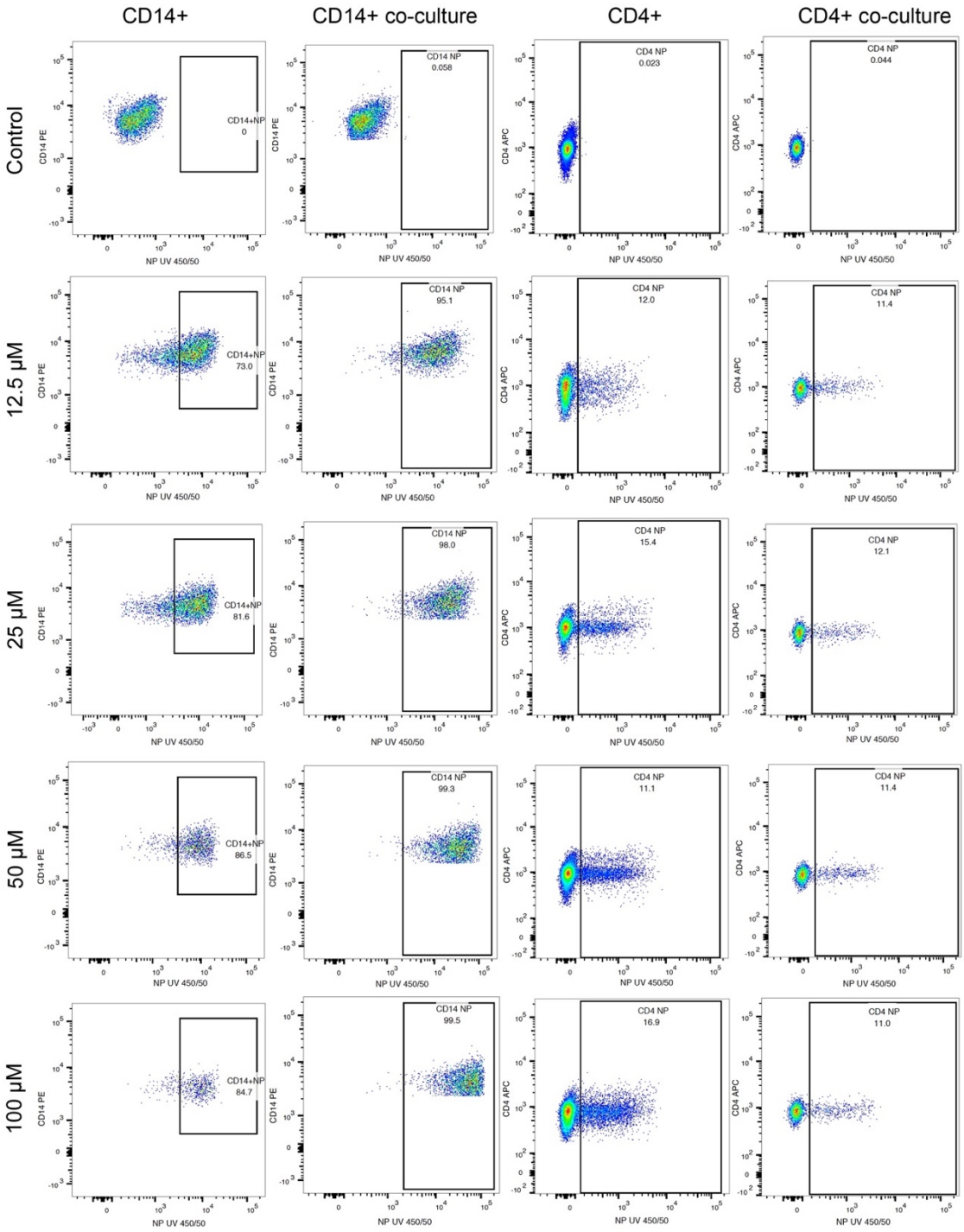

Figure 3.5 RPV-NC uptake in co-cultured macrophages and CD4+ T cells.

Flow cytometry plots of CD14+ macrophages and CD4+ T cells treated with 12.5, 25, 50 and 100 μM RPV-NC. Gates show cells positive for RPV-NC on UV 450/50.

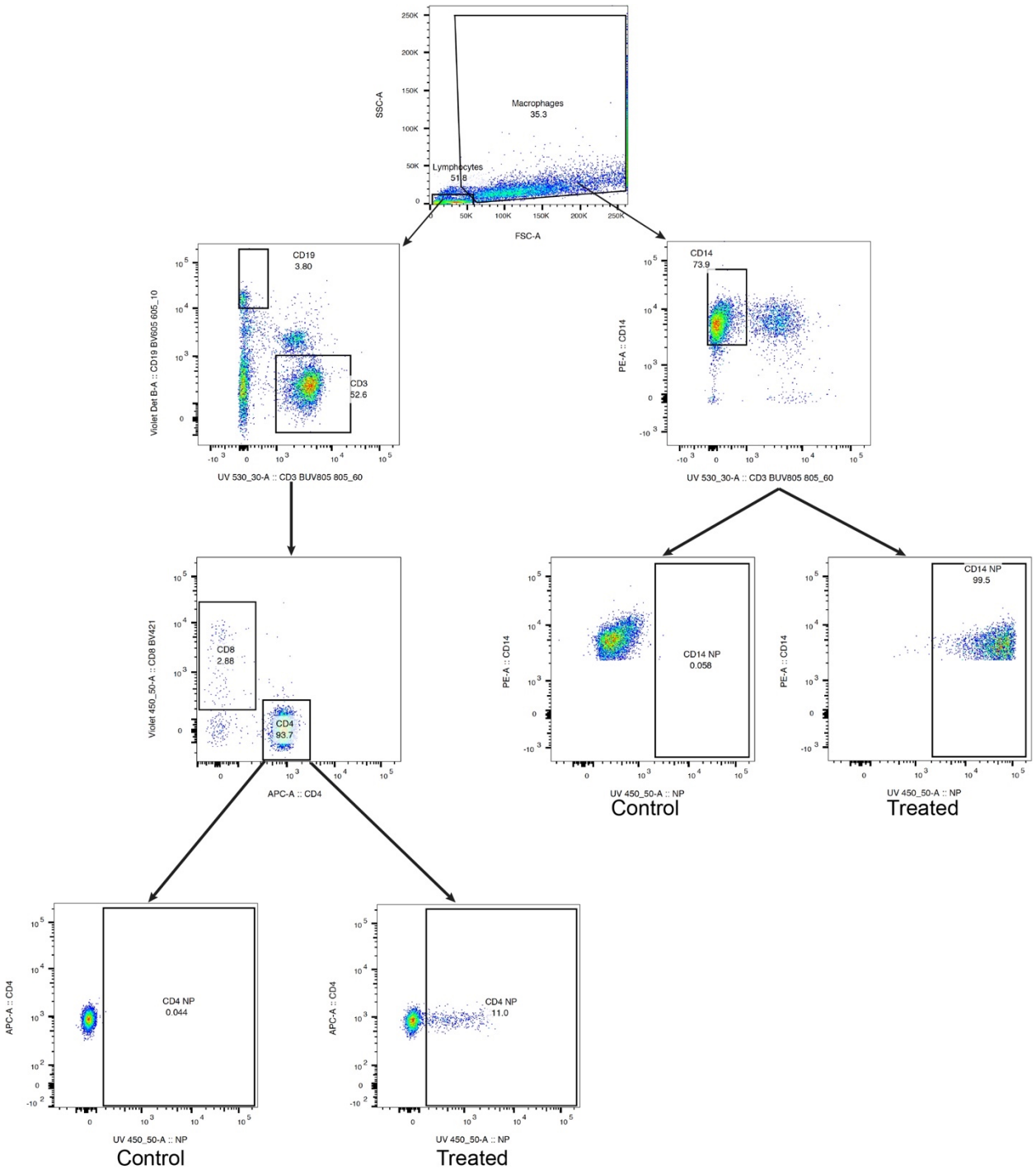
SSC-A
FSC-A
Macrophages
35.3
Lymphocytes
51.8
Violet Det B-A :: CD19 BV605 605_10
UV 530_30-A :: CD3 BUV805 805_60
CD19
3.80
CD3
52.6
PE-A :: CD14
CD14
73.9
Violet 450_50-A :: CD8 BV421
APC-A :: CD4
CD8
2.88
CD4
93.7
CD14 NP
0.058
CD14 NP
99.5
UV 450_50-A :: NP
Control
Treated
CD4 NP
0.044
CD4 NP
11.0

Figure 3.6 Gating strategy for RPV-NC uptake in co-cultured cells.

Cells were gated separately into lymphocytes and macrophages. Lymphocytes were then sub-gated into $CD19^+$ and $CD3^+$ populations. $CD3^+$ populations were then sub-gated into $CD8^+$ and CD4+ populations. Macrophages were gated into CD14+ and $CD3^+$ populations. RPV-NC positive CD4+ and CD14+ populations were then gated based on control untreated cells.

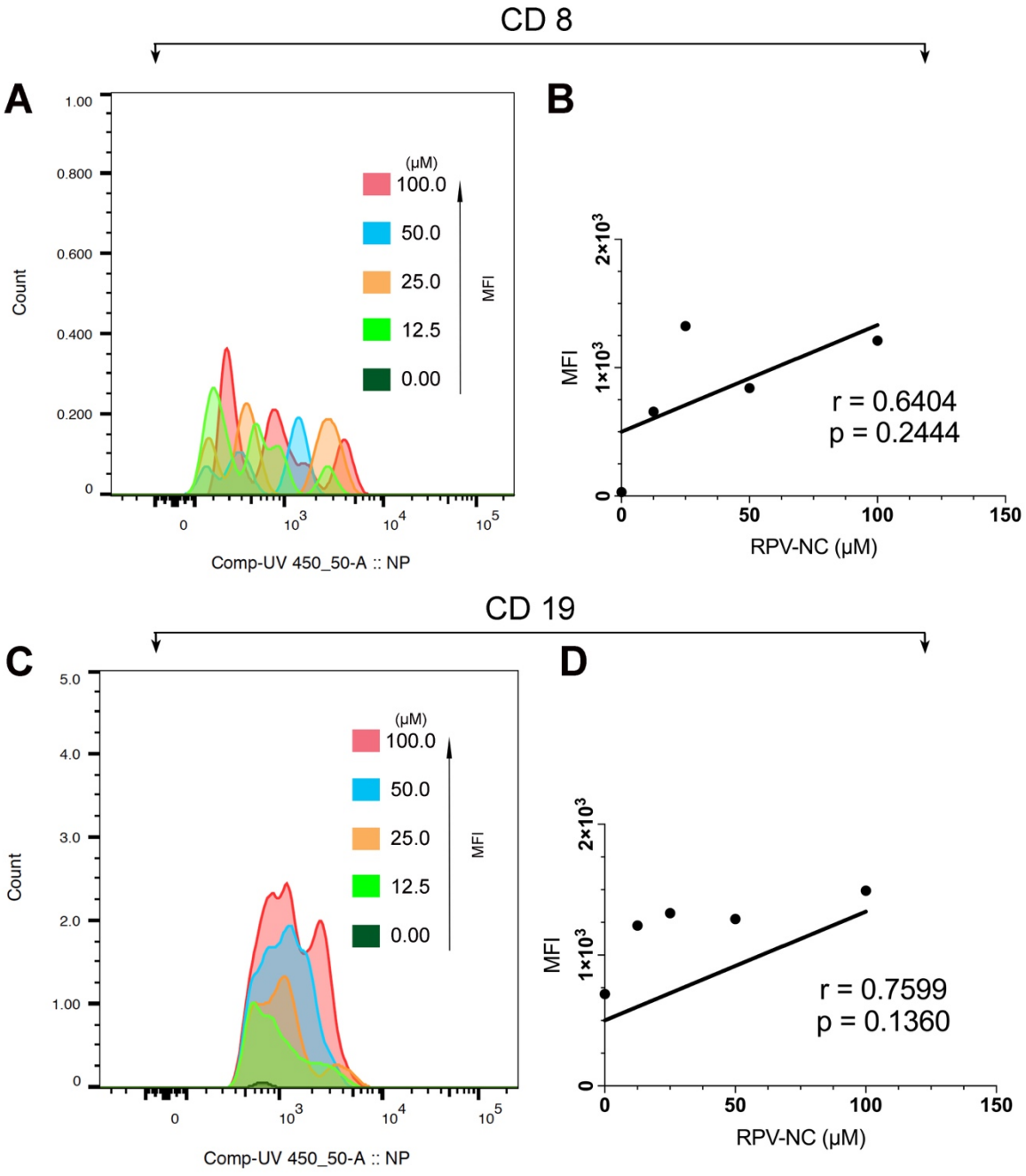
CD 8
A
B
Count
MFI
(μM)
100.0
50.0
25.0
12.5
0.00
Comp-UV 450_50-A :: NP
r = 0.6404
p = 0.2444
RPV-NC (μM)
CD 19
C
D
r = 0.7599
p = 0.1360

Figure 3.7 RPV-NC uptake by PBMC lymphocytes.

Human peripheral blood mononuclear cells (PBMC) were treated with RPV-NC at 0-100 uM drug for 24 hours then immunostained to identify HIV non-infectible CD8+ T (A-B) and CD19+ B (C-D) lymphocytes via flow cytometry. Histograms showing median fluorescent intensity (MFI) corresponding to RPV-NC intracellular accumulation among lymphocyte subtypes are plotted (A-C). Pearson correlation analyses of MFI against treatment concentration were performed (C-D) and shown by two-tailed p-value to be not significant at $\alpha = 0.05$ among each of the lymphocyte subtypes.

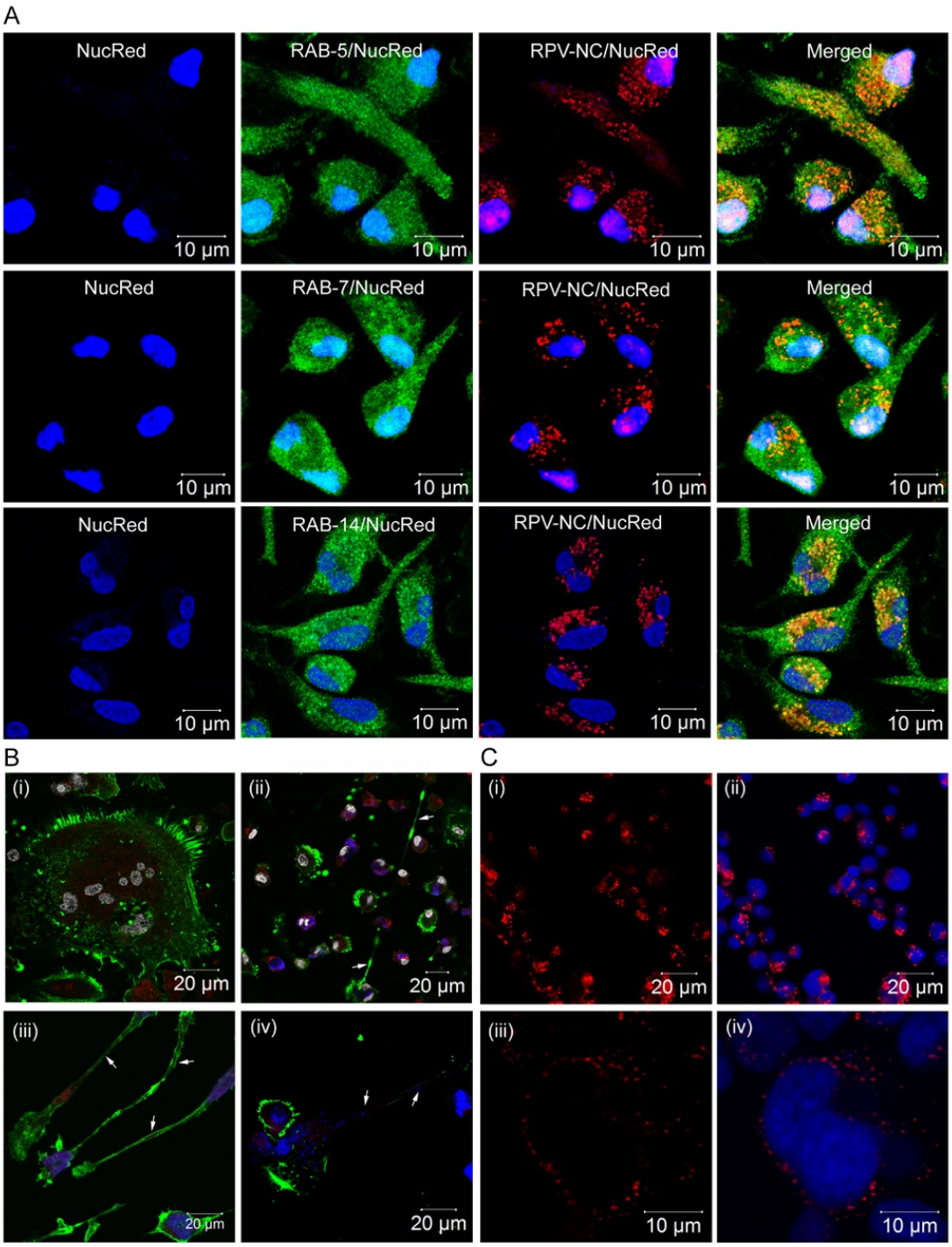
A
NucRed
RAB-5/NucRed
RPV-NC/NucRed
Merged
NucRed
RAB-7/NucRed
RPV-NC/NucRed
Merged
NucRed
RAB-14/NucRed
RPV-NC/NucRed
Merged
10 µm
B
C
(i)
(ii)
(iii)
(iv)
20 µm
10 µm

Figure 3.8 Cellular and sub-cellular RPV-NC localizations.

(A) Representative images of macrophages treated with RPV-NC (pseudo-colored red) and Alexa-Fluor 488 secondary antibody against primary Rab5, Rab7 or Rab14 antibodies (green). Yellow areas (merged images) indicate co-localization of RPV-NC with endosomal compartments. Nuclei are stained with NucRed (pseudo-colored blue). **(B)** Cellular distribution of RPV-NC (blue) in infected macrophages. Virus particles were visualized by staining with Alexa-Fluor 594 secondary antibody against p24 primary (red). Cell cytoskeleton and tunneling nanotubes were visualized by staining for F-actin (green). **(i)** Control macrophages showing giant cell formation upon infection. **(ii)** and **(iii)** Infected macrophages showing the formation of tunneling nanotubes (indicated by the white arrows) and the presence of RPV-NC in the cell cytoplasm. **(iv)** Presence of RPV-NC in the tunneling nanotubes of infected macrophages (indicated by the arrows). Nuclei are stained with NucRed (pseudo-colored white). **(C)** Presence of RPV-NC (pseudo-colored red) in CD4+ T cells. Nuclei are stained with NucRed (pseudo-colored blue).

A

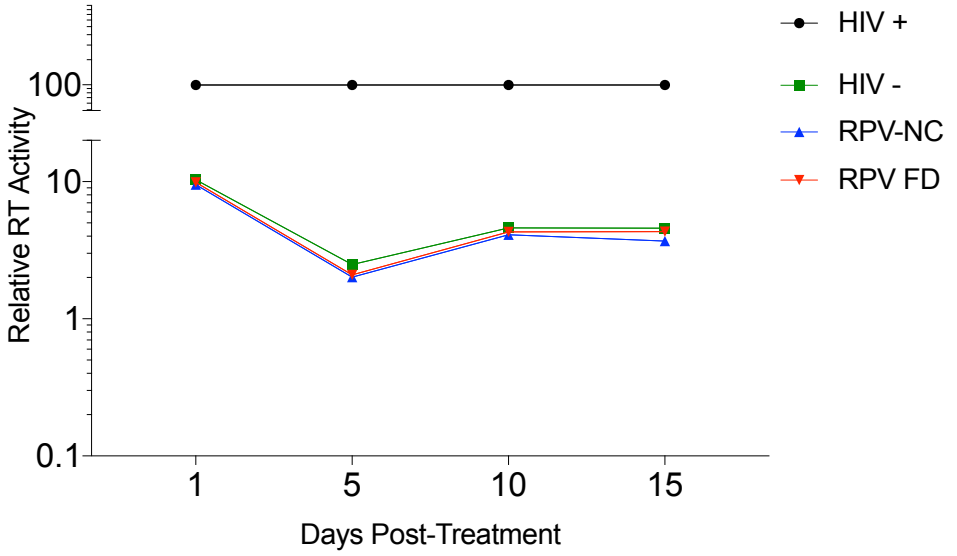
HIV +
HIV -
RPV-NC
RPV FD
Relative RT Activity
100
10
1
0.1
1
5
10
15
Days Post-Treatment

B

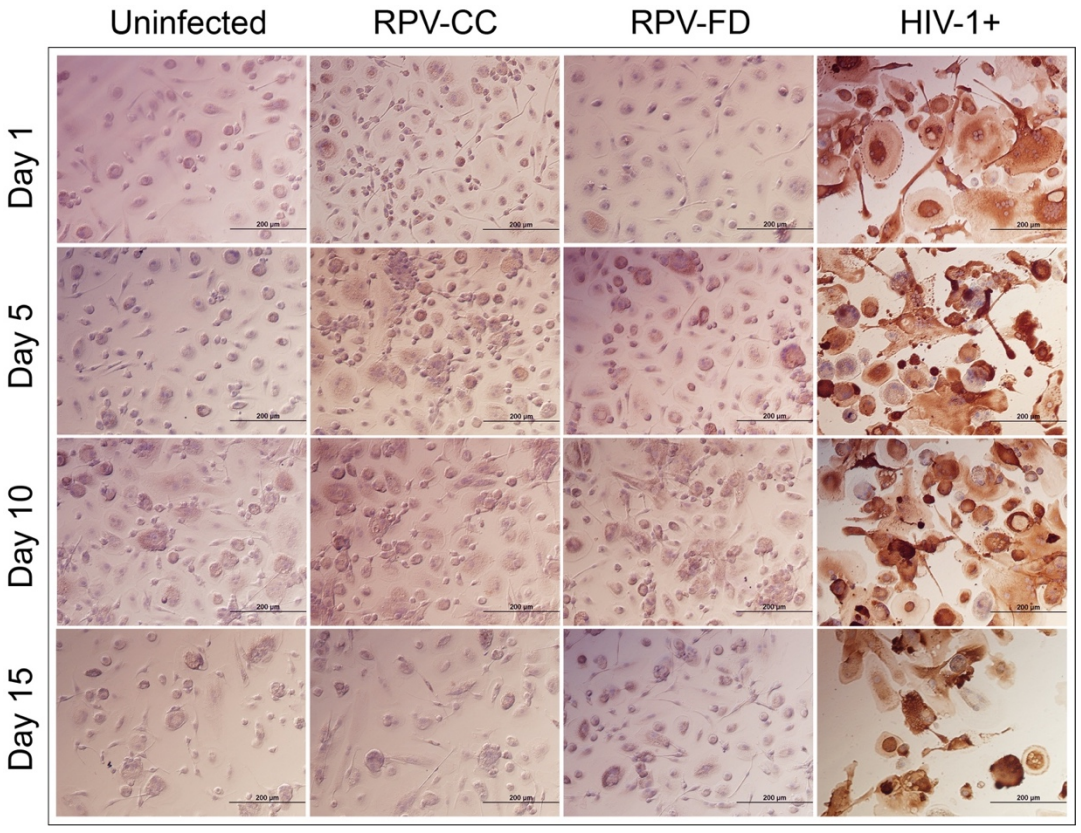
Uninfected
RPV-CC
RPV-FD
HIV-1+
Day 1
Day 5
Day 10
Day 15

Figure 3.9 Antiretroviral activity of RPV-NC in MDM.

(A) Progeny HIV virion production was determined by HIV reverse transcriptase (RT) activity using beta scintillation spectroscopy. (B) HIV p24 staining (brown) counterstained with hematoxylin (blue) (scalebar = 200 μm).

CHAPTER 4. PHARMACOKINETIC (PK) AND BIODISTRIBUTION ASSAYS

4.1 Introduction

Animal models are vital aspects of the research world and have been widely used to advance scientific findings and predict clinical outcomes. While no single animal model can completely recapitulate human disease, significant progress has been made in advancing animal models to closely mimic human systems. Animal models enable us to make important predictions about drug pharmacokinetics for possible use in humans. Key insights can be obtained on disease progression and pathogenesis, as well as drug biodistribution and pharmacokinetics. In the current study, the tissue pharmacokinetics and biodistribution of RPV-NC were evaluated in Sprague-Dawley rats as well as human peripheral blood lymphocyte (PBL)-reconstituted mice. A short 5-day PK study was carried out in Sprague-Dawley rats while a longer 10-day PK profile was studied in PBL-reconstituted mice. Animal tissues were also analyzed for the presence of intact nanoparticles by confocal microscopy.

Finally, to track nanoparticles in CD4+ T cells and monocyte-macrophages, a second murine model, the human $CD34^+$ hematopoietic stem cell (HSC)-reconstituted model, was employed to assess uptake of RPV-NC in human immune cells[153]. Single cell isolates from liver and spleen tissue were subjected to fluorescence-activated cell sorting (FACS) to detect RPV-NC CD4+ and CD14+ cell populations that are known cellular reservoirs of HIV[154]. Our data provide

evidence that AIE can be used as a platform to detect ARV delivery to cellular reservoirs of HIV.

4.2 Methods

4.2.1 Reagents

FITC mouse anti-human CD45, BUV805 mouse anti-human CD3, APC mouse anti-human CD4, PE mouse anti-human CD14, BV605 mouse anti-human CD19 and BV421 mouse anti-human CD8 were purchased from BD Biosciences (San Jose, CA, USA). Methanol, hexane and optima-grade solvents were purchased from Thermo Fischer Scientific. Bovine serum albumin (BSA), Gibco RPMI Medium 1640 and HyClone™ Penicillin Streptomycin 100x solution were purchased from Thermo Fischer Scientific. Fetal bovine serum (FBS) was purchased from Atlanta Biologicals (Flowery Branch, GA, USA).

4.2.2 In vivo pharmacokinetic (PK) and biodistribution assays

PK and biodistribution studies for RPV-NC were carried out in rats and mice. For the first study, Sprague-Dawley rats (180-200 g, Jackson Labs, Bar Harbor, ME, USA) were injected IV with 45 mg/kg RPV-NC. On days 1 and 2 post-injection blood was collected. Plasma was subsequently isolated by centrifugation at 2000 g for 5 min for drug quantification tests by UPLC-MS/MS. Five days after injection the animals were sacrificed, and tissues (liver, spleen and lymph node) were stored. In a replicate study, male 6- to 8-week-old NOD/SCID/IL2R$\gamma c^{-/-}$ (NSG) mice (Jackson Labs, Bar Harbor, ME, USA) were injected intraperitoneally with $25x10^6$ human peripheral blood lymphocytes (PBL). These cells were obtained by leukapheresis and centrifugal elutriation and used to reconstitute the NSG mice.

Twelve days after reconstitution, mice were injected intravenously with 45 mg/kg RPV-NC. After 10 days, the animals were sacrificed and tissues were collected for drug quantification by LC-MS/MS [96, 111]. For confocal analysis, 5 μm sections of paraffin-embedded tissue were fixed on glass slides and stained with appropriate antibodies. For rats, spleen tissue sections were probed with rabbit anti-rat polyclonal antibody to ionized calcium-binding adaptor molecule-1 (Iba-1) (1:500, Wako Chemicals, Richmond, VA, USA) to detect macrophages [115]. Primary antibody was detected with anti-rabbit secondary antibody conjugated to Alexa Fluor 488 (Thermo-Fischer Scientific, Waltham, MA, USA). For PBL mice, spleen and lymph node tissue sections were stained with CD4 Monoclonal Antibody (OKT4 (OKT-4)), Alexa Fluor 488. NucRed™ Live 647 ReadyProbes™ Reagent (Thermo-Fischer Scientific, Waltham, MA, USA) was used as a nuclear stain.

4.2.3 Toxicological assessments

In-vivo toxicity of RPV-NC was assessed by serum chemistry and histological examination. For histological examination, 5 μm sections of paraffin-embedded tissues were affixed to glass slides and stained with hematoxylin and eosin. Images were captured with a 20x objective using a Nuance EX multispectral imaging system affixed to a Nikon Eclipse E800 microscope (Nikon Instruments, Melville, NY, USA). Histopathological assessment was conducted in accordance with the guidelines of the Society of Toxicologic Pathology. For serum chemistry analysis, rat blood samples were collected before and five days after RPV-NC administration. Albumin (ALB), alkaline phosphatase (ALP), total bilirubin (TBIL),

blood urea nitrogen (BUN), total protein (TP) and creatinine (CRE) were quantitated using a VetScan comprehensive diagnostic profile disc and a VetScan VS-2 instrument (Abaxis Veterinary Diagnostics, Union City, CA, USA).

4.2.4 Nanoparticle tracking in humanized mice

Nanoparticle tracking in CD4+ T cells and macrophages was assessed in humanized mice. NSG mice were reconstituted at birth with $CD34^+$ HSC isolated from umbilical cord blood [155]. Reconstituted mice, six-to-eight weeks old, were injected IV with 45 mg/kg of RPV-NC. At 24 hours following particle injection, mice were sacrificed, and the liver and the spleen were collected. Liver and spleen tissue were passed through a 70 µm cell strainer to obtain single cell suspensions. For flow cytometry analysis, cell suspensions were stained with antibodies to human CD45, CD14, CD4, CD8 and CD3 as per the manufacturer's protocol and fixed in 2% PFA. For drug quantification, single cell suspensions from the liver and spleen tissue were stained with antibodies to human CD45, CD3, CD4 and CD14 antibodies and subjected to FACS on BD FACS Aria II (BD Biosciences, San Jose, CA, USA). Sorted cells were pelleted by centrifugation at 700 g for 5 min at 4°C and analyzed by UPLC-MS/MS as described below.

4.2.5 UPLC-MS/MS analysis of RPV

For analysis of RPV in plasma, 10 µL of internal standard (IS) solution (250 ng/ml indinavir and 500 ng/ml lopinavir; final concentration 25 ng/ml indinavir, 50 ng/ml lopinavir) was added to 25 µl of plasma along with 1 ml of ice-cold Optima-

grade acetonitrile. Samples were then vortexed and centrifuged at 17,000 g for 10 min at 4°C. Supernatants were evaporated using a Thermo Scientific Savant Speed Vacuum (Waltham, MA, USA) and reconstituted in 100 µL 50% (v/v) optima-grade methanol in optima-grade water. Standard curves were prepared in blank rat plasma in the range of 0.2–2000 ng/ml RPV with 10 µL of IS added. For tissue analyses, 100 mg of tissue was homogenized in 4 volumes of 90% (v/v) Optima-grade methanol/water using a Qiagen Tissue Lyzer II (Valencia, CA, USA). To 100 µL of tissue homogenate, 80 µL of 100% Optima-grade methanol, 10 µL of 50% Optima-grade methanol (v/v) in MS-grade water, and 10 µL IS was added. Standard curve samples were prepared using equivalent tissue matrix dilutions, to which 80 µL of Optima-grade methanol, 10 µL of 50% Optima-grade methanol (v/v) in MS-grade water spiked with standard drug concentrations and 10 µL of IS were added. Chromatographic separation of 10 µL of plasma or tissue samples was achieved with an ACQUITY UPLC BEH Shield RP18 column (1.7 µm, 2.1 mm x 100 mm) using a 7 min gradient of mobile phase A (7.5 mM ammonium bicarbonate in Optima-grade water adjusted to pH 7 using acetic acid) and mobile phase B (100% Optima-grade methanol) at a flow rate of 0.25 ml/min. The initial mobile phase composition of 70% B was held for 4.75 min and was increased to 95% B in 0.25 min then held constant for 0.75 min. Mobile phase B was reset to 70% in 0.25 min and the column was equilibrated for 1.0 min before the next injection. RPV was detected at a cone voltage of 92 V and collision energy of 56 V. Multiple reaction monitoring (MRM) transitions used for RPV, indinavir and lopinavir were 367.032 m/z > 127.859 m/z, 614.14 m/z > 97.023 m/z, and 629.177

m/z > 155.031 m/z, respectively. Spectra were analyzed and quantified by MassLynx software version 4.1 using the ratio of analyte peak area to IS peak area.

4.2.6 Statistical analyses

For all studies, data were analyzed using GraphPad Prism 7.0 software (La Jolla, CA) and presented as the mean ± the standard error of the mean (SEM). Sample sizes were not based on power analyses. For comparisons of two groups, Student's t-test (two-tailed) was used. Tissue drug levels and T cell populations were analyzed by one-way ANOVA with Bonferroni correction for multiple comparisons. For studies with multiple time points, two-way factorial ANOVA and Bonferroni's post-hoc tests for multiple comparisons were performed. Animal studies included a minimum of six animals per group unless otherwise noted. Extreme outliers beyond the 99% confidence interval of the mean and 3-fold greater than the SEM were excluded. Significant differences were determined at $P < 0.05$.

4.2.7 Study approval

All experimental protocols involving the use of laboratory animals were approved by the UNMC Institutional Animal Care and Use Committee (IACUC) ensuring the ethical care and use of laboratory animals in experimental research. All animal studies were performed in compliance with UNMC institutional policies and NIH guidelines for laboratory animal housing and care. Human blood cells

were isolated by leukapheresis from HIV-1/2 and hepatitis seronegative donors and were deemed exempt from approval by the Institutional Review Board (IRB) of UNMC. Human $CD34^{+}$ hematopoietic stem cells were isolated from umbilical cord blood and are exempt from UNMC IRB approval.

4.3 Results

4.3.1 Pharmacokinetics (PK) and biodistribution

To correlate RPV-NC *in vitro* cellular uptake with tissue and cellular uptake *in vivo*, biodistribution and PK profiles of RPV-NC were assessed in rats and humanized mice. **Figure 4.1 A** shows a schematic outlining the time course of the studies in the indicated animal models. A short-term biodistribution and PK analysis was carried out in Sprague-Dawley rats injected intravenously (IV) with 45 mg/kg RPV equivalent of RPV-NC. On days 1, 2 and 5 post-injection, blood samples were collected, and plasma was analyzed by UPLC-MS/MS for drug quantification. Animal tissues were collected on day 5 post-injection and the drug was quantified by UPLC-MS/MS. **Figure 4.1 B** shows plasma drug levels over time as well as day 5 liver, spleen and lymph node drug levels. As shown in **Figure 4.1 B (i)**, plasma drug levels decreased from 134.5 ± 15.3 ng/ml on day 1 to 1.5 ± 0.2 ng/ml on day 5. In tissues, drug levels were highest in the liver (3540 ng/g of tissue), followed by the spleen (94.5 ng/g of tissue) and the lymph nodes (9.5 ng/g of tissue) in **Figure 4.1 B (ii)**. The rapid decline of plasma drug levels and increased accumulation in the tissues indicates that RPV-NC can form tissue depots. Similar results were seen with a polymeric nanoformulation of RPV where drug levels were found to be highest in the liver, spleen and lymph node tissues[116].

Toxicological assessments of liver and spleen tissues from rats treated with RPV-NC showed no histological abnormalities when compared to tissues from

untreated controls. Also, no biochemical or hematological effects of RPV-NC were seen in treated animals (**Figure 4.2**).

To track RPV-NC biodistribution in human immune cells, we adoptively transferred human peripheral blood lymphocytes (PBL) into NSG mice and dosed animals with 45 mg/kg drug. Tissues were collected on day 10 post-injection and RPV concentration was determined. Analysis of RPV drug levels in excised tissue showed the highest drug levels in the liver as seen in **Figure 4.1 B(iii)**. Having observed measurable quantities of RPV in tissues, we searched for intact nanoparticles displaying AIE in HIV-1 infectible cells. Confocal imaging of rat spleens revealed discernable overlap between UV-excitable RPV-NC and Iba-1^{+} rat macrophages (**Figure 4.1 C**). This finding extended to human CD4+ leukocytes in PBL-reconstituted mice (**Figure 4.1 D, E and F**). A high percentage of human CD4+ splenocytes exhibited RPV-NC-associated fluorescence (**Figure 4.1 D**), whereas this effect was more modest in lymph nodes (**Figure 4.1 E and F**). Together, these findings manifest that IV administration of RPV-NC travels via blood to reticuloendothelial organs (i.e., liver, spleen, and lymph nodes), where they are encountered and engulfed by various immunocytes. In contrast, IM administration of RPV shows a very different pharmacokinetic profile according to prior works involving a polymeric nanoformulation of RPV[111].

4.3.2 Cellular tracking of RPV-NC in humanized mice

To track nanoparticles in CD4+ T cells and monocyte-macrophages, a second murine model was employed to assess the uptake of RPV-NC in human

immune cells. NSG mice were reconstituted at birth with human CD34+ hematopoietic stem cells (HSC). Importantly, the reconstituted mice (humanized mice) show quiescent lymphocyte profiles and as such reflect what would occur in a HIV-1 challenged human host [155]. These humanized mice were injected with 45 mg/kg RPV equivalent of RPV-NC, and after 24 hours, the liver and spleen were collected. Single cell suspensions of these tissues were prepared and analyzed *ex vivo* by flow cytometry for nanoparticle distribution in different immune subsets. **Figure 4.3 A** shows representative flow cytometry plots of nanoparticle positive CD4+ T cells and CD14+ macrophages from treated mice. The detailed gating strategy for different immune subsets is provided in **Figure 4.4**. Human CD4+ and CD14+ populations were quantified as percent nanoparticle positive cells for each animal. From the same experimental mice, cellular suspensions from the liver and spleen were subjected to fluorescence-activated cell sorting (FACS) to sort CD4+ T cells and CD14+ monocyte-macrophages. These isolated cell populations were then analyzed by UPLC-MS/MS quantification of RPV. **Figure 4.3 B** shows liver CD4+ T cell and CD14+ macrophage percent populations positive for RPV-NC. RPV levels of about 179 ng/10^6 cells and 368 ng/10^6 cells were observed in the CD4+ T cells and monocyte-macrophages, respectively, as shown in **Figure 4.3 C**. Pearson correlations between RPV levels and percent positive CD4+ T cell or CD14+ macrophage populations provided r values of 0.81 and 0.94, respectively (**Figure 4.3 D** & **E**). Similarly, **Figure 4.3 F** shows percent CD4+ T cell and monocyte-macrophage populations positive for RPV-NC where a significantly higher particle uptake was observed in macrophages. RPV levels of about 22.6

ng/10^6 cells and 62.6 ng/10^6 cells were observed in splenic CD4+ T cells and CD14+ macrophages, respectively, as shown in **Figure 4.3 G**. Pearson correlation analysis for RPV concentration and percent cells positive for RPV-NC provided an r-value of 0.72 for the CD4+ T cells and 0.99 for the monocyte-macrophages as shown in **Figure 4.3 H and I**. Hence, the presence of RPV-NC in human monocyte-macrophages and T cells was observed by flow cytometry and substantiated with RPV drug levels from UPLC-MS/MS. The correlation values obtained confirm the presence of RPV-NC in the form of intact nanoparticles in immune cell subsets. These data, taken together, confirm that the AIE property of RPV can be used to track the presence and integrity of RPV-NC in immune cell populations.

4.4 Discussion

PK studies in rats and PBL-reconstituted mice showed detectable drug levels in tissues. Following tissue drug quantification tests, we analyzed the major tissue reservoirs of HIV: liver, spleen and lymph node ftor presence of intact nanocrystals of RPV. Confocal analysis of rat liver tissue showed apparent co-localization of RPV-NC in activated macrophages. Similar results were seen in human CD4+ leucocytes in spleen and lymph node tissues of PBL-reconstituted mice. Together, these findings manifest that IV administration of RPV-NC travels via blood to reticuloendothelial organs (i.e., liver, spleen, and lymph nodes), where they are encountered and engulfed by various immunocytes.

Furthermore, to track RPV-NC distribution in cell subpopulations, HSC-reconstituted mice, also known as, humanized mice, were used. Following treatment for 24 hours, liver and spleen tissue were collected. Single cell suspensions of these tissues were subjected to flow cytometry, FACS and UPLC-MS/MS. Presence of RPV-NC in human monocyte-macrophages and T cells was observed by flow cytometry and substantiated with RPV drug levels from UPLC-MS/MS. The correlation values obtained confirm the presence of RPV-NC in the form of intact nanoparticles in immune cell subsets. Taken together, these results posit that the AIE property of RPV can be used to track the presence and integrity of RPV-NC in immune cell populations, enabling effective and targeted delivery of ARVs to cellular viral reservoirs.

4.5 Figures

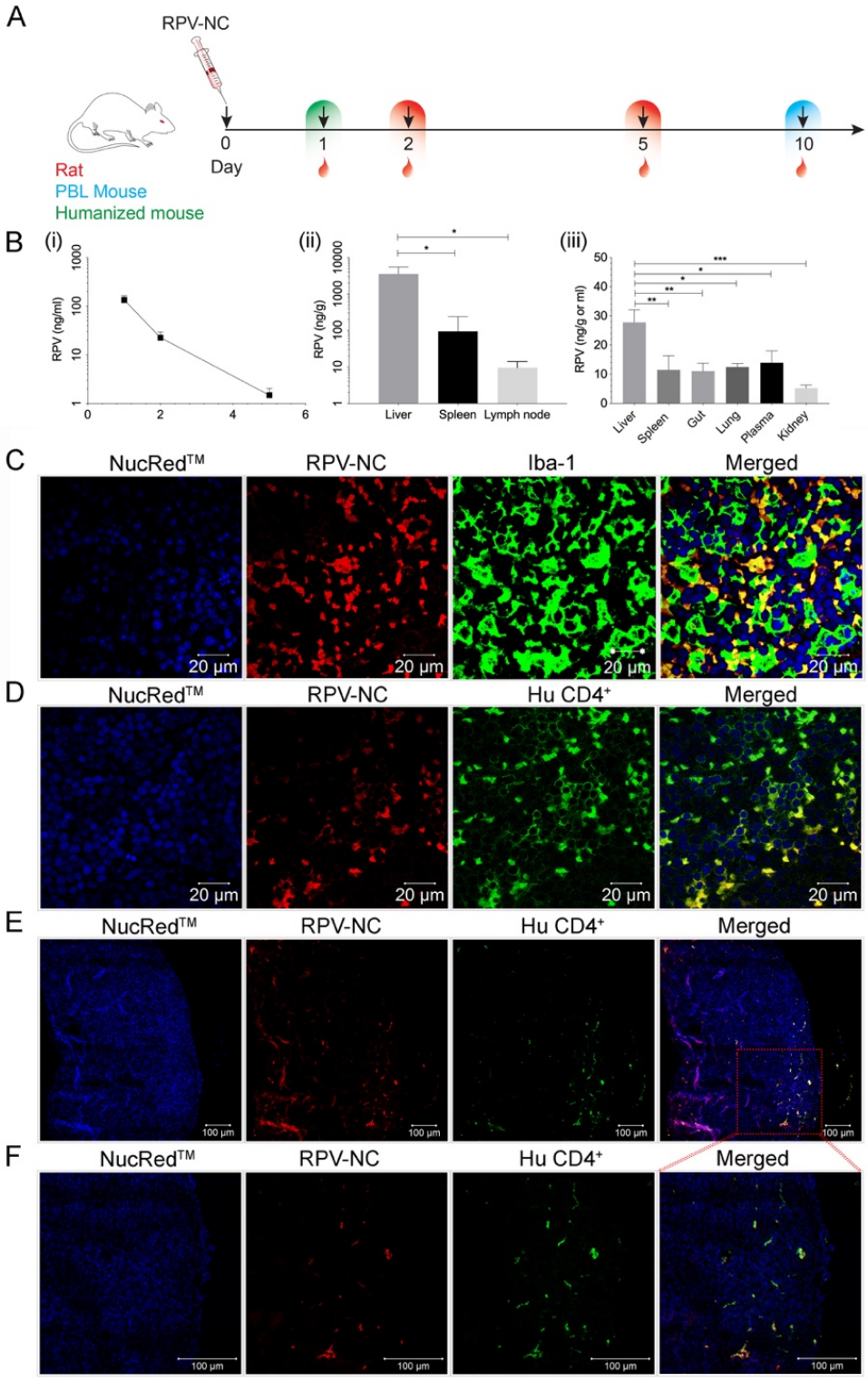
A
RPV-NC
0
1
2
5
10
Day
Rat
PBL Mouse
Humanized mouse
B
(i)
RPV (ng/ml)
(ii)
RPV (ng/g)
Liver
Spleen
Lymph node
(iii)
RPV (ng/g or ml)
Liver
Spleen
Gut
Lung
Plasma
Kidney
C
NucRed™
RPV-NC
Iba-1
Merged
20 μm
D
NucRed™
RPV-NC
Hu CD4+
Merged
20 μm
E
NucRed™
RPV-NC
Hu CD4+
Merged
100 μm
F
NucRed™
RPV-NC
Hu CD4+
Merged
100 μm

Figure 4.1 PK and RPV tissue-cell biodistribution.

(A) Schematic representation of the *in-vivo* studies of RPV-NC. **(B)** RPV concentrations from **(i)** rat plasma at 1, 2- and 5-days post-injection **(ii)** rat liver, spleen and lymph node tissue on day 5 post-injection **(iii)** PBL mouse tissue on day 10 post-injection. Statistical differences were determined using two-way ANOVA among groups; Bonferroni's post-hoc test was used for multiple comparisons. *$p < 0.05$; **$p < 0.01$; ***$p < 0.001$. **(C)** Representative images of rat spleen tissue sections stained with Iba-1 for activated macrophages (green). Yellow areas indicate co-localization of RPV-NC (pseudo-colored red) in rat splenic macrophages. Representative images of PBL mouse **(D)** spleen and **(E)** lymph node tissue sections, stained with anti-human CD4+ antibody (green). Yellow areas indicate co-localization of RPV-NC (pseudo-colored red) in human CD4+ cells. **(F)** Magnification of the areas of co-localization from (E). Nuclei are stained with NucRed (pseudo-colored blue).

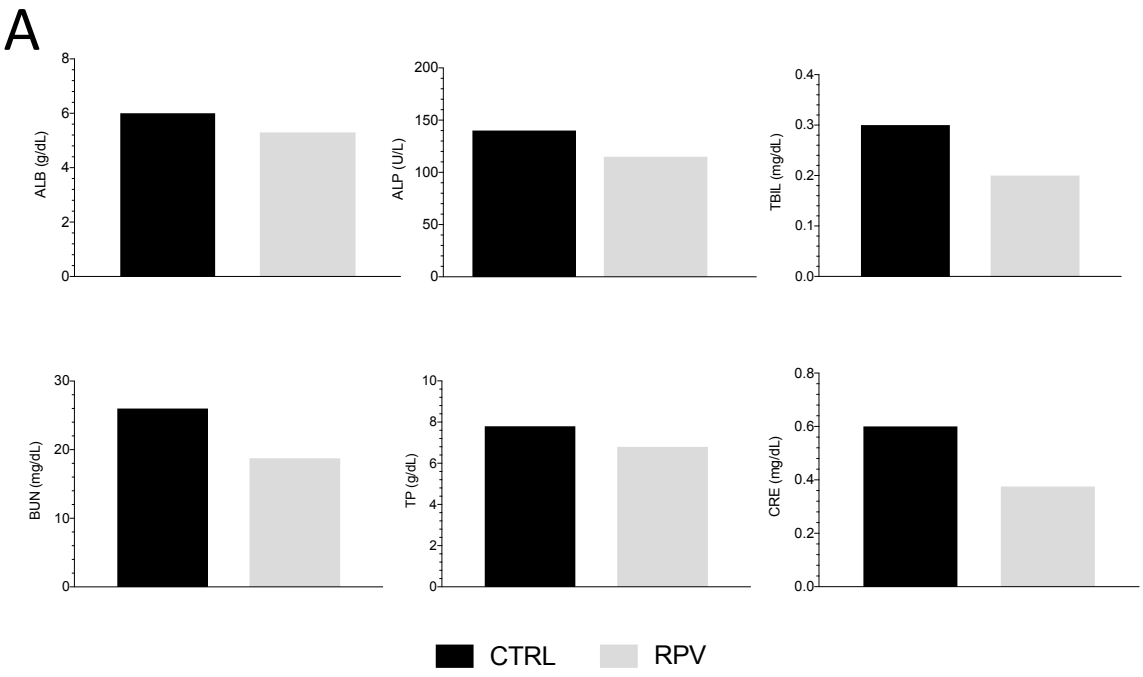
A
ALB (g/dL)
ALP (U/L)
TBIL (mg/dL)
BUN (mg/dL)
TP (g/dL)
CRE (mg/dL)
CTRL
RPV

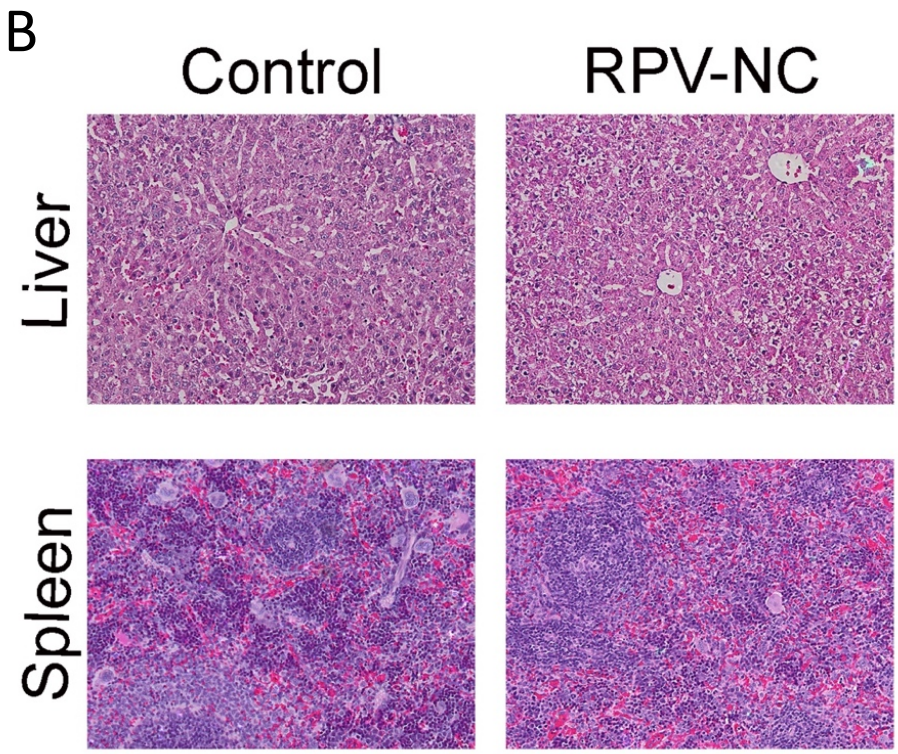
B
Control
RPV-NC
Liver
Spleen

Figure 4.2 Evaluation of RPV-NC toxicity.

(A) Hepatic, renal and pancreatic functions were analyzed in rats 5 days post-injection of RPV-NC administered IV at 45 mg/kg (ALB: Albumin, ALP: Alkaline phosphatase, TBIL: Total bilirubin, BUN: Blood urea nitrogen, TP: Total protein, CRE: creatinine). (B) Hematoxylin and eosin staining of rat tissues. Normal tissue histology was recorded in tissues in all animal groups. Images were captured with a 20x magnification objective.

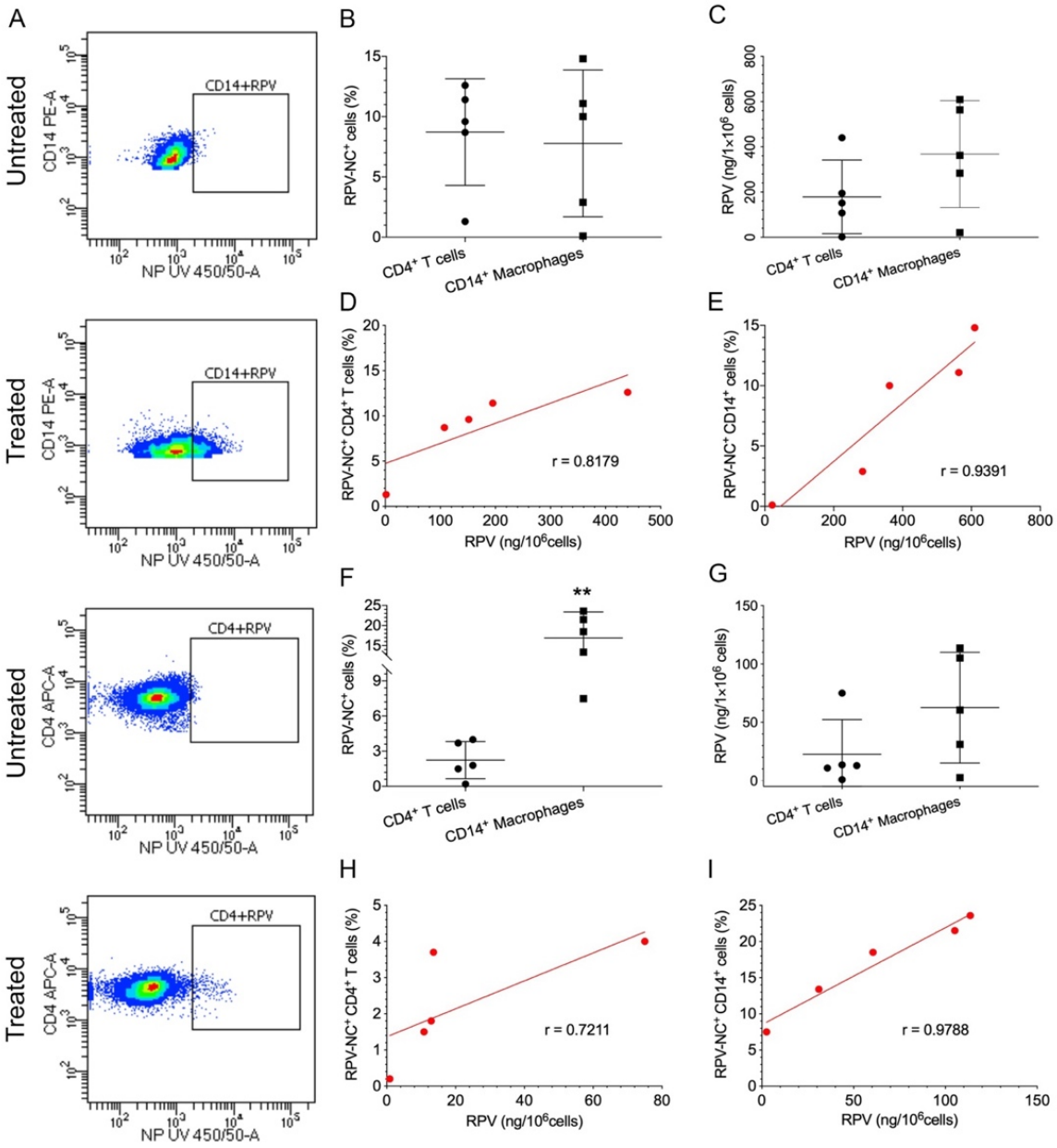
A
Untreated
CD14+RPV
CD14 PE-A
NP UV 450/50-A
B
RPV-NC+ cells (%)
CD4+ T cells
CD14+ Macrophages
C
RPV (ng/1x10^6 cells)
CD4+ T cells
CD14+ Macrophages
Treated
CD14+RPV
CD14 PE-A
NP UV 450/50-A
D
RPV-NC+ CD4+ T cells (%)
r = 0.8179
RPV (ng/10^6cells)
E
RPV-NC+ CD14+ cells (%)
r = 0.9391
RPV (ng/10^6cells)
Untreated
CD4+RPV
CD4 APC-A
NP UV 450/50-A
F
**
RPV-NC+ cells (%)
CD4+ T cells
CD14+ Macrophages
G
RPV (ng/1x10^6 cells)
CD4+ T cells
CD14+ Macrophages
Treated
CD4+RPV
CD4 APC-A
NP UV 450/50-A
H
RPV-NC+ CD4+ T cells (%)
r = 0.7211
RPV (ng/10^6cells)
I
RPV-NC+ CD14+ cells (%)
r = 0.9788
RPV (ng/10^6cells)

Figure 4.3 Nanoparticle tracking and quantification in humanized mice.

(A) Representative flow cytometry plots showing RPV-NC positive populations in spleen CD4+ T cells and CD14+ macrophages based on gating relative to splenocytes and hepatocytes from untreated control mice (see **Figure 4.4** for full gating description). **(B)** Percent populations positive for RPV-NC from the liver. **(C)** RPV concentrations in hepatic T cells and macrophages. Pearson correlation between RPV-NC percent positive population and RPV drug levels in liver **(D)** T cells; r = 0.81 and **(E)** macrophages; r = 0.93 **(F)** Percent populations positive for RPV-NC from the spleen. **(G)** RPV concentrations in splenic T cells and macrophages. Pearson correlation between RPV-NC percent positive population and RPV drug levels in splenic **(H)** T cells; r = 0.72 and **(I)** macrophages; r = 0.97.

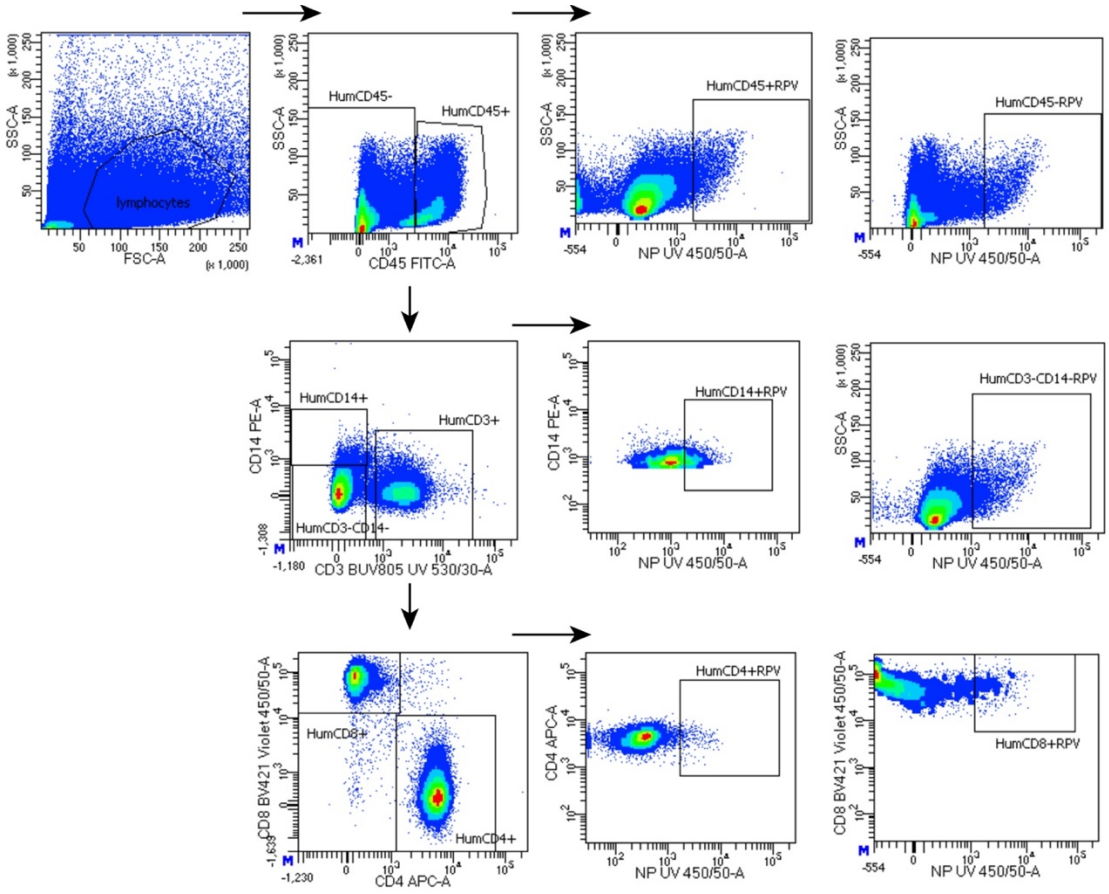

Figure 4.4 Gating strategy for *in vivo* tracking of RPV-NC in humanized mice.

CD45 (pan-leukocyte) marker was used differentiate human- from murine cells. $CD45^+$ populations were then sub-gated into CD14+ (monocyte-macrophage) and $CD3^+$ (T lymphocyte) populations. $CD3^+$ populations were then sub-gated into CD4+ and $CD8^+$ populations. Gates for RPV-NC positive populations were drawn based on plots from untreated control mice.

CHAPTER 5. DISCUSSION

Treatment for HIV/AIDS has made significant progress since its first descriptions in the early 1980s[5, 11-13, 17, 156]. ART readily suppresses viral replication to undetectable levels and improves the quality and longevity of life[157-159]. The recent emergence of LA ART extends the prior ART successes and has led to improvements in treatment regimens and patient adherence as well as prevent new viral infections[156]. While viral suppression and restoration of immunity have been observed, elimination of the viral reservoir has not yet been achieved. Nonetheless, a number of research strategies are being developed towards HIV cure. This includes improved ART, viral reversal agents and boosting of adaptive immunity. These have been deployed to modulate viral replication then eliminate the residual infected cells. Recent progress has been achieved in this field with LASER ART being able to extend plasma drug levels up to months upon a single injection[7, 8, 138]. Further advances have also been able to eliminate HIV in animal models using a combination of LASER ART and CRISPR-Cas 9 excision systems[14]. One of the major hurdles involving efforts to cure HIV lies in the latent viral reservoirs that develop in tissues and cells[16, 18, 19, 31]. It has been well-known that the major cellular reservoirs of latent HIV infection are the CD4+ T cells[104-106]. Since the major leukocyte harboring latent HIV infection is the CD4+ T cell [104-106] and to a lesser degree the monocyte-macrophage, tracking of viral cell reservoirs is imperative to seek out sites of low-level HIV replication so that viral elimination can be achieved. While such cell tracking could be achieved through gold,

magnetic and programmed nanoparticles [76, 87, 90] concerns for both sensitivity and specificity of such systems abound. AIE could overcome such limitations as it allows for visualization of ARVs or excision-containing nanoparticles endocytosed by these cellular reservoirs as well as simultaneously permitting quantitative drug assessment.

To effectively achieve viral elimination, therapeutically effective amounts of viral suppressive and elimination agents must reach cellular reservoirs of HIV. Thus, ARV tracking to sites of viral infection is required. The development of RPV-NC exhibiting AIE could enable this need to be achieved. Correlations made between amount of therapeutic nanoparticle payloads delivered to cells harboring latent HIV and elimination of infection could be realized. Thus, the technologies developed herein would provide a pathway forward towards such required therapeutic delivery. Indeed, molecules with AIE properties have already shown to possess a wide range of applications. These include chemical sensors to biological imaging probes and have been used successfully in a range of applications in diagnosis and therapy [65, 80, 81, 160, 161]. One such prototypical molecule is tetraphenylethylene (TPE) [68, 70, 71, 81]. The AIE characteristics of TPE were deployed as an AIE fluorescent probe for real time tracking of cell apoptosis [162]. Other molecules have been derivatized by introducing an AIE-genic fragment to induce strong fluorescence upon aggregation [73, 74]. Clearly, the future use of AIE-active drugs will certainly provide significant added advantages to any presently existing nanoparticle tracking designs.

In this work, we report a novel aggregation-induced emission property of RPV. RPV, an NNRTI that is being used for HIV therapy, exhibits fluorescence emission at 350nm when aggregated. Hence, we hypothesized that the AIE property of RPV can be used as an effective tool to assess nanoparticle integrity and achieve nanoparticle tracking in cellular sub-populations while also achieving therapeutic outcomes. To achieve this goal, we formulated RPV nanocrystals, characterized their AIE phenomenon and utilized them to track nanoparticle presence in HIV targeted cell populations. First, we synthesized RPV-NC through a bottom-up top-down approach by antisolvent precipitation and subsequent size-reduction to obtain nanoparticles that can reach viral target CD4+ T cells and monocyte-macrophages. Second, we thoroughly characterized the morphological and fluorescent properties of RPV-NC in a wide variety of conditions. These characterizations confirmed the AIE property of RPV as well as the crystallinity of formulated RPV-NC. Third, we performed single crystal x-ray crystallography studies and found that RIR was the primary mechanism of AIE expression in RPV-NC. Fourth, we characterized the uptake of RPV-NC in CD14+ macrophages and CD4+ T cells with a broad range of techniques and also ensured cell uptake of RPV-NC in simulated conditions that could reflect what is operative in an HIV infected human host. Fifth, we carried out confocal microscopy analyses of macrophages and T cells treated with RPV-NC and confirmed their presence in cellular and sub-cellular compartments where viral replication is known to ensue. Sixth, PK and biodistribution studies were performed and showed the presence of RPV in liver, spleen and lymph nodes which are major tissue viral reservoirs.

Seventh, confocal analyses of these tissue sections showed the presence of intact RPV-NC in splenic macrophages and human CD4+ T cells of the spleen and lymph node. Eighth, nanoparticle tracking was achieved by flow cytometry in human immune cells using a humanized mouse model. CD4+ T cells and monocyte-macrophages from these animals were isolated by FACS and subjected to drug quantification. These results, taken together, demonstrate the use of AIE to achieve therapeutic nanoparticle tracking in human cellular immune subsets.

All together, we characterized an AIE drug molecule, RPV, and harnessed its fluorescent property for drug biodistribution assessments. Cellular uptake studies were translated into animal models to observe nanoparticle tracking in CD4+ T cells and monocyte-macrophages. When used in combination with other ARVs [156, 163], RPV has the potential to track the biodistribution and cellular uptake of other drugs. In tandem with drug quantification, the AIE phenomena can be used as a platform to optimize drug delivery to cellular viral reservoirs that currently remain elusive. While parallel studies have achieved cellular tracking for other diseases by gold, magnetic and programmed nanoparticles [76, 87, 90], the inherent AIE property of RPV enables simultaneous assessment by fluorescence and drug quantification, affirming the presence of intact ARV nanoparticles in target cellular reservoirs. Our findings may be readily translated into other nanoformulations and can be used with other AIE molecules to achieve nanoparticle tracking to deliver ARV to viral reservoir sites and aid in achieving HIV eradication through continuous improvement of antiretroviral therapies.

BIBLIOGRAPHY

1. UNAIDS. Global HIV & AIDS Statistics- 2020 Fact Sheet. . **2020**.

2. Organization, W.H. HIV/AIDS Fact Sheet. **2020**.

3. May, M. T.; Gompels, M.; Delpech, V.; Porter, K.; Orkin, C.; Kegg, S.; Hay, P.; Johnson, M.; Palfreeman, A.; Gilson, R.; Chadwick, D.; Martin, F.; Hill, T.; Walsh, J.; Post, F.; Fisher, M.; Ainsworth, J.; Jose, S.; Leen, C.; Nelson, M.; Anderson, J.; Sabin, C.; Study, U. K. C. H. C., Impact on life expectancy of HIV-1 positive individuals of CD4+ cell count and viral load response to antiretroviral therapy. *AIDS* **2014,** *28* (8), 1193-202.

4. Antiretroviral Therapy Cohort, C., Survival of HIV-positive patients starting antiretroviral therapy between 1996 and 2013: a collaborative analysis of cohort studies. *Lancet HIV* **2017,** *4* (8), e349-e356.

5. Pau, A. K.; George, J. M., Antiretroviral therapy: current drugs. *Infect Dis Clin North Am* **2014,** *28* (3), 371-402.

6. Vittinghoff, E.; Scheer, S.; O'Malley, P.; Colfax, G.; Holmberg, S. D.; Buchbinder, S. P., Combination antiretroviral therapy and recent declines in AIDS incidence and mortality. *J Infect Dis* **1999,** *179* (3), 717-20.

7. Zhou, T.; Su, H.; Dash, P.; Lin, Z.; Dyavar Shetty, B. L.; Kocher, T.; Szlachetka, A.; Lamberty, B.; Fox, H. S.; Poluektova, L.; Gorantla, S.; McMillan, J.; Gautam, N.; Mosley, R. L.; Alnouti, Y.; Edagwa, B.; Gendelman, H. E., Creation of a nanoformulated cabotegravir prodrug with improved antiretroviral profiles. *Biomaterials* **2018,** *151*, 53-65.

8. Sillman, B.; Bade, A. N.; Dash, P. K.; Bhargavan, B.; Kocher, T.; Mathews, S.; Su, H.; Kanmogne, G. D.; Poluektova, L. Y.; Gorantla, S.; McMillan, J.; Gautam, N.; Alnouti, Y.; Edagwa, B.; Gendelman, H. E., Creation of a long-acting nanoformulated dolutegravir. *Nat Commun* **2018,** *9* (1), 443.

9. Lin, Z.; Gautam, N.; Alnouti, Y.; McMillan, J.; Bade, A. N.; Gendelman, H. E.; Edagwa, B., ProTide generated long-acting abacavir nanoformulations. *Chem Commun (Camb)* **2018,** *54* (60), 8371-8374.

10. van 't Klooster, G.; Hoeben, E.; Borghys, H.; Looszova, A.; Bouche, M. P.; van Velsen, F.; Baert, L., Pharmacokinetics and disposition of rilpivirine (TMC278) nanosuspension as a long-acting injectable antiretroviral formulation. *Antimicrob Agents Chemother* **2010,** *54* (5), 2042-50.

11. Spreen, W. R.; Margolis, D. A.; Pottage, J. C., Jr., Long-acting injectable antiretrovirals for HIV treatment and prevention. *Curr Opin HIV AIDS* **2013,** *8* (6), 565-71.

12. Jackson, A.; McGowan, I., Long-acting rilpivirine for HIV prevention. *Curr Opin HIV AIDS* **2015,** *10* (4), 253-7.

13. Baert, L.; van 't Klooster, G.; Dries, W.; Francois, M.; Wouters, A.; Basstanie, E.; Iterbeke, K.; Stappers, F.; Stevens, P.; Schueller, L.; Van Remoortere, P.; Kraus, G.; Wigerinck, P.; Rosier, J., Development of a long-acting injectable formulation with nanoparticles of rilpivirine (TMC278) for HIV treatment. *Eur J Pharm Biopharm* **2009,** *72* (3), 502-8.

14. Dash, P. K.; Kaminski, R.; Bella, R.; Su, H.; Mathews, S.; Ahooyi, T. M.; Chen, C.; Mancuso, P.; Sariyer, R.; Ferrante, P.; Donadoni, M.; Robinson, J.

A.; Sillman, B.; Lin, Z.; Hilaire, J. R.; Banoub, M.; Elango, M.; Gautam, N.; Mosley, R. L.; Poluektova, L. Y.; McMillan, J.; Bade, A. N.; Gorantla, S.; Sariyer, I. K.; Burdo, T. H.; Young, W. B.; Amini, S.; Gordon, J.; Jacobson, J. M.; Edagwa, B.; Khalili, K.; Gendelman, H. E., Sequential LASER ART and CRISPR Treatments Eliminate HIV-1 in a Subset of Infected Humanized Mice. *Nat Commun* **2019,** *10* (1), 2753.

15. Palmer, S.; Josefsson, L.; Coffin, J. M., HIV reservoirs and the possibility of a cure for HIV infection. *J Intern Med* **2011,** *270* (6), 550-60.

16. Chun, T. W.; Fauci, A. S., HIV reservoirs: pathogenesis and obstacles to viral eradication and cure. *AIDS* **2012,** *26* (10), 1261-8.

17. Hocqueloux, L.; Avettand-Fenoel, V.; Jacquot, S.; Prazuck, T.; Legac, E.; Melard, A.; Niang, M.; Mille, C.; Le Moal, G.; Viard, J. P.; Rouzioux, C.; Virales, A. C. o. t. A. N. d. R. s. l. S. e. l. H., Long-term antiretroviral therapy initiated during primary HIV-1 infection is key to achieving both low HIV reservoirs and normal T cell counts. *J Antimicrob Chemother* **2013,** *68* (5), 1169-78.

18. Churchill, M. J.; Deeks, S. G.; Margolis, D. M.; Siliciano, R. F.; Swanstrom, R., HIV reservoirs: what, where and how to target them. *Nat Rev Microbiol* **2016,** *14* (1), 55-60.

19. Dahl, V.; Josefsson, L.; Palmer, S., HIV reservoirs, latency, and reactivation: prospects for eradication. *Antiviral Res* **2010,** *85* (1), 286-94.

20. Dalgleish, A. G.; Beverley, P. C.; Clapham, P. R.; Crawford, D. H.; Greaves, M. F.; Weiss, R. A., The CD4 (T4) antigen is an essential component of the receptor for the AIDS retrovirus. *Nature* **1984,** *312* (5996), 763-7.

21. Dragic, T.; Litwin, V.; Allaway, G. P.; Martin, S. R.; Huang, Y.; Nagashima, K. A.; Cayanan, C.; Maddon, P. J.; Koup, R. A.; Moore, J. P.; Paxton, W. A., HIV-1 entry into CD4+ cells is mediated by the chemokine receptor CC-CKR-5. *Nature* **1996,** *381* (6584), 667-73.

22. Melikyan, G. B., Common principles and intermediates of viral protein-mediated fusion: the HIV-1 paradigm. *Retrovirology* **2008,** *5*, 111.

23. Hu, W. S.; Hughes, S. H., HIV-1 reverse transcription. *Cold Spring Harb Perspect Med* **2012,** *2* (10).

24. Kirchhoff, F., HIV life cycle: overview. *Encyclopedia of AIDS* **2013**, 1-9.

25. Craigie, R.; Bushman, F. D., HIV DNA integration. *Cold Spring Harb Perspect Med* **2012,** *2* (7), a006890.

26. Das, A. T.; Harwig, A.; Berkhout, B., The HIV-1 Tat protein has a versatile role in activating viral transcription. *J Virol* **2011,** *85* (18), 9506-16.

27. Sundquist, W. I.; Krausslich, H. G., HIV-1 assembly, budding, and maturation. *Cold Spring Harb Perspect Med* **2012,** *2* (7), a006924.

28. Maartens, G.; Celum, C.; Lewin, S. R., HIV infection: epidemiology, pathogenesis, treatment, and prevention. *Lancet* **2014,** *384* (9939), 258-71.

29. Brenchley, J. M.; Schacker, T. W.; Ruff, L. E.; Price, D. A.; Taylor, J. H.; Beilman, G. J.; Nguyen, P. L.; Khoruts, A.; Larson, M.; Haase, A. T.; Douek, D. C., CD4+ T cell depletion during all stages of HIV disease occurs predominantly in the gastrointestinal tract. *J Exp Med* **2004,** *200* (6), 749-59.

30. Chun, T. W.; Fauci, A. S., Latent reservoirs of HIV: obstacles to the eradication of virus. *Proc Natl Acad Sci U S A* **1999,** *96* (20), 10958-61.

31. Chun, T. W.; Moir, S.; Fauci, A. S., HIV reservoirs as obstacles and opportunities for an HIV cure. *Nat Immunol* **2015,** *16* (6), 584-9.

32. Harrigana, P. R.; Whaley, M.; Montaner, J. S., Rate of HIV-1 RNA rebound upon stopping antiretroviral therapy. *Aids* **1999,** *13* (8), F59-F62.

33. Eisele, E.; Siliciano, R. F., Redefining the viral reservoirs that prevent HIV-1 eradication. *Immunity* **2012,** *37* (3), 377-88.

34. Zack, J. A., The role of the cell cycle in HIV-1 infection. *Adv Exp Med Biol* **1995,** *374*, 27-31.

35. Bukrinsky, M. I.; Stanwick, T. L.; Dempsey, M. P.; Stevenson, M., Quiescent T lymphocytes as an inducible virus reservoir in HIV-1 infection. *Science* **1991,** *254* (5030), 423-7.

36. Blankson, J. N.; Persaud, D.; Siliciano, R. F., The challenge of viral reservoirs in HIV-1 infection. *Annu Rev Med* **2002,** *53*, 557-93.

37. Abrahams, M.-R.; Joseph, S. B.; Garrett, N.; Tyers, L.; Moeser, M.; Archin, N.; Council, O. D.; Matten, D.; Zhou, S.; Doolabh, D.; Anthony, C.; Goonetilleke, N.; Karim, S. A.; Margolis, D. M.; Pond, S. K.; Williamson, C.; Swanstrom, R., The replication-competent HIV-1 latent reservoir is primarily established near the time of therapy initiation. *Science Translational Medicine* **2019,** *11* (513), eaaw5589.

38. Schrager, L. K.; D'Souza, M. P., Cellular and anatomical reservoirs of HIV-1 in patients receiving potent antiretroviral combination therapy. *Jama* **1998,** *280* (1), 67-71.

39. Cavert, W.; Haase, A. T., A national tissue bank to track HIV eradication and immune reconstitution. *Science* **1998,** *280* (5371), 1865-1866.

40. Coleman, C. M.; Wu, L., HIV interactions with monocytes and dendritic cells: viral latency and reservoirs. *Retrovirology* **2009,** *6* (1), 51.

41. Crowe, S.; Zhu, T.; Muller, W. A., The contribution of monocyte infection and trafficking to viral persistence, and maintenance of the viral reservoir in HIV infection. *J Leukoc Biol* **2003,** *74* (5), 635-41.

42. Castor, T. P., Phospholipid nanosomes. *Curr Drug Deliv* **2005,** *2* (4), 329-40.

43. Voinea, M.; Simionescu, M., Designing of 'intelligent' liposomes for efficient delivery of drugs. *J Cell Mol Med* **2002,** *6* (4), 465-74.

44. Bummer, P. M., Physical chemical considerations of lipid-based oral drug delivery--solid lipid nanoparticles. *Crit Rev Ther Drug Carrier Syst* **2004,** *21* (1), 1-20.

45. Manjunath, K.; Reddy, J. S.; Venkateswarlu, V., Solid lipid nanoparticles as drug delivery systems. *Methods Find Exp Clin Pharmacol* **2005,** *27* (2), 127-44.

46. Roney, C.; Kulkarni, P.; Arora, V.; Antich, P.; Bonte, F.; Wu, A.; Mallikarjuana, N. N.; Manohar, S.; Liang, H. F.; Kulkarni, A. R.; Sung, H. W.; Sairam, M.; Aminabhavi, T. M., Targeted nanoparticles for drug delivery through the blood-brain barrier for Alzheimer's disease. *J Control Release* **2005,** *108* (2-3), 193-214.

47. Perelson, A. S.; Essunger, P.; Cao, Y.; Vesanen, M.; Hurley, A.; Saksela, K.; Markowitz, M.; Ho, D. D., Decay characteristics of HIV-1-infected compartments during combination therapy. *Nature* **1997,** *387* (6629), 188-91.

48. Zhang, X., Anti-retroviral drugs: current state and development in the next decade. *Acta Pharm Sin B* **2018,** *8* (2), 131-136.

49. HIV Fact Sheet. **2020**.

50. Craig, J. C.; Duncan, I. B.; Hockley, D.; Grief, C.; Roberts, N. A.; Mills, J. S., Antiviral properties of Ro 31-8959, an inhibitor of human immunodeficiency virus (HIV) proteinase. *Antiviral Res* **1991,** *16* (4), 295-305.

51. Koup, R. A.; Merluzzi, V. J.; Hargrave, K. D.; Adams, J.; Grozinger, K.; Eckner, R. J.; Sullivan, J. L., Inhibition of human immunodeficiency virus type 1 (HIV-1) replication by the dipyridodiazepinone BI-RG-587. *J Infect Dis* **1991,** *163* (5), 966-70.

52. Wild, C. T.; Shugars, D. C.; Greenwell, T. K.; McDanal, C. B.; Matthews, T. J., Peptides corresponding to a predictive alpha-helical domain of human immunodeficiency virus type 1 gp41 are potent inhibitors of virus infection. *Proc Natl Acad Sci U S A* **1994,** *91* (21), 9770-4.

53. Dorr, P.; Westby, M.; Dobbs, S.; Griffin, P.; Irvine, B.; Macartney, M.; Mori, J.; Rickett, G.; Smith-Burchnell, C.; Napier, C.; Webster, R.; Armour, D.; Price, D.; Stammen, B.; Wood, A.; Perros, M., Maraviroc (UK-427,857), a potent, orally bioavailable, and selective small-molecule inhibitor of chemokine receptor CCR5 with broad-spectrum anti-human immunodeficiency virus type 1 activity. *Antimicrob Agents Chemother* **2005,** *49* (11), 4721-32.

54. Summa, V.; Petrocchi, A.; Bonelli, F.; Crescenzi, B.; Donghi, M.; Ferrara, M.; Fiore, F.; Gardelli, C.; Gonzalez Paz, O.; Hazuda, D. J.; Jones, P.; Kinzel, O.; Laufer, R.; Monteagudo, E.; Muraglia, E.; Nizi, E.; Orvieto, F.; Pace, P.; Pescatore, G.; Scarpelli, R.; Stillmock, K.; Witmer, M. V.; Rowley, M., Discovery of raltegravir, a potent, selective orally bioavailable HIV-integrase inhibitor for the treatment of HIV-AIDS infection. *J Med Chem* **2008,** *51* (18), 5843-55.

55. Kozal, M.; Aberg, J.; Pialoux, G.; Cahn, P.; Thompson, M.; Molina, J. M.; Grinsztejn, B.; Diaz, R.; Castagna, A.; Kumar, P.; Latiff, G.; DeJesus, E.; Gummel, M.; Gartland, M.; Pierce, A.; Ackerman, P.; Llamoso, C.; Lataillade, M.; Team, B. T., Fostemsavir in Adults with Multidrug-Resistant HIV-1 Infection. *N Engl J Med* **2020,** *382* (13), 1232-1243.

56. Zhang, L.; Ramratnam, B.; Tenner-Racz, K.; He, Y.; Vesanen, M.; Lewin, S.; Talal, A.; Racz, P.; Perelson, A. S.; Korber, B. T.; Markowitz, M.; Ho, D. D., Quantifying residual HIV-1 replication in patients receiving combination antiretroviral therapy. *N Engl J Med* **1999,** *340* (21), 1605-13.

57. Flexner, C., HIV drug development: the next 25 years. *Nature Reviews Drug Discovery* **2007,** *6* (12), 959-966.

58. Mathias, A. A.; Hinkle, J.; Menning, M.; Hui, J.; Kaul, S.; Kearney, B. P.; Efavirenz/Emtricitabine/Tenofovir Disoproxil Fumarate Single-Tablet Regimen Development, T., Bioequivalence of efavirenz/emtricitabine/tenofovir disoproxil fumarate single-tablet regimen. *J Acquir Immune Defic Syndr* **2007,** *46* (2), 167-73.

59. Wohl, D. A.; Yazdanpanah, Y.; Baumgarten, A.; Clarke, A.; Thompson, M. A.; Brinson, C.; Hagins, D.; Ramgopal, M. N.; Antinori, A.; Wei, X., Bictegravir combined with emtricitabine and tenofovir alafenamide versus dolutegravir, abacavir, and lamivudine for initial treatment of HIV-1 infection: week 96 results from a randomised, double-blind, multicentre, phase 3, non-inferiority trial. *The Lancet HIV* **2019,** *6* (6), e355-e363.

60. Janssen, P. A.; Lewi, P. J.; Arnold, E.; Daeyaert, F.; de Jonge, M.; Heeres, J.; Koymans, L.; Vinkers, M.; Guillemont, J.; Pasquier, E.; Kukla, M.; Ludovici, D.; Andries, K.; de Bethune, M. P.; Pauwels, R.; Das, K.; Clark, A. D., Jr.; Frenkel, Y. V.; Hughes, S. H.; Medaer, B.; De Knaep, F.; Bohets, H.; De Clerck, F.; Lampo, A.; Williams, P.; Stoffels, P., In search of a novel anti-HIV drug: multidisciplinary coordination in the discovery of 4-[[4-[[4-[(1E)-2-cyanoethenyl]-2,6-dimethylphenyl]amino]-2- pyrimidinyl]amino]benzonitrile (R278474, rilpivirine). *J Med Chem* **2005,** *48* (6), 1901-9.

61. Sharma, M.; Saravolatz, L. D., Rilpivirine: a new non-nucleoside reverse transcriptase inhibitor. *J Antimicrob Chemother* **2013,** *68* (2), 250-6.

62. Martinez, E.; Blanco, J. L.; Arnaiz, J. A.; Perez-Cuevas, J. B.; Mocroft, A.; Cruceta, A.; Marcos, M. A.; Milinkovic, A.; Garcia-Viejo, M. A.; Mallolas, J.; Carne, X.; Phillips, A.; Gatell, J. M., Hepatotoxicity in HIV-1-infected patients receiving nevirapine-containing antiretroviral therapy. *AIDS* **2001,** *15* (10), 1261-8.

63. Decloedt, E. H.; Maartens, G., Neuronal toxicity of efavirenz: a systematic review. *Expert Opin Drug Saf* **2013,** *12* (6), 841-6.

64. Mei, J.; Leung, N. L.; Kwok, R. T.; Lam, J. W.; Tang, B. Z., Aggregation-Induced Emission: Together We Shine, United We Soar! *Chem Rev* **2015,** *115* (21), 11718-940.

65. Hong, Y.; Lam, J. W.; Tang, B. Z., Aggregation-induced emission: phenomenon, mechanism and applications. *Chem Commun (Camb)* **2009,** (29), 4332-53.

66. Hong, Y.; Lam, J. W.; Tang, B. Z., Aggregation-induced emission. *Chem Soc Rev* **2011,** *40* (11), 5361-88.

67. Mei, J.; Hong, Y.; Lam, J. W.; Qin, A.; Tang, Y.; Tang, B. Z., Aggregation-induced emission: the whole is more brilliant than the parts. *Adv Mater* **2014,** *26* (31), 5429-79.

68. Liu, J. L.; Zhang, J. Q.; Tang, Z. L.; Zhuo, Y.; Chai, Y. Q.; Yuan, R., Near-infrared aggregation-induced enhanced electrochemiluminescence from tetraphenylethylene nanocrystals: a new generation of ECL emitters. *Chem Sci* **2019,** *10* (16), 4497-4501.

69. Wang, W.; Lin, T.; Wang, M.; Liu, T. X.; Ren, L.; Chen, D.; Huang, S., Aggregation emission properties of oligomers based on tetraphenylethylene. *J Phys Chem B* **2010,** *114* (18), 5983-8.

70. Gao, W.; Lee, D.; Meng, Z.; Li, T., Exploring intracellular fate of drug nanocrystals with crystal-integrated and environment-sensitive fluorophores. *J Control Release* **2017,** *267*, 214-222.

71. Kokado*, T. J. T. T. S. K., Control of Aggregation-Induced Emission from a Tetraphenylethene Derivative through the Components in the Co-crystal. *Crystal Growth & Design* **2018**.

72. Zhang, T.; Jiang, Y.; Niu, Y.; Wang, D.; Peng, Q.; Shuai, Z., Aggregation effects on the optical emission of 1,1,2,3,4,5-hexaphenylsilole (HPS): a QM/MM study. *J Phys Chem A* **2014,** *118* (39), 9094-104.

73. Srivastava, A. K.; Singh, A.; Mishra, L., Tuning of Aggregation Enhanced Emission and Solid State Emission from 1,8-Naphthalimide Derivatives: Nanoaggregates, Spectra, and DFT Calculations. *J Phys Chem A* **2016,** *120* (26), 4490-504.

74. Chen, J.; Xu, B.; Ouyang, X.; Tang, B. Z.; Cao, Y., Aggregation-Induced Emission of cis,cis-1,2,3,4-Tetraphenylbutadiene from Restricted Intramolecular Rotation. *The Journal of Physical Chemistry A* **2004,** *108* (37), 7522-7526.

75. Temme, S.; Baran, P.; Bouvain, P.; Grapentin, C.; Kramer, W.; Knebel, B.; Al-Hasani, H.; Moll, J. M.; Floss, D.; Schrader, J.; Schubert, R.; Flogel, U.; Scheller, J., Synthetic Cargo Internalization Receptor System for Nanoparticle Tracking of Individual Cell Populations by Fluorine Magnetic Resonance Imaging. *ACS Nano* **2018,** *12* (11), 11178-11192.

76. Heo, M. B.; Lim, Y. T., Programmed nanoparticles for combined immunomodulation, antigen presentation and tracking of immunotherapeutic cells. *Biomaterials* **2014,** *35* (1), 590-600.

77. Wang, F.; Wen, S.; He, H.; Wang, B.; Zhou, Z.; Shimoni, O.; Jin, D., Microscopic inspection and tracking of single upconversion nanoparticles in living cells. *Light Sci Appl* **2018,** *7*, 18007.

78. Idris, N. M.; Li, Z.; Ye, L.; Sim, E. K.; Mahendran, R.; Ho, P. C.; Zhang, Y., Tracking transplanted cells in live animal using upconversion fluorescent nanoparticles. *Biomaterials* **2009,** *30* (28), 5104-13.

79. He, Z.; Ke, C.; Tang, B. Z., Journey of Aggregation-Induced Emission Research. *ACS Omega* **2018,** *3* (3), 3267-3277.

80. Zhao, Z.; Lam, J. W. Y.; Tang, B. Z., Tetraphenylethene: a versatile AIE building block for the construction of efficient luminescent materials for organic light-emitting diodes. *Journal of Materials Chemistry* **2012,** *22* (45), 23726-23740.

81. Wang, M.; Zhang, G.; Zhang, D.; Zhu, D.; Tang, B. Z., Fluorescent bio/chemosensors based on silole and tetraphenylethene luminogens with aggregation-induced emission feature. *Journal of Materials Chemistry* **2010,** *20* (10), 1858-1867.

82. Qin, A.; Lam, J. W. Y.; Tang, L.; Jim, C. K. W.; Zhao, H.; Sun, J.; Tang, B. Z., Polytriazoles with Aggregation-Induced Emission Characteristics: Synthesis by Click Polymerization and Application as Explosive Chemosensors. *Macromolecules* **2009,** *42* (5), 1421-1424.

83. Cao, H.; Yue, Z.; Gao, H.; Chen, C.; Cui, K.; Zhang, K.; Cheng, Y.; Shao, G.; Kong, D.; Li, Z.; Ding, D.; Wang, Y., In Vivo Real-Time Imaging of Extracellular Vesicles in Liver Regeneration via Aggregation-Induced Emission Luminogens. *ACS Nano* **2019,** *13* (3), 3522-3533.

84. Yu, C. Y.; Xu, H.; Ji, S.; Kwok, R. T.; Lam, J. W.; Li, X.; Krishnan, S.; Ding, D.; Tang, B. Z., Mitochondrion-Anchoring Photosensitizer with Aggregation-Induced Emission Characteristics Synergistically Boosts the Radiosensitivity of Cancer Cells to Ionizing Radiation. *Adv Mater* **2017,** *29* (15).

85. Yu, T.; Zhuang, W.; Su, X.; Ma, B.; Hu, J.; He, H.; Li, G.; Wang, Y., Dual-Responsive Micelles with Aggregation-Induced Emission Feature and Two-Photon Aborsption for Accurate Drug Delivery and Bioimaging. *Bioconjug Chem* **2019**.

86. Shi, H.; Liu, J.; Geng, J.; Tang, B. Z.; Liu, B., Specific Detection of Integrin αvβ3 by Light-Up Bioprobe with Aggregation-Induced Emission Characteristics. *Journal of the American Chemical Society* **2012,** *134* (23), 9569-9572.

87. Shi, H.; Kwok, R. T. K.; Liu, J.; Xing, B.; Tang, B. Z.; Liu, B., Real-Time Monitoring of Cell Apoptosis and Drug Screening Using Fluorescent Light-Up Probe with Aggregation-Induced Emission Characteristics. *Journal of the American Chemical Society* **2012,** *134* (43), 17972-17981.

88. Feng, G.; Liu, B., Aggregation-Induced Emission (AIE) Dots: Emerging Theranostic Nanolights. *Accounts of Chemical Research* **2018,** *51* (6), 1404-1414.

89. Li, K.; Qin, W.; Ding, D.; Tomczak, N.; Geng, J.; Liu, R.; Liu, J.; Zhang, X.; Liu, H.; Liu, B.; Tang, B. Z., Photostable fluorescent organic dots with aggregation-induced emission (AIE dots) for noninvasive long-term cell tracing. *Sci Rep* **2013,** *3*, 1150.

90. Lewin, M.; Carlesso, N.; Tung, C. H.; Tang, X. W.; Cory, D.; Scadden, D. T.; Weissleder, R., Tat peptide-derivatized magnetic nanoparticles allow in vivo tracking and recovery of progenitor cells. *Nat Biotechnol* **2000,** *18* (4), 410-4.

91. Meir, R.; Shamalov, K.; Betzer, O.; Motiei, M.; Horovitz-Fried, M.; Yehuda, R.; Popovtzer, A.; Popovtzer, R.; Cohen, C. J., Nanomedicine for Cancer Immunotherapy: Tracking Cancer-Specific T-Cells in Vivo with Gold Nanoparticles and CT Imaging. *ACS Nano* **2015,** *9* (6), 6363-72.

92. Romano, J.; Kashuba, A.; Becker, S.; Cummins, J.; Turpin, J.; Veronese, F.; Antiretroviral Pharmacology In, H. I. V. P. T. T. P., Pharmacokinetics and pharmacodynamics in HIV prevention; current status and future directions: a summary of the DAIDS and BMGF sponsored think tank on pharmacokinetics (PK)/pharmacodynamics (PD) in HIV prevention. *AIDS Res Hum Retroviruses* **2013,** *29* (11), 1418-27.

93. Duwal, S.; Schutte, C.; von Kleist, M., Pharmacokinetics and pharmacodynamics of the reverse transcriptase inhibitor tenofovir and prophylactic efficacy against HIV-1 infection. *PLoS One* **2012,** *7* (7), e40382.

94. Gerber, J. G., Using pharmacokinetics to optimize antiretroviral drug-drug interactions in the treatment of human immunodeficiency virus infection. *Clin Infect Dis* **2000,** *30 Suppl 2*, S123-9.

95. Govil, S.; Katz, D. F., Deducing Mucosal Pharmacokinetics and Pharmacodynamics of the Anti-HIV Molecule Tenofovir from Measurements in Blood. *Scientific Reports* **2019,** *9* (1), 82.

96. Kevadiya, B. D.; Ottemann, B.; Mukadam, I. Z.; Castellanos, L.; Sikora, K.; Hilaire, J. R.; Machhi, J.; Herskovitz, J.; Soni, D.; Hasan, M.; Zhang, W.; Anandakumar, S.; Garrison, J.; McMillan, J.; Edagwa, B.; Mosley, R. L.; Vachet, R. W.; Gendelman, H. E., Rod-shape theranostic nanoparticles facilitate

antiretroviral drug biodistribution and activity in human immunodeficiency virus susceptible cells and tissues. *Theranostics* **2020,** *10* (2), 630-656.

97. Langdon, G.; Davis, J. D.; McFadyen, L. M.; Dewhurst, M.; Brunton, N. S.; Rawal, J. K.; Van der Graaf, P. H.; Benson, N., Translational pharmacokinetic–pharmacodynamic modelling; application to cardiovascular safety data for PF-00821385, a novel HIV agent. *British journal of clinical pharmacology* **2010,** *69* (4), 336-345.

98. Csajka, C.; Verotta, D., Pharmacokinetic–pharmacodynamic modelling: history and perspectives. *Journal of pharmacokinetics and pharmacodynamics* **2006,** *33* (3), 227-279.

99. Felmlee, M. A.; Morris, M. E.; Mager, D. E., Mechanism-based pharmacodynamic modeling. In *Computational Toxicology*, Springer: 2012; pp 583-600.

100. Lavé, T.; Parrott, N.; Grimm, H.; Fleury, A.; Reddy, M., Challenges and opportunities with modelling and simulation in drug discovery and drug development. *Xenobiotica* **2007,** *37* (10-11), 1295-1310.

101. de Velde, F.; Mouton, J. W.; de Winter, B. C.; van Gelder, T.; Koch, B. C., Clinical applications of population pharmacokinetic models of antibiotics: challenges and perspectives. *Pharmacological research* **2018,** *134*, 280-288.

102. Lusic, M.; Siliciano, R. F., Nuclear landscape of HIV-1 infection and integration. *Nature Reviews Microbiology* **2017,** *15* (2), 69-82.

103. Henderson, L. J.; Reoma, L. B.; Kovacs, J. A.; Nath, A., Advances toward Curing HIV-1 Infection in Tissue Reservoirs. *Journal of Virology* **2020,** *94* (3), e00375-19.

104. Siliciano, J. D.; Kajdas, J.; Finzi, D.; Quinn, T. C.; Chadwick, K.; Margolick, J. B.; Kovacs, C.; Gange, S. J.; Siliciano, R. F., Long-term follow-up studies confirm the stability of the latent reservoir for HIV-1 in resting CD4+ T cells. *Nat Med* **2003,** *9* (6), 727-8.

105. Schnittman, S. M.; Psallidopoulos, M. C.; Lane, H. C.; Thompson, L.; Baseler, M.; Massari, F.; Fox, C. H.; Salzman, N. P.; Fauci, A. S., The reservoir for HIV-1 in human peripheral blood is a T cell that maintains expression of CD4. *Science* **1989,** *245* (4915), 305-8.

106. Agosto, L. M.; Herring, M. B.; Mothes, W.; Henderson, A. J., HIV-1-Infected CD4+ T Cells Facilitate Latent Infection of Resting CD4+ T Cells through Cell-Cell Contact. *Cell Rep* **2018,** *24* (8), 2088-2100.

107. Reverchon, E., Supercritical antisolvent precipitation of micro- and nano-particles. *The Journal of Supercritical Fluids* **1999,** *15* (1), 1-21.

108. Thorat, A. A.; Dalvi, S. V., Liquid antisolvent precipitation and stabilization of nanoparticles of poorly water soluble drugs in aqueous suspensions: Recent developments and future perspective. *Chemical Engineering Journal* **2012,** *181-182*, 1-34.

109. Zhou, Y.; Fang, Q.; Niu, B.; Wu, B.; Zhao, Y.; Quan, G.; Pan, X.; Wu, C., Comparative studies on amphotericin B nanosuspensions prepared by a high

pressure homogenization method and an antisolvent precipitation method. *Colloids Surf B Biointerfaces* **2018,** *172*, 372-379.

110. Raghava Srivalli, K. M.; Mishra, B., Drug nanocrystals: A way toward scale-up. *Saudi Pharm J* **2016,** *24* (4), 386-404.

111. Hilaire, J. R.; Bade, A. N.; Sillman, B.; Gautam, N.; Herskovitz, J.; Dyavar Shetty, B. L.; Wojtkiewicz, M. S.; Szlachetka, A.; Lamberty, B. G.; Sravanam, S.; Fox, H. S.; Alnouti, Y.; Dash, P. K.; McMillan, J. M.; Edagwa, B. J.; Gendelman, H. E., Creation of a long-acting rilpivirine prodrug nanoformulation. *J Control Release* **2019,** *311-312*, 201-211.

112. Dong, H.; Luo, M.; Wang, S.; Ma, X., Synthesis and properties of tetraphenylethylene derivatived diarylethene with photochromism and aggregation-induced emission. *Dyes and Pigments* **2017,** *139*, 118-128.

113. Dou, H.; Morehead, J.; Destache, C. J.; Kingsley, J. D.; Shlyakhtenko, L.; Zhou, Y.; Chaubal, M.; Werling, J.; Kipp, J.; Rabinow, B. E.; Gendelman, H. E., Laboratory investigations for the morphologic, pharmacokinetic, and anti-retroviral properties of indinavir nanoparticles in human monocyte-derived macrophages. *Virology* **2007,** *358* (1), 148-58.

114. Brouwer, A. M., Standards for photoluminescence quantum yield measurements in solution. *Pure Appl. Chem.* **2011,** *Vol. 83* (No. 12), 15.

115. Kevadiya, B. D.; Woldstad, C.; Ottemann, B. M.; Dash, P.; Sajja, B. R.; Lamberty, B.; Morsey, B.; Kocher, T.; Dutta, R.; Bade, A. N.; Liu, Y.; Callen, S. E.; Fox, H. S.; Byrareddy, S. N.; McMillan, J. M.; Bronich, T. K.; Edagwa, B. J.; Boska, M. D.; Gendelman, H. E., Multimodal Theranostic Nanoformulations Permit

Magnetic Resonance Bioimaging of Antiretroviral Drug Particle Tissue-Cell Biodistribution. *Theranostics* **2018,** *8* (1), 256-276.

116. Ottemann, B. M.; Helmink, A. J.; Zhang, W.; Mukadam, I.; Woldstad, C.; Hilaire, J. R.; Liu, Y.; McMillan, J. M.; Edagwa, B. J.; Mosley, R. L.; Garrison, J. C.; Kevadiya, B. D.; Gendelman, H. E., Bioimaging predictors of rilpivirine biodistribution and antiretroviral activities. *Biomaterials* **2018,** *185*, 174-193.

117. Dolomanov, O. V.; Bourhis, L. J.; Gildea, R. J.; Howard, J. A. K.; Puschmann, H., OLEX2: a complete structure solution, refinement and analysis program. *Journal of Applied Crystallography* **2009,** *42* (2), 339-341.

118. Sheldrick, G. M., A short history of SHELX. *Acta Crystallogr A* **2008,** *64* (Pt 1), 112-22.

119. Sheldrick, G. M., Crystal structure refinement with SHELXL. *Acta Crystallogr C Struct Chem* **2015,** *71* (Pt 1), 3-8.

120. Chang, X.; Bao, J.; Shan, G.; Bao, Y.; Pan, P., Crystallization-Driven Formation of Diversified Assemblies for Supramolecular Poly(lactic acid)s in Solution. *Crystal Growth & Design* **2017,** *17* (5), 2498-2506.

121. Dobretsov, G.; Syrejschikova, T.; Smolina, N., On mechanisms of fluorescence quenching by water. *Biophysics* **2014,** *59*, 183-188.

122. Aquaro, S.; Calio, R.; Balzarini, J.; Bellocchi, M. C.; Garaci, E.; Perno, C. F., Macrophages and HIV infection: therapeutical approaches toward this strategic virus reservoir. *Antiviral Res* **2002,** *55* (2), 209-25.

123. Honeycutt, J. B.; Wahl, A.; Baker, C.; Spagnuolo, R. A.; Foster, J.; Zakharova, O.; Wietgrefe, S.; Caro-Vegas, C.; Madden, V.; Sharpe, G.; Haase,

A. T.; Eron, J. J.; Garcia, J. V., Macrophages sustain HIV replication in vivo independently of T cells. *J Clin Invest* **2016,** *126* (4), 1353-66.

124. Herskovitz, J.; Gendelman, H. E., HIV and the Macrophage: From Cell Reservoirs to Drug Delivery to Viral Eradication. *J Neuroimmune Pharmacol* **2019,** *14* (1), 52-67.

125. Meltzer, M. S.; Skillman, D. R.; Gomatos, P. J.; Kalter, D. C.; Gendelman, H. E., Role of mononuclear phagocytes in the pathogenesis of human immunodeficiency virus infection. *Annu Rev Immunol* **1990,** *8*, 169-94.

126. Meltzer, M. S.; Skillman, D. R.; Hoover, D. L.; Hanson, B. D.; Turpin, J. A.; Kalter, D. C.; Gendelman, H. E., Macrophages and the human immunodeficiency virus. *Immunol Today* **1990,** *11* (6), 217-23.

127. Beduneau, A.; Ma, Z.; Grotepas, C. B.; Kabanov, A.; Rabinow, B. E.; Gong, N.; Mosley, R. L.; Dou, H.; Boska, M. D.; Gendelman, H. E., Facilitated monocyte-macrophage uptake and tissue distribution of superparmagnetic iron-oxide nanoparticles. *PLoS One* **2009,** *4* (2), e4343.

128. Martinez-Skinner, A. L.; Veerubhotla, R. S.; Liu, H.; Xiong, H.; Yu, F.; McMillan, J. M.; Gendelman, H. E., Functional proteome of macrophage carried nanoformulated antiretroviral therapy demonstrates enhanced particle carrying capacity. *J Proteome Res* **2013,** *12* (5), 2282-94.

129. Cline, M. J.; Swett, V. C., The interaction of human monocytes and lymphocytes. *J Exp Med* **1968,** *128* (6), 1309-25.

130. Kadiu, I.; Gendelman, H. E., Macrophage bridging conduit trafficking of HIV-1 through the endoplasmic reticulum and Golgi network. *J Proteome Res* **2011,** *10* (7), 3225-38.

131. Kadiu, I.; Gendelman, H. E., Human immunodeficiency virus type 1 endocytic trafficking through macrophage bridging conduits facilitates spread of infection. *J Neuroimmune Pharmacol* **2011,** *6* (4), 658-75.

132. David, J. R., Macrophage activation induced by lymphocyte mediators. *Acta Endocrinol Suppl (Copenh)* **1975,** *194*, 245-61.

133. Arainga, M.; Guo, D.; Wiederin, J.; Ciborowski, P.; McMillan, J.; Gendelman, H. E., Opposing regulation of endolysosomal pathways by long-acting nanoformulated antiretroviral therapy and HIV-1 in human macrophages. *Retrovirology* **2015,** *12*, 5.

134. Foley, G. E.; Lazarus, H.; Farber, S.; Uzman, B. G.; Boone, B. A.; McCarthy, R. E., Continuous Culture of Human Lymphoblasts from Peripheral Blood of a Child with Acute Leukemia. *Cancer* **1965,** *18*, 522-9.

135. Nara, P. L.; Fischinger, P. J., Quantitative infectivity assay for HIV-1 and-2. *Nature* **1988,** *332* (6163), 469-70.

136. Mosmann, T., Rapid colorimetric assay for cellular growth and survival: application to proliferation and cytotoxicity assays. *J Immunol Methods* **1983,** *65* (1-2), 55-63.

137. Soni, D.; Bade, A. N.; Gautam, N.; Herskovitz, J.; Ibrahim, I. M.; Smith, N.; Wojtkiewicz, M. S.; Dyavar Shetty, B. L.; Alnouti, Y.; McMillan, J.;

Gendelman, H. E.; Edagwa, B. J., Synthesis of a long acting nanoformulated emtricitabine ProTide. *Biomaterials* **2019,** *222*, 119441.

138. Guo, D.; Zhou, T.; Arainga, M.; Palandri, D.; Gautam, N.; Bronich, T.; Alnouti, Y.; McMillan, J.; Edagwa, B.; Gendelman, H. E., Creation of a Long-Acting Nanoformulated 2',3'-Dideoxy-3'-Thiacytidine. *J Acquir Immune Defic Syndr* **2017,** *74* (3), e75-e83.

139. Kalter, D. C.; Gendelman, H. E.; Meltzer, M. S., Inhibition of human immunodeficiency virus infection in monocytes by monoclonal antibodies against leukocyte adhesion molecules. *Immunol Lett* **1991,** *30* (2), 219-27.

140. Kadiu, I.; Nowacek, A.; McMillan, J.; Gendelman, H. E., Macrophage endocytic trafficking of antiretroviral nanoparticles. *Nanomedicine (Lond)* **2011,** *6* (6), 975-94.

141. Guo, D.; Zhang, G.; Wysocki, T. A.; Wysocki, B. J.; Gelbard, H. A.; Liu, X. M.; McMillan, J. M.; Gendelman, H. E., Endosomal trafficking of nanoformulated antiretroviral therapy facilitates drug particle carriage and HIV clearance. *J Virol* **2014,** *88* (17), 9504-13.

142. Campbell, J. H.; Hearps, A. C.; Martin, G. E.; Williams, K. C.; Crowe, S. M., The importance of monocytes and macrophages in HIV pathogenesis, treatment, and cure. *AIDS* **2014,** *28* (15), 2175-87.

143. Lameijer, M. A.; Tang, J.; Nahrendorf, M.; Beelen, R. H.; Mulder, W. J., Monocytes and macrophages as nanomedicinal targets for improved diagnosis and treatment of disease. *Expert Rev Mol Diagn* **2013,** *13* (6), 567-80.

144. Batrakova, E. V.; Gendelman, H. E.; Kabanov, A. V., Cell-mediated drug delivery. *Expert Opin Drug Deliv* **2011,** *8* (4), 415-33.

145. Orenstein, J. M.; Fox, C.; Wahl, S. M., Macrophages as a source of HIV during opportunistic infections. *Science* **1997,** *276* (5320), 1857-61.

146. MacParland, S. A.; Tsoi, K. M.; Ouyang, B.; Ma, X. Z.; Manuel, J.; Fawaz, A.; Ostrowski, M. A.; Alman, B. A.; Zilman, A.; Chan, W. C.; McGilvray, I. D., Phenotype Determines Nanoparticle Uptake by Human Macrophages from Liver and Blood. *ACS Nano* **2017,** *11* (3), 2428-2443.

147. Weissleder, R.; Nahrendorf, M.; Pittet, M. J., Imaging macrophages with nanoparticles. *Nat Mater* **2014,** *13* (2), 125-38.

148. Nowacek, A.; Kadiu, I.; McMillan, J.; Gendelman, H. E., Methods for isolation and identification of nanoparticle-containing subcellular compartments. *Methods Mol Biol* **2013,** *991*, 47-55.

149. Kadiu, I.; Ricardo-Dukelow, M.; Ciborowski, P.; Gendelman, H. E., Cytoskeletal protein transformation in HIV-1-infected macrophage giant cells. *J Immunol* **2007,** *178* (10), 6404-15.

150. Eugenin, E. A.; Gaskill, P. J.; Berman, J. W., Tunneling nanotubes (TNT) are induced by HIV-infection of macrophages: a potential mechanism for intercellular HIV trafficking. *Cell Immunol* **2009,** *254* (2), 142-8.

151. Dupont, M.; Souriant, S.; Lugo-Villarino, G.; Maridonneau-Parini, I.; Verollet, C., Tunneling Nanotubes: Intimate Communication between Myeloid Cells. *Front Immunol* **2018,** *9*, 43.

152. Compeer, E. B.; Kraus, F.; Ecker, M.; Redpath, G.; Amiezer, M.; Rother, N.; Nicovich, P. R.; Kapoor-Kaushik, N.; Deng, Q.; Samson, G. P. B.; Yang, Z.; Lou, J.; Carnell, M.; Vartoukian, H.; Gaus, K.; Rossy, J., A mobile endocytic network connects clathrin-independent receptor endocytosis to recycling and promotes T cell activation. *Nat Commun* **2018,** *9* (1), 1597.

153. Dash, P. K.; Gendelman, H. E.; Roy, U.; Balkundi, S.; Alnouti, Y.; Mosley, R. L.; Gelbard, H. A.; Mcmillan, J.; Gorantla, S.; Poluektova, L. Y., Long-acting NanoART elicits potent antiretroviral and neuroprotective responses in HIV-1 infected humanized mice. *AIDS (London, England)* **2012,** *26* (17), 2135.

154. Arainga, M.; Edagwa, B.; Mosley, R. L.; Poluektova, L. Y.; Gorantla, S.; Gendelman, H. E., A mature macrophage is a principal HIV-1 cellular reservoir in humanized mice after treatment with long acting antiretroviral therapy. *Retrovirology* **2017,** *14* (1), 17.

155. Gorantla, S.; Sneller, H.; Walters, L.; Sharp, J. G.; Pirruccello, S. J.; West, J. T.; Wood, C.; Dewhurst, S.; Gendelman, H. E.; Poluektova, L., Human immunodeficiency virus type 1 pathobiology studied in humanized BALB/c-Rag2-/-gammac-/- mice. *J Virol* **2007,** *81* (6), 2700-12.

156. Margolis, D. A.; Gonzalez-Garcia, J.; Stellbrink, H. J.; Eron, J. J.; Yazdanpanah, Y.; Podzamczer, D.; Lutz, T.; Angel, J. B.; Richmond, G. J.; Clotet, B.; Gutierrez, F.; Sloan, L.; Clair, M. S.; Murray, M.; Ford, S. L.; Mrus, J.; Patel, P.; Crauwels, H.; Griffith, S. K.; Sutton, K. C.; Dorey, D.; Smith, K. Y.; Williams, P. E.; Spreen, W. R., Long-acting intramuscular cabotegravir and rilpivirine in adults with HIV-1 infection (LATTE-2): 96-week results of a

randomised, open-label, phase 2b, non-inferiority trial. *Lancet* **2017,** *390* (10101), 1499-1510.

157. Rusconi, S.; Marcotullio, S.; Cingolani, A., Long-acting agents for HIV infection: biological aspects, role in treatment and prevention, and patient's perspective. *New Microbiol* **2017,** *40* (2), 75-79.

158. Kirtane, A. R.; Langer, R.; Traverso, G., Past, Present, and Future Drug Delivery Systems for Antiretrovirals. *J Pharm Sci* **2016,** *105* (12), 3471-3482.

159. Ma, A.; Chen, D. M.; Chau, F. M.; Saberi, P., Improving adherence and clinical outcomes through an HIV pharmacist's interventions. *AIDS Care* **2010,** *22* (10), 1189-94.

160. La, D. D.; Bhosale, S. V.; Jones, L. A.; Bhosale, S. V., Tetraphenylethylene-Based AIE-Active Probes for Sensing Applications. *ACS Appl Mater Interfaces* **2018,** *10* (15), 12189-12216.

161. Svechkarev, D.; Mohs, A. M., Organic Fluorescent Dye-based Nanomaterials: Advances in the Rational Design for Imaging and Sensing Applications. *Curr Med Chem* **2019,** *26* (21), 4042-4064.

162. Shi, H.; Kwok, R. T.; Liu, J.; Xing, B.; Tang, B. Z.; Liu, B., Real-time monitoring of cell apoptosis and drug screening using fluorescent light-up probe with aggregation-induced emission characteristics. *J Am Chem Soc* **2012,** *134* (43), 17972-81.

163. Cohen, C.; Wohl, D.; Arribas, J. R.; Henry, K.; Van Lunzen, J.; Bloch, M.; Towner, W.; Wilkins, E.; Ebrahimi, R.; Porter, D.; White, K.; Walker, I.; Chuck, S.; De-Oertel, S.; Fralich, T., Week 48 results from a randomized clinical trial of

rilpivirine/emtricitabine/tenofovir disoproxil fumarate vs. efavirenz/emtricitabine/tenofovir disoproxil fumarate in treatment-naive HIV-1-infected adults. *AIDS* **2014,** *28* (7), 989-97.